Cu_2S ZnCdS THIN FILM HETEROJUNCTION SOLAR CELL STUDIES

by

Shang-wen Chang

Dissertation submitted to the Faculty of the
Virginia Polytechnic Institute and State University
in partial fulfillment of the requirements for the degree of
DOCTOR OF PHILOSOPHY
in
Electrical Engineering

APPROVED:

L. C. Burton, Chairman

C. W. Bostian

T. E. Gilmer

F. C. Lee

D. D. Chen

July, 1985
Blacksburg, Virginia

Cu_2S/ZnCdS THIN FILM HETEROJUNCTION SOLAR CELL STUDIES

by

Shang-wen Chang

(Abstract)

Cu_2S/CdS solar cells have been studied extensively for the past two decades due to their potentially high efficiencies per unit cost. The operation and characteristics of Cu_2S/CdS solar cells are fairly well understood. However, the properties of the newer Cu_2S/ZnCdS cell type are not well understood.

The main goals of this thesis were to compare Cu_2S/CdS and Cu_2S/ZnCdS cells using Cu_2S/CdS cells as a reference, and to understand the operation and properties of Cu_2S/ZnCdS cells in order to improve cell performance. Four different measurements were used in this research to achieve these goals. They were; electrical, spectral, capacitance and deep trap measurements.

I-V measurements give important electrical parameters of the cells; cell efficiency, fill factor, short circuit

current, open circuit voltage, shunt resistance and series resistance are reported. From a $\ln(I_{sc})$ versus V_{oc} measurement, the diode factor, A, was found to be about 1 for Cu_2S/CdS, $Cu_2S/Zn_{0.11}Cd_{0.89}S$, and about 1.2 for $Cu_2S/Zn_{0.25}Cd_{0.75}S$ cells. The relation between $\ln(J_{oo})$ (current density) and ϕ (potential barrier height) is linear for both types of cells. The slope of this linear relationship increases as the content of Zn increases in $Zn_xCd_{1-x}S$. Under air mass 1 (100 mW/cm^2) illumination, it was found that V_{oc} decays and capacitance increases for $Cu_2S/ZnCdS$ cells. This is attributed to electron relaxation from deep traps near the junction.

Spectral response with and without bias light were measured for both Cu_2S/CdS and $Cu_2S/ZnCdS$ cells. White and blue bias light enhance the spectral response, while red bias light quenches the response. This is attributed to ionization and filling of deep traps near the junction.

Capacitance measurements on both cell types show that $1/C^2$ versus voltage is quite flat, which indicates the existence of an i-layer (insulation layer) in the CdS or ZnCdS near the junction.

Three methods-photocapacitance, space-charge-limited current, and thermally stimulated current techniques-were used for deep trap measurements. Photocapacitance

measurements indicate one deep donor energy and two deep acceptor energy levels. These trap energies become larger as the content of Zn in ZnCdS increases. Space-charge-limited current measurements give a trap density of the order of 10^{16} cm^{-3} for both cell types. The shallow energy trap is found to be 0.26 eV below the conduction band edge of CdS. The occurrence of a current-saturated region for Cu_2S/ZnCdS is attributed to the filling of the interface traps near the junction. Thermally stimulated current measurements give two energy levels below the conduction band of CdS; 0.05 eV and 0.26 eV.

From the above results, several differences between the Cu_2S/CdS and the Cu_2S/ZnCdS cells can be seen. The Cu_2S/ZnCdS cells show stronger red quenching, smaller electron lifetime at the interface near the junction, and deeper traps than the Cu_2S/CdS cells. These differences can account for the decline of I_{sc} and the V_{oc} decay. The smaller I_{sc} for the Cu_2S/ZnCdS cells can also possibly result from smaller electron lifetime at the interface, larger interface recombination velocity, different deep trap levels, and enhanced Zn concentration near the junction. The V_{oc} decay for the Cu_2S/ZnCdS cells is mostly due to long decay of charge. Longer decay could be attributed to deeper traps.

Acknowledgements

The auther wishes to express his sincere appreciation to his advisor Dr. L. C. Burton for his guidance, encouragement, and his invaluable assistance during the course of his study. Many thanks also go to the members of his committee, Dr. C. W. Bostian, Dr. T. E. Gilmer, Dr. F. C. Lee, and Dr. D. D. Chen for their review and suggestions of this thesis.

Also, the auther would like to thank his friends and fellow graduate students, , , , and , who provided both friendship and support when he needed them the most.

A special thanks goes to his wife, , for her assistance and encouragement.

Finally, the auther would like to thank the Solar Energy Research Institute, the Chevron Research Company, and Department of Electrical Engineering, Virginia Tech, for the financial support during this period of study.

TABLE OF CONTENTS

LIST OF FIGURES

LISTS OF TABLES

Chapter I

INTRODUCTION

1.1 HISTORICAL BACKGROUND

The Cu_2S/CdS photovoltaic solar cell was first discovered at the Aerospace Research Laboratories in 1954 by Reynolds [1]. A copper layer was electroplated onto an indium-doped CdS crystal, followed by heating for 30 seconds at 350°C. A cell efficiency of 1.5% was obtained. Hammond and Shirland improved the efficiency of this type of cell to over 5% in 1959 [2,3]. All the initial cells were backwall type cells where the incident light passes through the CdS portion first before reaching the junction. The first frontwall cells (where the light is incident upon the Cu_2S first before reaching the junction) were also made by Hammond and Shirland.

The first polycrystalline CdS thin film photovoltaic cells were fabricated at The Clevite Corporation by Carlson *et al*. [4,5]. The CdS was thought to be responsible for the photovoltaic behavior of the junction. In 1960 Williams and Bube studied the photovoltaic effect in Cu-CdS cells and related junctions. Several metals, such as Cu, Fe, Au, Ag and Ni were applied to the CdS by electroplating. It was

found that Cu gave the highest spectral response. Williams and Bube presented a model in terms of photoemission of electrons from the Cu metal into the CdS [6]. Gremmeiss and Memming concluded that photovoltaic cells made of vapor-deposited CdS layers behaved the same as those made of the single crystals. They also proposed that the photovoltaic effect was caused by a p-n junction [7]. Cusano and Keating asserted that Cu_2S formed a heterojunction with the CdS [8,9]. Cusano also showed that the similar results could be obtained from the copper telluride and cadmium telluride heterojunction. They still thought that CdS or CdTe played major part in the absorption of radiation for the result of photovoltaic response. Clevite continued their researches on backwall cells until 1965. In 1965 Clevite started to develop frontwall cells using molybdenum or kapton substrates. The junctions were formed by dipping the CdS films into a CuCl solution. Cell efficiencies between 4 to 6% were obtained at that time. In 1966 Hill and Keramidas, and Selle *et al*. presented a model to describe the formation of the p-type Cu_2S on the n-type CdS layer [10,11]. They found that the photoabsorption occurred mainly in the Cu_2S layer. This model is now widely accepted.

In the 1970's research and development of the Cu_2S/CdS cell were undertaken primarily at the University of

Delaware, Stanford University, Photon Power (United States), S.A.T. (France), Stuttgart University (Germany) and Indian Institute of Technology (India). A lot of efforts were made at modifying earlier processes, material properties and device design. Several theoretical models were proposed to explain the cell behavior. All these developments have led to cell efficiency close to 10% for the Cu_2S/CdS thin film solar cell.

Several techniques can be used to make CdS films, such as vapor deposition, spray deposition, sputtering, sintering and silk screening. Among these, vapor deposition and spray deposition techniques are most commonly used. Cu_2S/CdS junctions can be formed either by dipping process (also called wet process) or dry process. The dipping process is based on an ion exchange reaction between the CdS layer and an aqueous solution of CuCl. The dry process deposits CuCl onto the CdS by the vacuum evaporation technique followed by heat annealing to form the junction. A more detailed explanation of cell fabrication technique will be given in Chapter 2.

Both silicon and CdS solar cells were considered as possible devices for solar energy conversion at the beginning of the space program in the 1950's. Silicon solar cells were used in the space program due to their

reliability and high efficiencies. The Cu_2S/CdS cells have suffered from two problems. First, the cells react with oxygen and water vapor which degrade them very fast. Secondly, the cell conversion efficiency is somewhat low. The highest value so far is 9.15% [12]. In comparison, silicon cells have conversion efficiencies greater than 15%. Cu_2S/CdS cells with efficiencies greater than 10% have been reported by the Indian Institute of Technology [13], but there is some question as to the validity of their measurements.

The reason for interest in the Cu_2S/CdS solar cells is due to their potentially high efficiencies per unit cost and ease of fabrication. The Cu_2S/CdS cells can potentially be produced at low costs in large sheets and are light weight. The fabrication process can be compatible with automated mass production techniques. Large area cells with efficiency of 5% have been fabricated on a pilot plant basis by the vacuum evaporation technique [14].

Since Cu_2S/CdS solar cells are heterojunctions, a 4% lattice mismatch between the Cu_2S and the CdS layers exists. This lattice mismatch creates an interface state density of about 10^{13} to 10^{14} cm^{-2} at the junction. These interface states form recombination centers which lower the output current. Also, due to the two different values of electron

affinity for the Cu_2S and the CdS, an energy step appears between the junction of these two materials which decreases the output voltage. In order to improve cell efficiency, the Cu_2S/ZnCdS solar cell has been developed. The ZnCdS substrate has been used in place of the CdS. Both the lattice mismatch and the electron affinity mismatch can be improved. The output open circuit voltage increases, hence cell efficiency increases. The highest efficiency for the Cu_2S/ZnCdS solar cell is 10.2% [15].

Two problems remain for the Cu_2S/ZnCdS cells. They are: 1) the current density is less than for Cu_2S/CdS cells made under similar conditions. 2) the open circuit voltage decreases with time. The first problem has been studied by Burton [16]. It has been found that Zn diffuses from the ZnCdS layer into the Cu_2S layer. Zn acts as a donor in the Cu_2S and can result in an interfacial spike which causes a decrease in the output current. The second problem has not been studied in detail. Both of these problems, along with other characteristics of the cell, are addressed in this thesis.

1.2 OBJECTIVES OF RESEARCH

The operation and properties of the Cu_2S/CdS type solar cell are fairly well understood; however, the characteristics of the Cu_2S/ZnCdS cells are less well understood. The objectives of this research are to compare the Cu_2S/CdS and the Cu_2S/ZnCdS cells by means of a variety of electrical and optical measurements using Cu_2S/CdS cells as a reference, and to try better to understand the mechanisms of the Cu_2S/ZnCdS cells in order to improve cell performance.

The experimental techniques used in this research can be divided into four sections:

1) Electrical Measurements

Various current-voltage measurements, with temperature as parameter, are measured to study cell characteristics.

2) Spectral Measurements

One-beam and two-beam techniques are used to study the quantum efficiency and optical enhancement and quenching effect on these cells.

3) Capacitance Measurements

Capacitance as a function of an applied voltage is measured to investigate the copper compensated layer at the

interface and to determine the depletion width of the junction.

4) Deep Trap Measurements

Photocapacitance, space-charge-limited current, and thermally stimulated current techniques are applied to deduce the deep trap parameters-mainly, deep trap energy level, concentration and capture cross section in the space charge region.

Chapter II

OPERATION AND CHARACTERISTICS OF THE Cu_2S/CdS AND Cu_2S/ZnCdS HETEROJUNCTION SOLAR CELLS

Cell fabrication techniques, operating principles and important parameters for controlling solar cell performance are examined in this chapter. Other characteristics including electrical properties, spectral response, capacitance behavior and deep trap effects are also presented.

2.1 CELL FABRICATION

Cross sections of the Cu_2S/CdS or the Cu_2S/ZnCdS thin film heterojunction solar cells is shown in Figure 1. These junctions are fabricated using the following steps:

1) Substrate Preparation

Several substrates have been successfully used for the fabrication of these cells including Zn plated copper [17], Zn coated Kapton [18], SnO_2 on glass [19], etc. The most efficient cells have been fabricated on Zn plated copper substrates. A Zn layer of 1 to 2 μm in thickness is

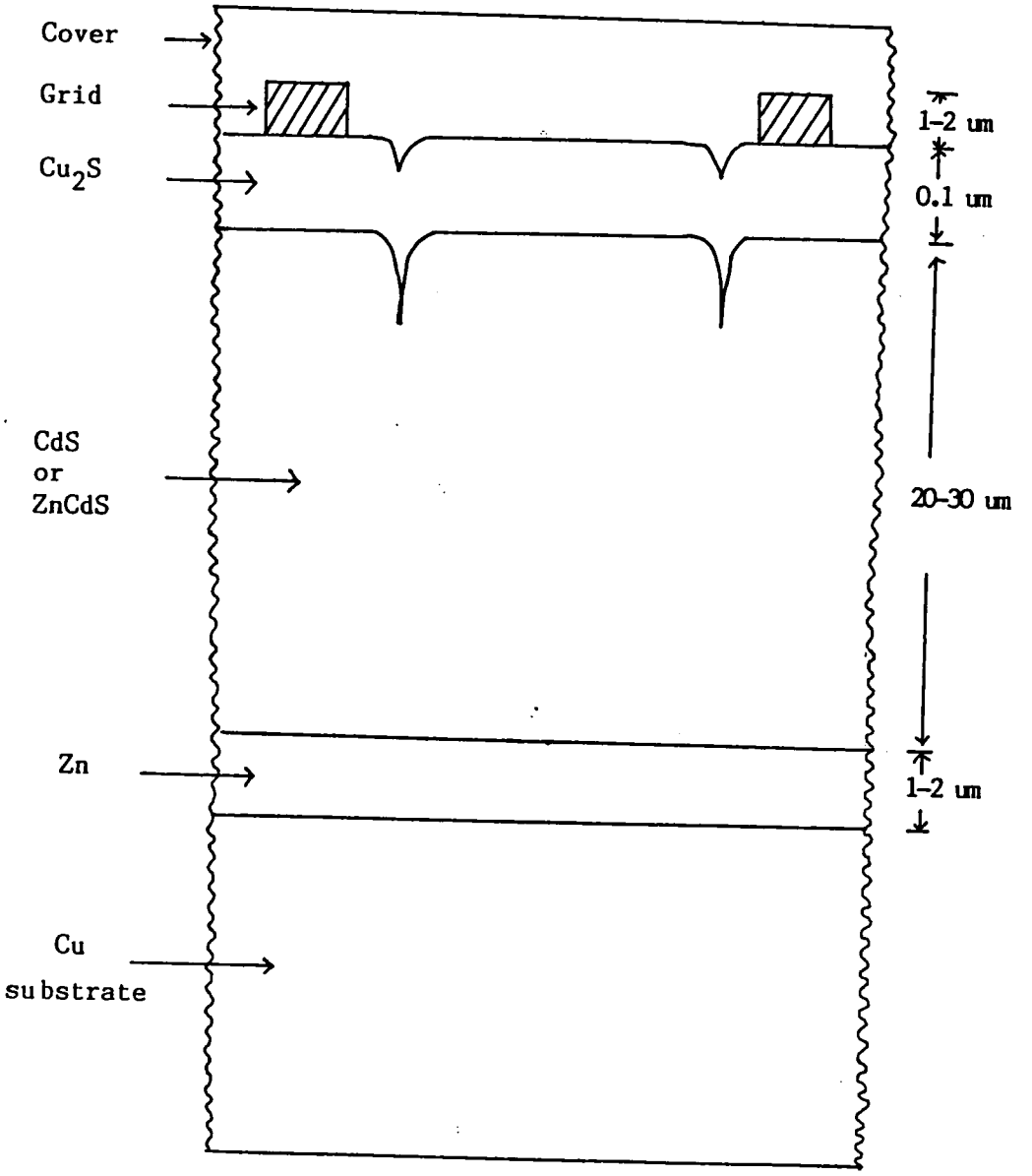

Figure 1: Cross section of a Cu_2S/CdS or Cu_2S/ZnCdS heterojunction solar cell.

electroplated on the copper foil. The Zn layer provides an ohmic contact to both CdS and ZnCdS.

2) CdS and ZnCdS Deposition

For vapor deposition, the CdS film is deposited on the Zn plated copper substrate, which is maintained at about 300°C, by evaporating CdS powder from a graphite source bottle which is maintained at 1000 - 1100°C. The ZnCdS ternary film can be formed using a concentric, dual-chamber source [12]. Source temperatures are maintained at 1100-1150°C for ZnS and 900-1125°C for CdS, depending upon the desired composition. CdS and ZnCdS films can also be formed by the spray deposition technique [20,21,22]. The CdS films are sprayed on a heated substrate with aqueous solutions of cadmium chloride and thiourea; and ZnCdS films are sprayed with solutions of cadmium chloride, zinc chloride and thiourea. The thickness of the CdS or the ZnCdS layer generally is about 20-30 μm. Most of this material is not needed for cell operation, but it is needed to support the Cu_2S and to prevent shorts between the Cu_2S and Zn plated copper substrate through CdS grain boundaries.

3) Junction Formation

There are two important techniques which can be used to form p-n junctions in CdS and ZnCdS. In the dipping process, CdS or ZnCdS films are immersed in a solution of CuCl. This dipping process is based upon an ion exchange reaction between the CdS or the ZnCdS layer and an aqueous solution of a cuprous complex. The equation for the Cu_2S formation is as follows:

$$CdS + 2CuCl \longrightarrow Cu_2S + CdCl_2 \qquad (2\text{-}1)$$

The similar equation for the Cu_2S/ZnCdS junction is as follows:

$$ZnCdS + 2CuCl \longrightarrow Cu_2S + CdCl_2 + ZnCl_2 \qquad (2\text{-}2)$$

In the so-called dry process, CuCl is deposited on the CdS or ZnCdS by the vacuum evaporation technique. The films are then heated in the vacuum chamber until the Cu_2S layers form. A textured surface can increase the effective area of the junction and improve the cell efficiency. Therefore, before the junction is formed, the CdS or ZnCdS should be etched for few seconds in a solution of 50% HCl. The advantage of the dry process is that it is easier to control the formation of the Cu_2S layer. However, cells made from

the dry process show lower efficiencies than those made from the dipping process.

4) Electrical Contact

Gold is a good ohmic contact to the Cu_2S. A gold grid can be evaporated onto the Cu_2S by vacuum deposition through a mask. Another way is to have a gold plated copper grid attached to the Cu_2S by means of epoxy. The space between the individual grid fingers should be small enough to collect all the carriers generated in the Cu_2S without creating significant shading losses (which are typically 5-10%).

5) Post-fabrication Heat Treatment

Before heat treatment, these cells show poor junction behavior with low shunt resistance. Post-fabrication heat treatment is necessary to improve the junction characteristics. These cells are generally heat treated in a reducing ambient of H_2 or in an inert ambient of N_2. During this process, copper diffuses from the Cu_2S layer into the CdS or the ZnCdS layer. The copper acts as an acceptor to compensate the charge carrier in the CdS and form the intrinsic layer between the junction, which reduces the leakage current of the cell and improves the junction behavior.

6) Encapsulation

The last step in cell fabrication is encapsulation; cells should be protected from the atmosphere to prevent degradation. Cu_2S can react with oxygen and water vapor, which reduces cell efficiency very rapidly. Therefore, encapsulation is a very important step during the cell fabrication process. Epoxy or plastic encapsulant can be used for this purpose.

Figure 2 shows the energy band diagram of the Cu_2S/CdS thin film solar cell. The Cu_2S is a p-type material with a bandgap of 1.2 eV, and a very high hole density of about 10^{19} cm^{-3}. The CdS is a n-type semiconductor with a direct bandgap of 2.4 eV. The electron concentration of the CdS is about 10^{17} cm^{-3}. The band bending at the junction, therefore, occurs almost exclusively in the CdS. Since the electron affinity of the CdS is greater than that of the Cu_2S, a step of 0.2 eV exists in the conduction band at the Cu_2S-CdS interface. The diffusion voltage $V_D \approx 0.8$ eV, and $\Delta E \approx 0.1$ eV for $n = 10^{17}$ cm^{-3} (See Figure 2.).

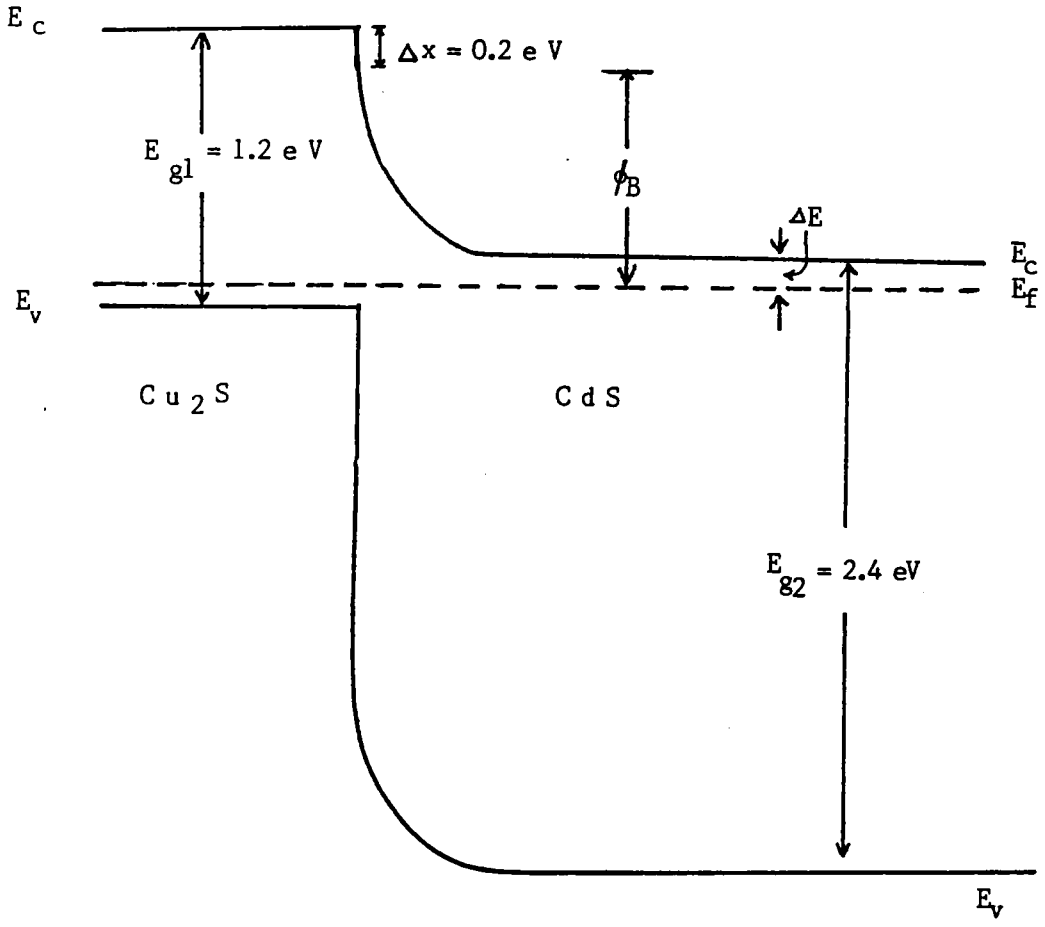

E_c = Conduction band

E_v = Valence band

E_f = Fermi level

Δx = Difference in electron affinities

ϕ_B = Potential barrier height

ΔE = Difference Fermi level and conduction band

Figure 2: Energy band diagram of the Cu_2S/CdS thin film solar cell.

2.2 DARK CURRENT-VOLTAGE CHARACTERISTICS

It is important to understand the dark current mechanisms of the cells, because the current mechanisms operative in the dark are also operative under illumination. In the dark, the electrical equivalent circuit for the Cu_2S/CdS and $Cu_2S/ZnCdS$ cells is shown in Figure 3. The expression for the current-voltage relationship follows:

$$J = J_o(e^{q(V-JR_S)/AkT} - 1) + \frac{V-JR_S}{R_{SH}} \qquad (2\text{-}3)$$

where J_o is the reverse saturation current; q is the electronic charge; A is the diode factor; k is the Boltzmann constant; T is the absolute temperature; R_S and R_{SH} are series resistance and shunt resistance respectively. The values of A and J_o depend on the current mechanism of the diodes. A homojunction is the simplest junction, and it is well understood. Most of the theories and concepts associated with the homojunction can also be applied to the heterojunction. Therefore, before the Cu_2S/CdS or $Cu_2S/ZnCdS$ heterojunctions are discussed, it is best to consider the homojunction first.

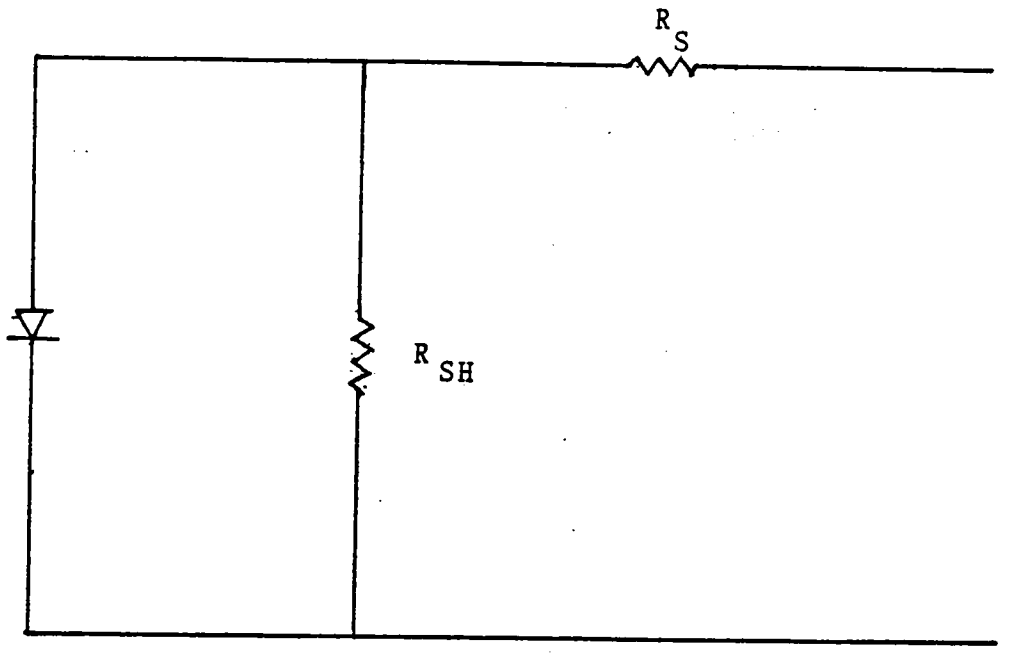

Figure 3: Electrical equivalent circuit for the Cu_2S/CdS and $Cu_2S/ZnCdS$ solar cells.

2.2.1 Homojunction

A p-n junction formed in the same material is called a homojunction. Three different current mechanisms contribute to current-voltage characteristics of the homojunction; these are: 1) injection current, 2) recombination current, and 3) tunneling current.

1) Injection Current

In this case, electrons are injected from the n-side into the p-side of the junction, and holes are injected from the p-side into the n-side. These are indicated by "1" in Figure 4. The theoretical results for J_o and A for injection are:

$$J_{oi} = q\left(\frac{n_{op}L_n}{\tau_n} + \frac{p_{on}L_p}{\tau_p}\right) \qquad (2\text{-}4)$$

$$A = 1$$

where q is the magnitude of the electronic charge; n_{op}, L_n, and τ_n are the equilibrium density of electrons, diffusion length of electrons, and lifetime of electrons in the p-type material; p_{on}, L_p, and τ_p are the corresponding quantities for holes in the n-type material.

2) Recombination Current

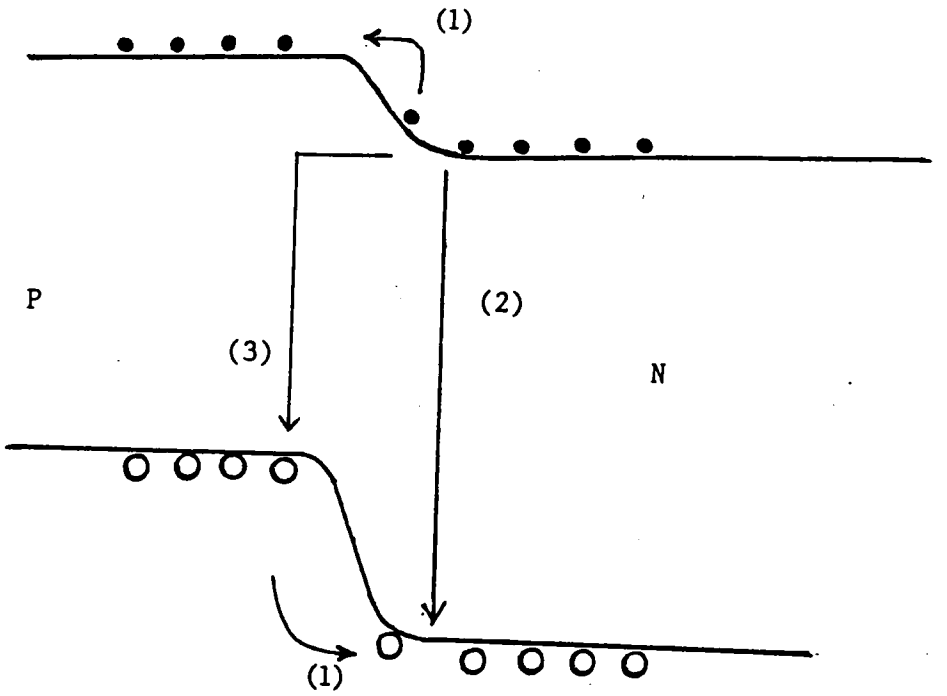

(1) Injection current

(2) Recombination current

(3) Tunneling current

Figure 4: Energy band diagram for the typical p-n junction, with current mechanisms in the dark.

Recombination of electron-hole pairs occurs mainly in the depletion region as indicated by "2" in Figure 4. The forward bias current in this case is

$$J = J_{or}\exp(\frac{qV}{2kT}) \qquad (2\text{-}5)$$

where

$$J_{or} = \frac{qn_i W}{\tau_o}$$

where n_i is the intrinsic carrier concentration; W is the width of the the depletion region, and τ_o is the mean lifetime of minority carriers in the depletion region.

3) Tunneling Current

The tunneling current takes place in homojunction only when the junction is heavily doped. The electrons and holes can tunnel from the conduction or valence band into states within the energy band and do one of two things: they may either tunnel into the opposite band, or they may recombine with the carriers tunneling from the opposite side. Tunneling current refers to the process indicated by "3" in Figure 4. The current-voltage relationship is of the general form

$$J \propto \exp(BV) \qquad (2\text{-}6)$$

where B is a constant.

2.2.2 Heterojunction

Heterojunctions are junctions where p and n regions are formed from two different semiconductors. Heterojunctions have been extensively studied since Schockly proposed in 1951 that they be used in a bipolar transistor [23]. Solar cells are among the most important applications of heterojunctions. Other applications, such as solid state lasers and photodetectors, are also important in heterojunctions, but they will not be discussed here.

Minority carriers forming the injection current are injected into each side of the junction. At the interface between two materials, a large density of interface states exists due to the mismatch of the lattices. Carriers tunnel through the barrier into these states and give rise to conduction via tunneling. These states can also act as recombination centers which contribute to the recombination current. Therefore the current of the heterojunctions usually involves one or more of the current mechanisms. For the case of the Cu_2S/CdS [24] or the Cu_2S/ZnCdS solar cell, the dominating current mechanism in the dark is recombination via interface states at the junction.

2.3 LIGHT-GENERATED CURRENT

The I-V equation for the Cu_2S/CdS and the $Cu_2S/ZnCdS$ junctions in the light can be expressed as

$$J = -J_L + J_o(e^{q(V-JR_S)/AkT} - 1) + \frac{V-JR_S}{R_{SH}} \qquad (2\text{-}7)$$

where J_L is the photocurrent, and where other parameters are as they were defined in Section 2.2. The typical I-V characteristic curve is shown in Figure 5. The open circuit voltage, V_{oc}, can be determined from the V intercept under illumination, and the short circuit current, I_{sc}, can be determined from the I intercept. Series resistance, R_S, and shunt resistance, R_{SH}, can be determined from the slopes in far forward and reverse bias. Fill factor, FF, is defined as $IV)_{MP}/I_{sc}V_{oc}$. Here $IV)_{MP}$ is the IV product at the maximum point. The conversion efficiency of a solar cell, η, is given as $I_{sc}V_{oc}FF/P_{in}$ where P_{in} is the power incident on the cell. The reverse saturation current, J_o, and the diode factor, A, can be obtained from a ln(J) versus V plot.

Incident photons are absorbed almost entirely in the Cu_2S due to its high absorption coefficient. The resulting minority carriers form the light generated current, J_{LO}. However, it is not the light generated current, J_{LO}, but the light collected current, J_L, which is important for the

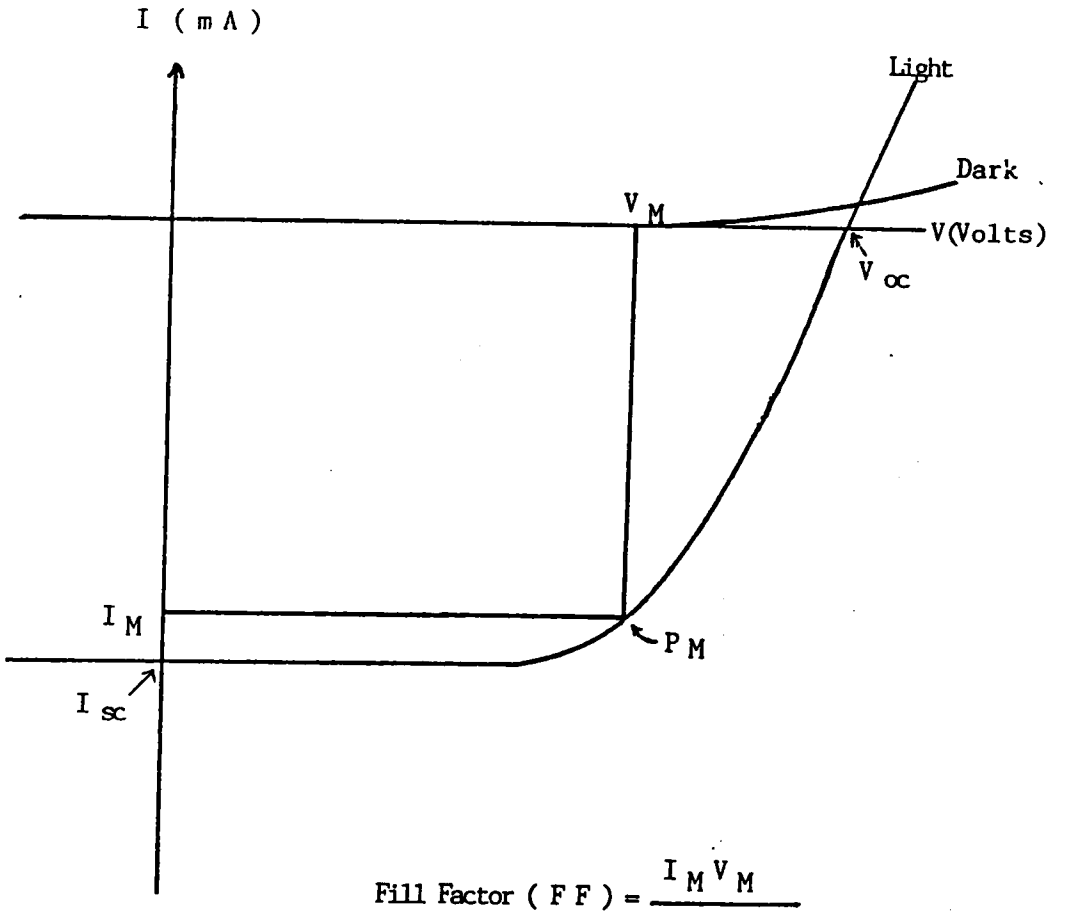

Figure 5: The I-V curve for the Cu_2S/CdS and the $Cu_2S/ZnCdS$ solar cells.

output power of the cell. J_L is related to J_{LO} through the ICF (interface collection factor) relation [25]:

$$J_L = \frac{\mu E_2}{\mu E_2 + S_I} J_{LO} \qquad (2\text{-}8)$$

This can also be written as

$$J_L = \frac{\mu E_2}{\mu E_2 + S_I} \frac{K\alpha L}{(\alpha^2 L^2 - 1)} [S+\alpha D - \exp(-\alpha d)\{(\frac{D}{L})[\sinh(\frac{d}{L}) + \alpha L \cosh(\frac{d}{L})]$$

$$+ S[\alpha L \sinh(\frac{d}{L}) + \cosh(\frac{d}{L})]\}][S\sinh(\frac{d}{L}) + (\frac{D}{L})\cosh(\frac{d}{L})]^{-1} \qquad (2\text{-}9)$$

where μ is the electron mobility in the CdS, E_2 the electric field at the interface in the CdS, S_I the interface recombination velocity, α the absorption coefficient of the Cu_2S, L the diffusion length in the Cu_2S, S the surface recombination velocity at the front face, D the diffusion coefficient, and d the thickness of the Cu_2S. Equation (2-9) is discussed in greater detail later.

The magnitude of the current J_L depends upon several parameters: the stoichiometry of the Cu_xS, the variables α, L, d, S, the electric field in the Cu_2S, as well as the grain size of the Cu_2S. The importance of these parameters is explained as follows

1) Stoichiometry of the Cu_xS

There are several phases which are known to be stable at room temperature, including Cu_2S (chalcocite), $Cu_{1.93}S$ (djurleite), $Cu_{1.8}S$ (digenite), $Cu_{1.75}S$ (anilite), and CuS (covellite). Several studies have shown that the most efficient cells are made with the chalcocite phase (Cu_xS, $2<x<1.996$) [26,27,28]. Palz et al. have shown that the short circuit current of thin film Cu_2S/CdS solar cell is a strong function of the stoichiometry of the Cu_xS layer [29]. As x varies from 2 to 1.96, the current reduces by an order of magnitude. The result from Palz's experiments is presented in Figure 6. The Cu_xS reacts with atmosphere which can change the properties of the cell. It was discovered that a formation or reduction of a few monolayers of copper oxide on the Cu_xS can result in changes of the stoichiometry of the Cu_xS; hence reductions of V_{oc} and I_{sc} of the cell will occur [30].

2) Absorption Coefficient of Cu_2S

It has been found that Cu_2S has a very high absorption coefficient between (10^4 to 10^5 cm^{-1}). The absorption coefficients for several polycrystalline Cu_2S films are shown in Figure 7 [31]. This high absorption coefficient makes it possible to fabricate a thin-film cell with the thickness of few tenths μm of Cu_2S.

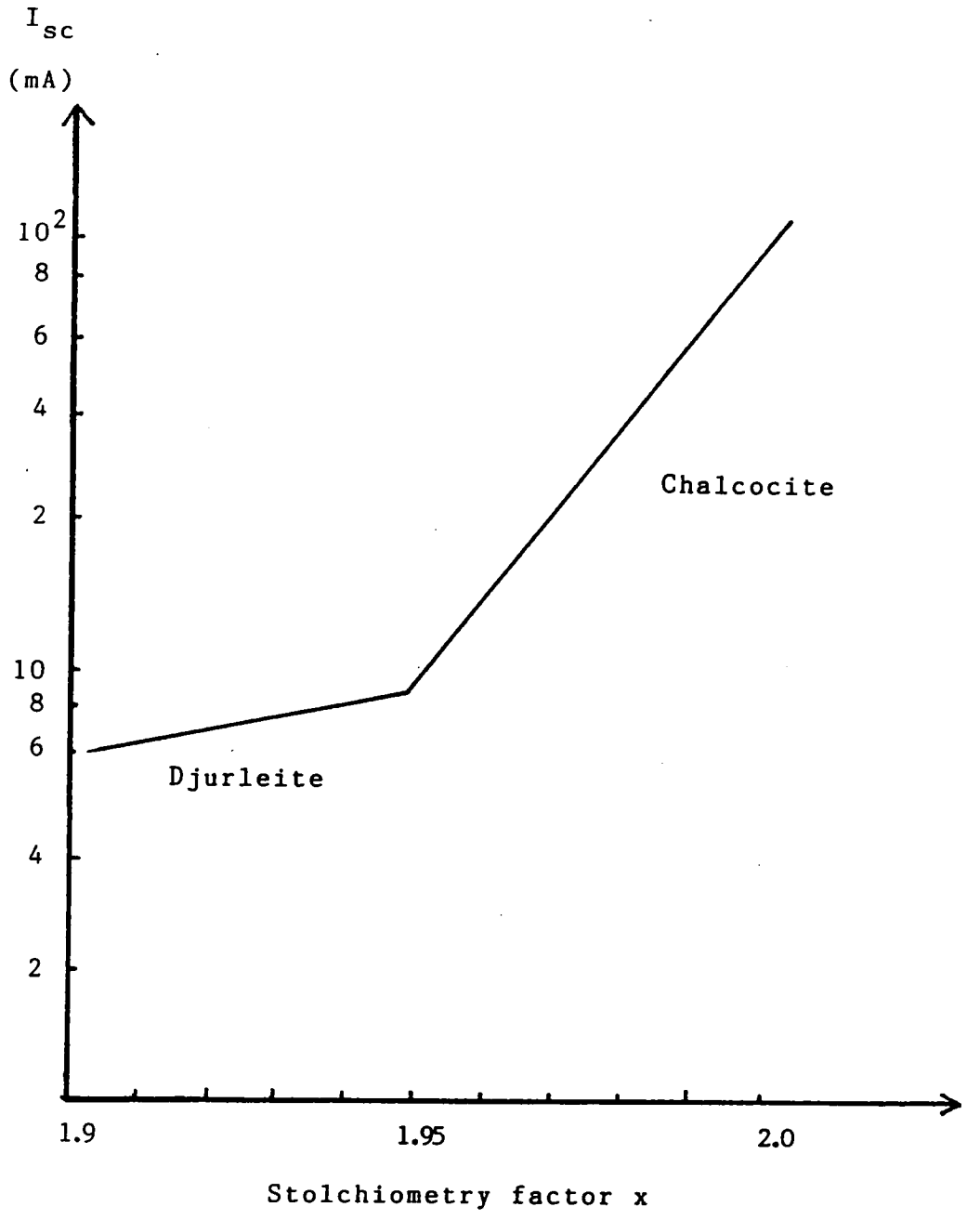

Figure 6: Short circuit current as a function of the stoichiometry of the Cu_xS [29].

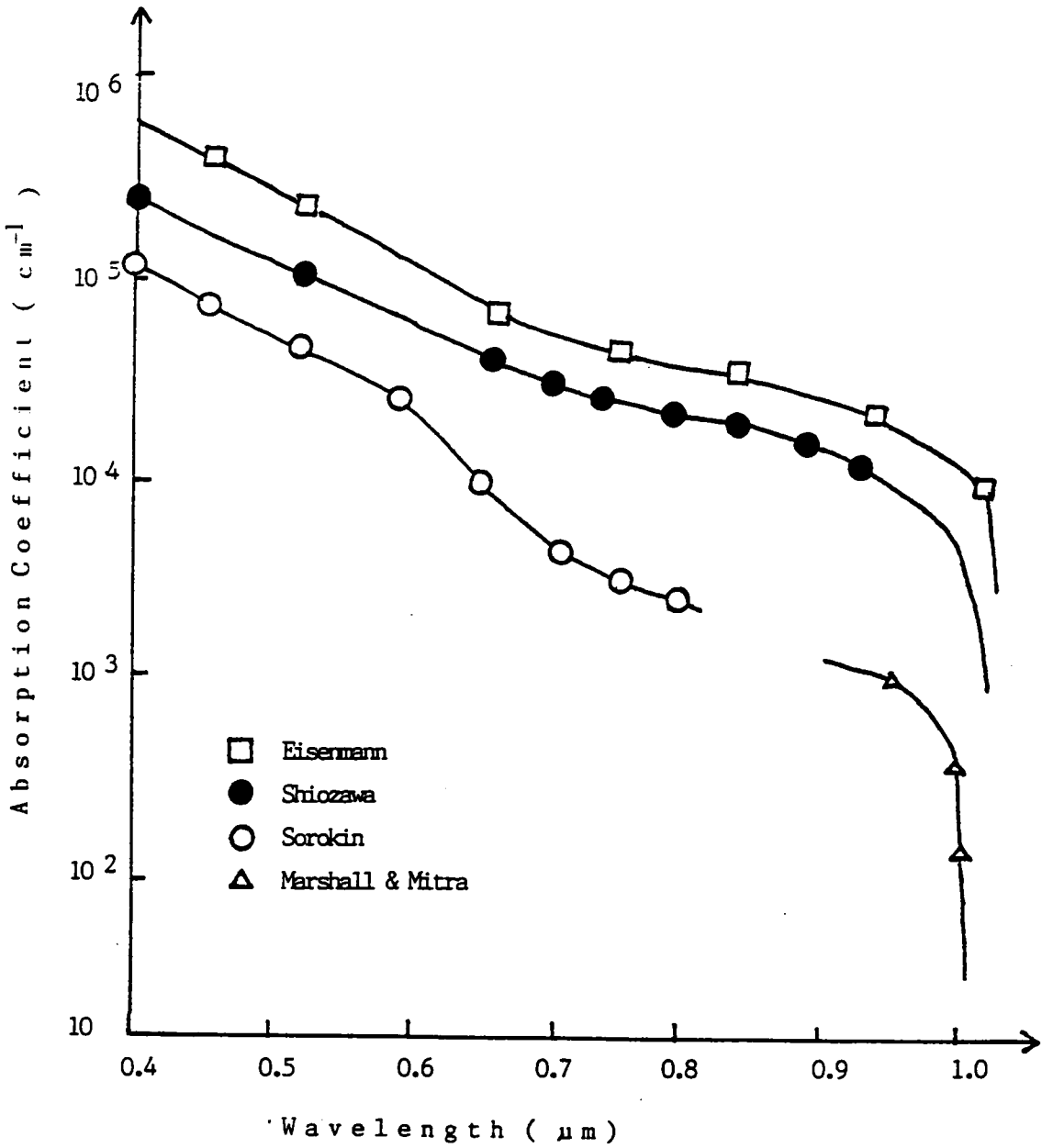

Figure 7: Absorption spectra for several polycrystalline Cu_2S films [31].

3) Electron Diffusion Length in the Cu_2S

Diffusion length is an important solar cell parameter which has a large effect on the short circuit current of the cell. Ideally, diffusion length should be as long as possible to obtain a high output current. The current density, as a function of Cu_2S thickness and diffusion length, is shown in Figure 8 [32]. Notice that the higher diffusion length gives the higher current density. The diffusion length is equal to $[kT\mu_n\tau_n/q]^{1/2}$. This indicates that the electron lifetime τ_n is related to the diffusion length. Several factors, such as grain boundaries, surface recombination, interface states and impurities, can affect the lifetime of the carriers; therefore, the diffusion length and the output current change accordingly.

4) Thickness of the Cu_2S

Figure 9 shows some calculated results of quantum efficiency as a function of the αd product, L/d ratio, and surface recombination velocity [33]. Here FWR stands for frontwall cell with reflection from back contact. The diffusion length should be equal to or greater than the thickness of the absorbing layer.

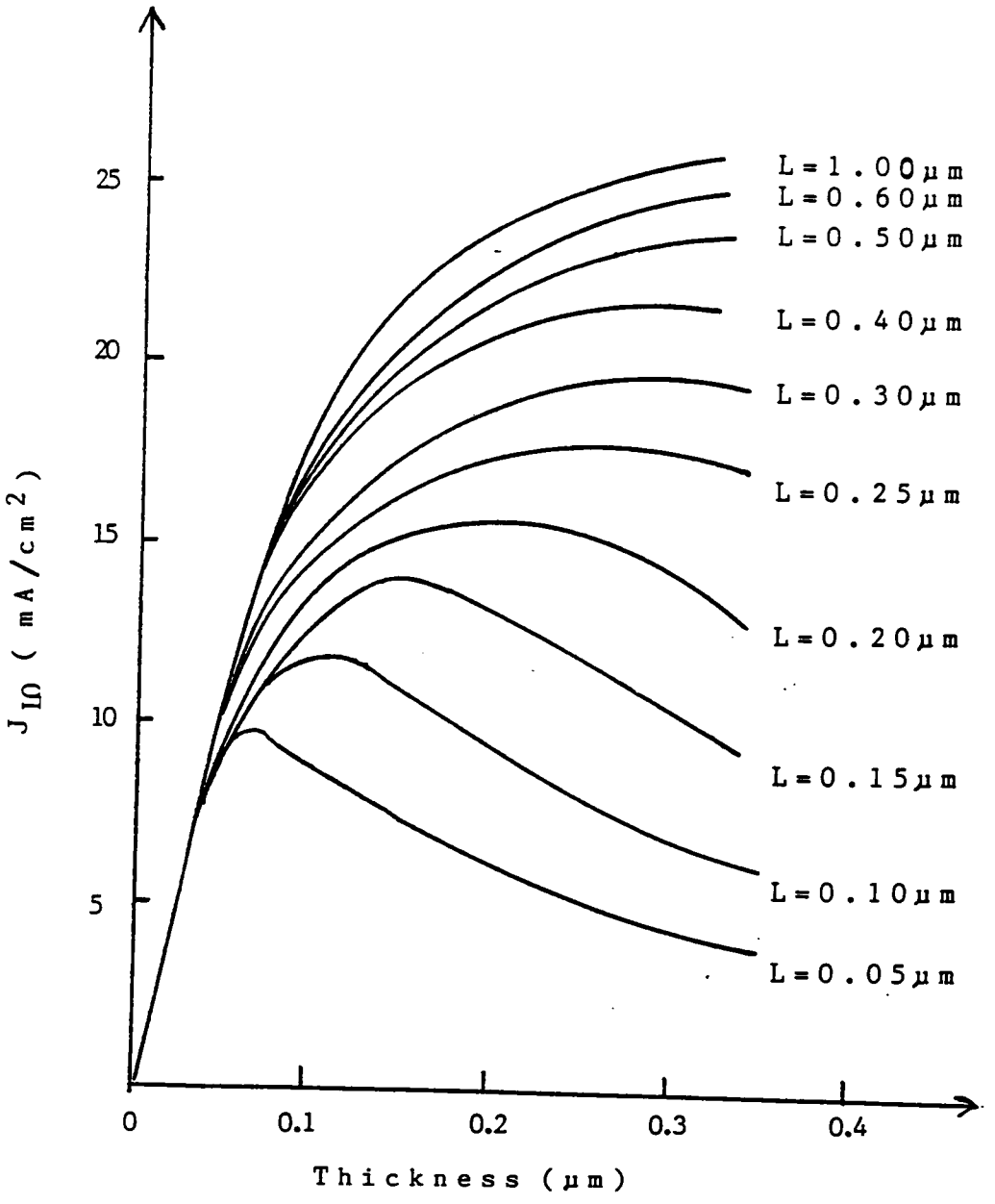

Figure 8: Current density as a function of Cu_2S thickness and diffusion length L [32].

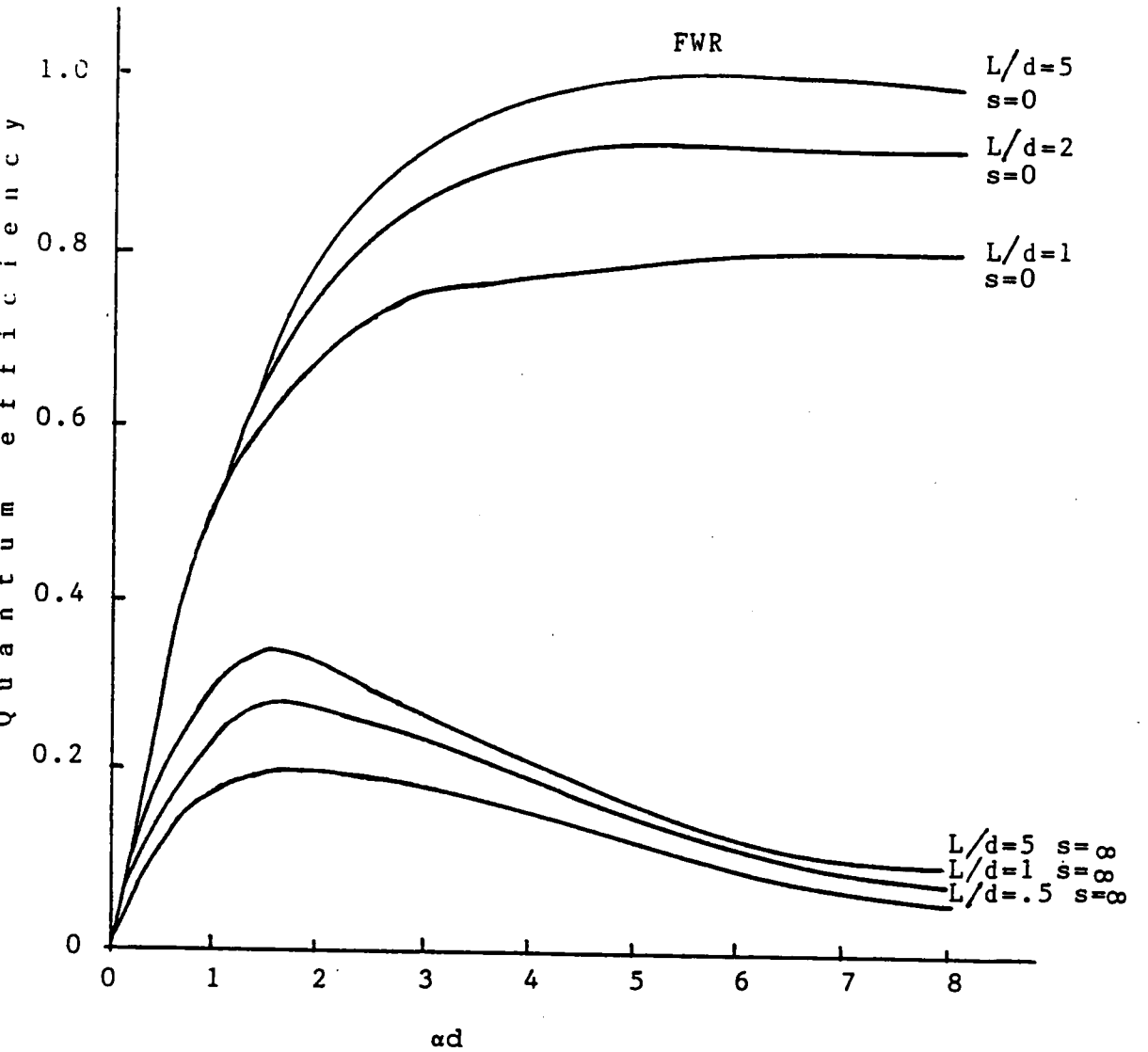

Figure 9: Calculated results of quantum efficiency as a function of αd product, L/d ratio, and surface recombination velocity.

5) Surface Recombination Velocity of the Cu_2S

The surface states act as recombination centers which reduce the short circuit current. In order to obtain a highly efficient solar cell, the surface recombination velocity must be small. ($S < 10^4$ cm/sec)

6) Drift Field in the Cu_2S

The existence of a drift field E_1 in the Cu_2S can increase the effective value of the diffusion length. For some values of E_1, the values of J_L can be increased about 10% over the E_1=0 case [34]. However, a drift field in the Cu_2S lowers the open circuit voltage due to the band bending in the Cu_2S, which reduces the band bending, and barrier height, in the CdS or ZnCdS.

7) Grain Size

The structural difference between single crystals and thin-film cells is the presence of grain boundaries. Because grain boundaries represent a source of recombination, they have important effect on the cells. The short circuit current can be reduced significantly if the grain size is too small.

Other factors which can affect J_L are the mode of operation of the cell (frontwall, backwall, and reflection modes), the intensity and spectral content of light source, the refrative index of the covering material, and the shading area of the contact grid.

For the ideal case, R_{SH} is approximately equal to infinity, and R_S is approximately equal to zero. When R_S and R_{SH} are neglected, the current-voltage characteristics of the Cu_2S/CdS solar cell, which is derived from equation (2-7), becomes

$$J = -J_L + J_o(e^{qV/AkT} - 1) \qquad (2\text{-}10)$$

when $J = 0$, $V = V_{oc}$. The V_{oc} equation is found to be

$$V_{oc} = \frac{AkT}{q} \ln \left[\frac{J_L}{J_o} + 1 \right] \qquad (2\text{-}11)$$

$$\text{or } V_{oc} \approx \frac{AkT}{q} \ln \frac{J_L}{J_o} \qquad (2\text{-}12)$$

Here J_o is the reverse saturation current and is given by

$$J_o = J_{oo} \exp^{-\phi_B/kT} \qquad (2\text{-}13)$$

and

$$J_{oo} = qN_c v \qquad (2\text{-}14)$$

where N_c is the density of the states in the conduction band; v is an effective velocity; and ϕ_B is the barrier height of the junction and is equal to $V_D + \Delta E$. (See Figure 2.)

Thus, the V_{oc} equation becomes

$$V_{oc} = \frac{\phi_B}{q} + \frac{kT}{q} \ln \frac{J_L}{qN_c v} \qquad (2\text{-}15)$$

Two cases can be considered: with and without interface states.

Case 1) Presence of interface states:

$v = S_I$ (interface state velocity)

$\phi_B = 0.9$ eV

$N_c = 2 \times 10^{18}$ cm^{-3}

The interface state recombination velocity can be evaluated from

$$S_I \approx v_{th} \sigma N_I \qquad (2\text{-}16)$$

where v_{th} is the electron thermal velocity ($\simeq 10^7$ cm/sec); σ is an electron capture cross section ($\simeq 10^{-14} - 10^{-15}$ cm^2); and N_I is the interface state density ($\simeq \frac{2\Delta a}{a_1 a_2}$), where a_1 and a_2 are the lattice constants of the Cu_2S and CdS respectively ($a_1 = 3.96$ Å, $a_2 = 4.14$ Å). Thus, $N_I \simeq 5 \times 10^{13}$ cm^{13}. Applying the above values in equation (2-15), $V_{oc} = 0.45 - 0.5$ V can be obtained. This is consistent with the experimental results for the Cu_2S/CdS solar cells.

Case 2) No interface state:

In this case, N_I is equal to zero. The barrier height, $\phi_B \simeq E_g(Cu_2S) = 1.2$ eV. J_o is controlled by diffusion currents and is represented by

$$J_o = qv_{eff}N_c\exp(-E_g/kT) \qquad (2\text{-}17)$$

where v_{eff} is the ratio of the electron diffusion length to lifetime, L_n/τ_n, and is roughly equal to 5×10^4 cm/sec. Using the above values in equation (2-15), the theoretical maximum, $V_{oc} \simeq 0.85$ eV, can be obtained.

Equation (2-15) shows clearly that an increase in V_{oc} can be obtained by increasing the barrier height, ϕ_B, and by reducing the interface state velocity, S_I. An increase in ϕ_B can be achieved by reducing both the electron affinity and

lattice mismatches, and a decrease in S_I can be achieved by better lattice match. Both the electron affinity and lattice mismatches can be reduced by using $Cu_2S/Zn_xCd_{1-x}S$ junction with $x \simeq 0.2$ instead of Cu_2S/CdS junction.

Several experimental results show that open circuit voltages obtained for the $Cu_2S/ZnCdS$ solar cells are indeed higher than those for the Cu_2S/CdS solar cells [18,35,36]. However, the increase in open circuit voltages is also accompanied by the decrease in short circuit current. In order to explain the reduction of short circuit current, it is necessary to understand the mechanisms of the $Cu_2S/ZnCdS$ heterojunctions. They can be discussed in three separate cell regions.

A) Cu_2S region

Several reports have proved that cadmium diffuses from the CdS into Cu_2S during the formation of Cu_2S/CdS cells [37,38]. $Cu_{1.995}Cd_{0.005}S$ was found in Cu_2S formed by wet ion exchange. For the $Cu_2S/ZnCdS$ solar cells, both cadmium and zinc will diffuse from ZnCdS into Cu_2S during the junction formation. If the doping density of cadmium or zinc is too high, the band bending will occur in the Cu_2S in the vicinity of the junction. Both the barrier height of the junction and the electric field in the ZnCdS will therefore be reduced. V_{oc} and I_{sc} will also be reduced.

B) Interfacial region between the Cu_2S and ZnCdS

This is the region which allows for the increase of the open circuit voltage. The increase of V_{oc} is due to a better electron affinity match between the Cu_2S and ZnCdS. Figure 10 shows three cases which can occur at the interface between the Cu_2S and ZnCdS. The first case (undermatched) corresponds to $Zn_xCd_{1-x}S$ for $x<0.1$. The second case (matched) occurs near $x=0.2$. The third case (overmatched) is for $x>0.3$. From this model, two interfacial effects, which could change the short circuit current, would be expected. One is the presence of a potential spike in the conduction band. This is caused by the excess zinc content at the interface (as in case 3 of Figure 10). This will result in a decrease in short circuit current. Another effect is the reduction in interface recombination velocity. This simply results from improved lattice match. From equation (2-8), one would expect that the short circuit current would increase as interface recombination velocity decreases, but this is not observed.

C) Compensated ZnCdS region

Both μ and E play important roles in collecting light generated current. Retention of zinc donors in Cu_2S increases the band bending in that layer, which causes the reduced E in the ZnCdS. The decrease in both μ and E can

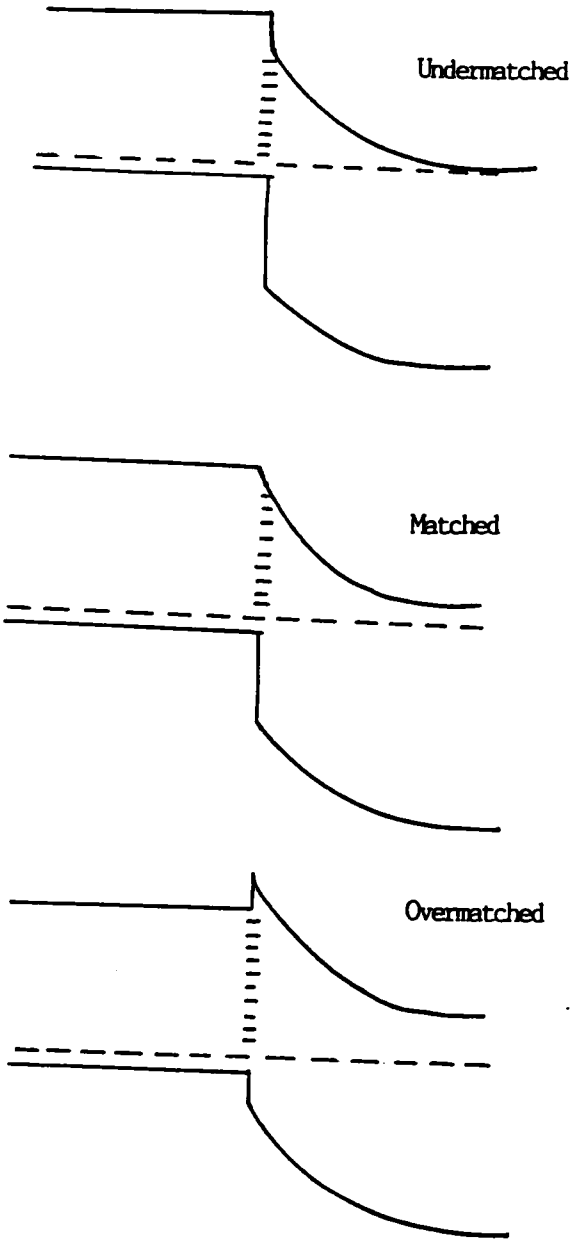

Figure 10: Band diagrams indicating three cases which can occur at the interface between Cu_2S and ZnCdS.

result in the decrease in short circuit current. This can easily be seen from the interface collection factor equation.

2.4 THE SPECTRAL RESPONSE AND THE ENHANCEMENT AND QUENCHING EFFECTS

A) Spectral response

When light with energy greater than the bandgap is incident upon the solar cells, photons are absorbed and electrons are raised from the valence band to the conduction band with the creation of electron-hole pairs. The minority carriers (holes in the n-side and electrons in the p-side of the junction) diffuse to the edges of the space charge region, and they recombine with majority carriers simultaneously. Those minority carriers which reach the junction can be swept across the junction by the electric field and will give rise to a photocurrent. The photocurrent moves in the opposite direction of the forward bias current in the dark. For the case of Cu_2S/CdS and Cu_2S/ZnCdS solar cells, incident photons are absorbed almost completely in Cu_2S because of its high absorption coefficient. The

contribution to the current from the CdS can usually be neglected.

There are four possible modes of operation for the Cu_2S/CdS or Cu_2S/ZnCdS heterojunction solar cells. These are a) frontwall mode (FW), b) backwall mode (BW), c) frontwall reflection mode (FWR), and d) backwall reflection mode (BWR). The light collected current of these cells, J_L, depends upon the absorption coefficient α of the Cu_2S , the thickness d of Cu_2S layer, the electron diffusion length L in the Cu_2S, the surface recombination velocity S_n, grain size R, the drift field in the Cu_2S, E_1, the interface recombination velocity S_I, and the drift field in the CdS E_2, for all modes of operation. The equation for J_L is

$$J_L = [1-(d/R)(1-d/3R)]\frac{\mu E_2}{S_I+\mu E_2} J_{LOO} \qquad (2\text{-}18)$$

where J_{LOO} is the value of J_{LO} in a single crystal.

The derivation of J_{LOO} can be seen as follows:

Assuming that the drift field in the Cu_2S is zero, and the electron density equation is

$$\frac{n(x)-n_o(x)}{\tau_n} = G(x) + \frac{kT\mu_n}{q}\frac{\partial^2 n}{\partial x^2} \qquad (2\text{-}19)$$

where G(x) is the generation rate of electrons, μ_n the electron molibity in Cu_2S, and τ_n the lifetime of the electron. The solution for this equation can be written as

$$n(x)-n_o = A \cosh(x/L) + B \sinh(x/L) + H[G(x)] \quad (2\text{-}20)$$

where H[G(x)] is a function of G(x). A and B can be determined by the boundary conditions and they also depend on G(x). The diffusion length $L=(D\tau_n)^{1/2} = (kT\mu_n\tau_n)^{1/2}$.

For the frontwall configuration (where the light is incident upon the cells from the Cu_2S side), the light is absorbed almost entirely in the Cu_2S, and G(x) is given by

$$G(x) = \eta\Phi_o\alpha\exp(-\alpha x) \quad (2\text{-}21)$$

where η is quantum efficiency, and Φ_o is the photon flux incident upon the cell. For this case H[G(x)] is given by

$$H[G(x)] = \frac{-\eta\Phi_o\alpha\tau_n\exp(-\alpha x)}{\alpha^2L^2-1} \quad (2\text{-}22)$$

Two boundary conditions, which can be used to solve equation (2-20), are

1) $qS_n(n-n_o) = qD\frac{\partial n}{\partial x}$ at $x = 0$

2) $n = n_o$ at the junction

The solution for J_{LOO} is

$$J_{LOO} = -\eta q \Phi_o \frac{\alpha L}{(\alpha^2 L^2 - 1)} [S+\alpha D - \exp(-\alpha d)\{(\frac{D}{L})[\sinh(\frac{d}{L}) + \alpha L \cosh(\frac{d}{L})]$$

$$+ S[\alpha L \sinh(\frac{d}{L}) + \cosh(\frac{d}{L})]\}][S\sinh(\frac{d}{L}) + (\frac{D}{L})\cosh(\frac{d}{L})]^{-1} \quad (2\text{-}23)$$

The J_{LOO} for other cases (the backwall mode, the frontwall reflection mode, and the backwall reflection mode) can also be derived in the same fashion. Figure 11 shows the typical spectral response of frontwall Cu_2S/CdS or Cu_2S/ZnCdS cells.

B) Enhancement and quenching effects

The spectral response of a solar cell often depends upon the sequence in which wavelengths are scanned. For the case of Cu_2S/CdS cells, the response for scanning from blue to red is higher than that for scanning from red to blue. This is due to the fact that some wavelengths ionize deep levels in the CdS, whereas other wavelengths fill the deep levels.

Enhancement and quenching effects can be seen by measuring the spectral response with bias light. Bias light of some wavelengths enhances the spectral response of the cell, while other wavelengths decrease or quench the response. Figure 12 gives a band diagram of the cell with deep traps. The enhancement of the spectral response results from the ionization of the deep traps which

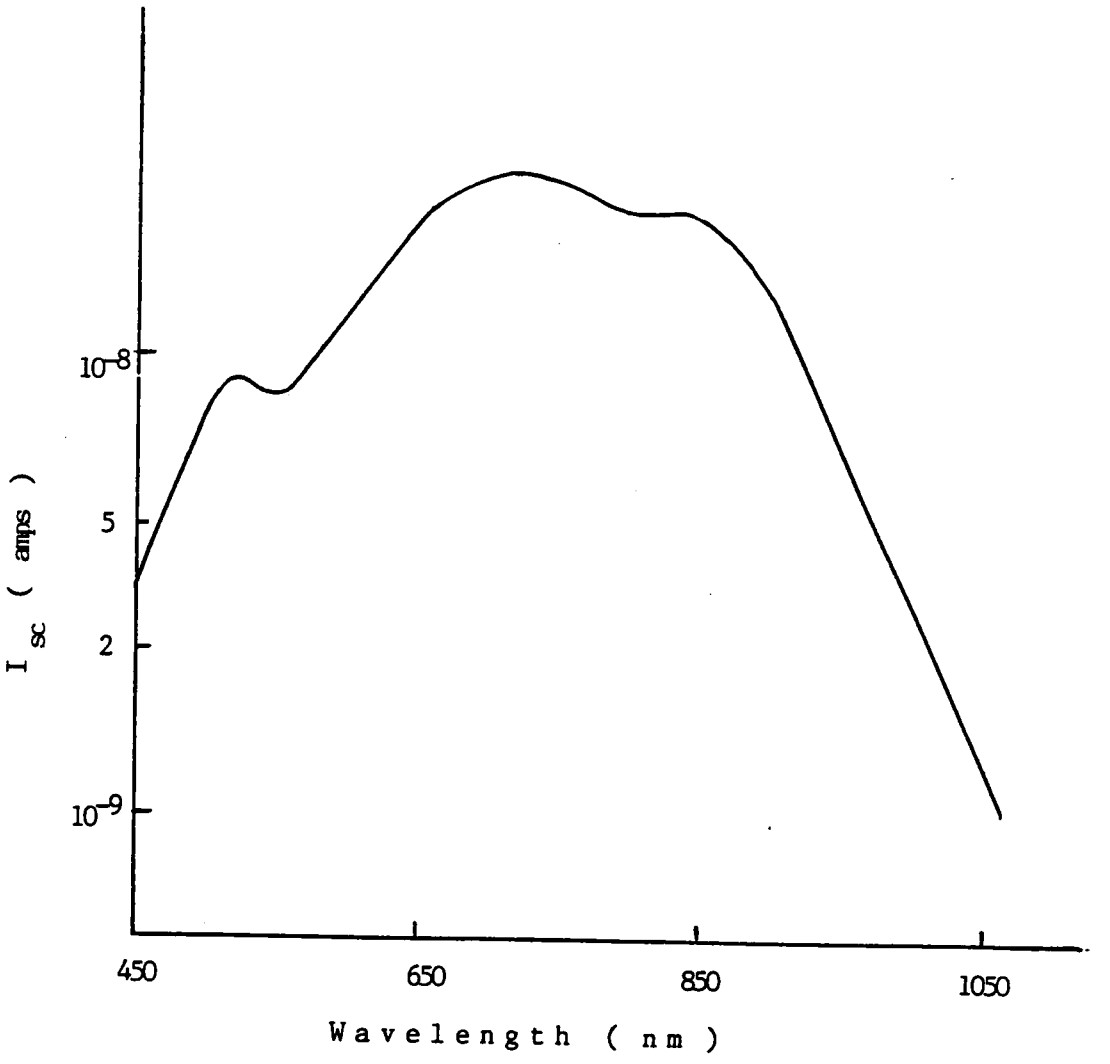

Figure 11: Typical spectral response of frontwall Cu_2S/CdS or $Cu_2S/ZnCdS$ cells.

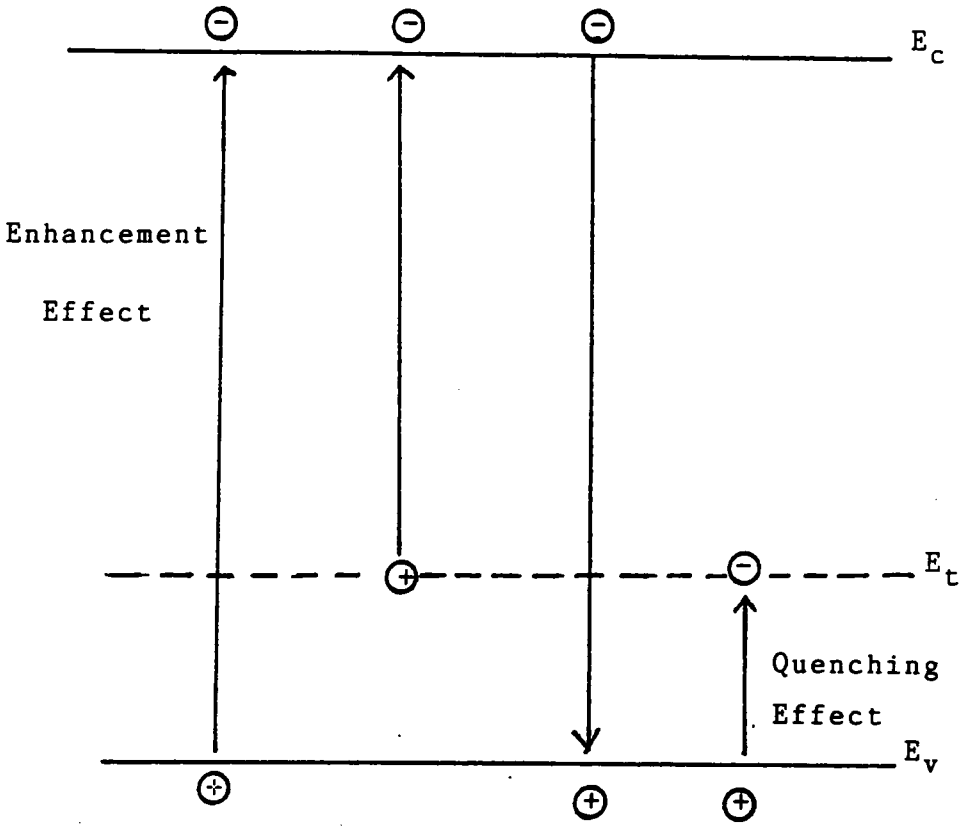

Figure 12: Energy band diagram with deep traps.

increases the positive charge in the depletion region and decreases its width. The shrinkage of the depletion width increases the electric field in this region. Therefore, the spectral response enhances. The quenching of the spectral response results from electron trapping by the deep traps. The electrons are excited from the valence band and trapped in this level. This trapping decreases positive charge in the depletion region and hence increases the depletion width. The increase of the depletion width results in a reduction of the electric field in this region. Therefore, the spectral response is decreased (quenched).

2.5 CAPACITANCE BEHAVIOR

Capacitance measurements have been used to obtain important information on the cell, including carrier concentration, diffusion voltage, and depletion width. For non-heat-treated Cu_2S/CdS or Cu_2S/ZnCdS solar cells, the junction is abrupt. The doping density of Cu_2S is much greater than that of CdS or ZnCdS, therefore, the transition capacitance per unit area can be expressed as

$$C = \left[\frac{q\varepsilon N}{2(V_D-V)}\right]^{1/2} \qquad (2\text{-}24)$$

$$\text{or} \quad \frac{1}{C^2} = \frac{2}{q\varepsilon N}(V_D - V) \qquad (2\text{-}25)$$

where ε is the dielectric constant; N is the carrier concentration; V_D is the diffusion voltage; and V is the applied voltage.

A plot of $1/C^2$ versus V should be linear for an abrupt junction, as shown in Figure 13. N and V_D can be determined from the slope and the intercept of the $1/C^2$ versus V plot. The depletion width of the junction can be obtained from the following equation:

$$C = \frac{\varepsilon}{W} \qquad (2\text{-}26)$$

For heat-treated cells, two straight lines can be seen on $1/C^2$ versus voltage plots, as shown in Figure 13 [39,40,41]. The capacitance-voltage characteristics of heat-treated Cu_2S/CdS heterojunctions have been studied by Hall and Singh [42]. Their analysis is based upon the fact that the heat treatment causes copper ions to diffuse into the CdS. Three regions with different densities occur in the CdS, as shown in Figure 14. The first region is close to the interface with a very high-doping density ($\approx 10^{19}$ cm^{-3}). Adjacent to this high-doping density region is a low-density compensated region. The presence of this layer is attributed to Cu diffusion from Cu_2S to CdS. Next to the

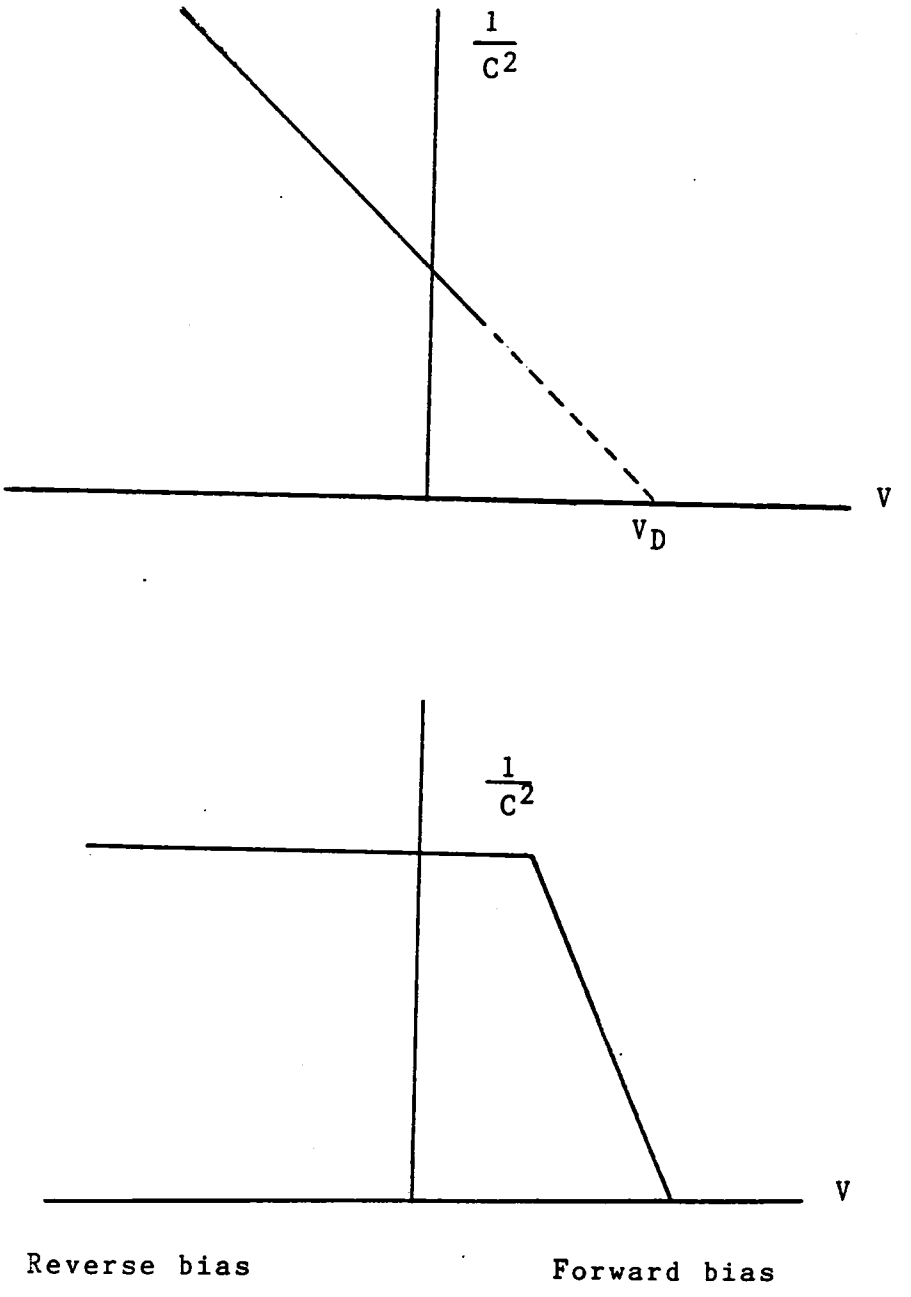

Figure 13: $1/C^2$ versus voltage for non-heat-treated and heat-treated Cu_2S/CdS heterojunctions [25].

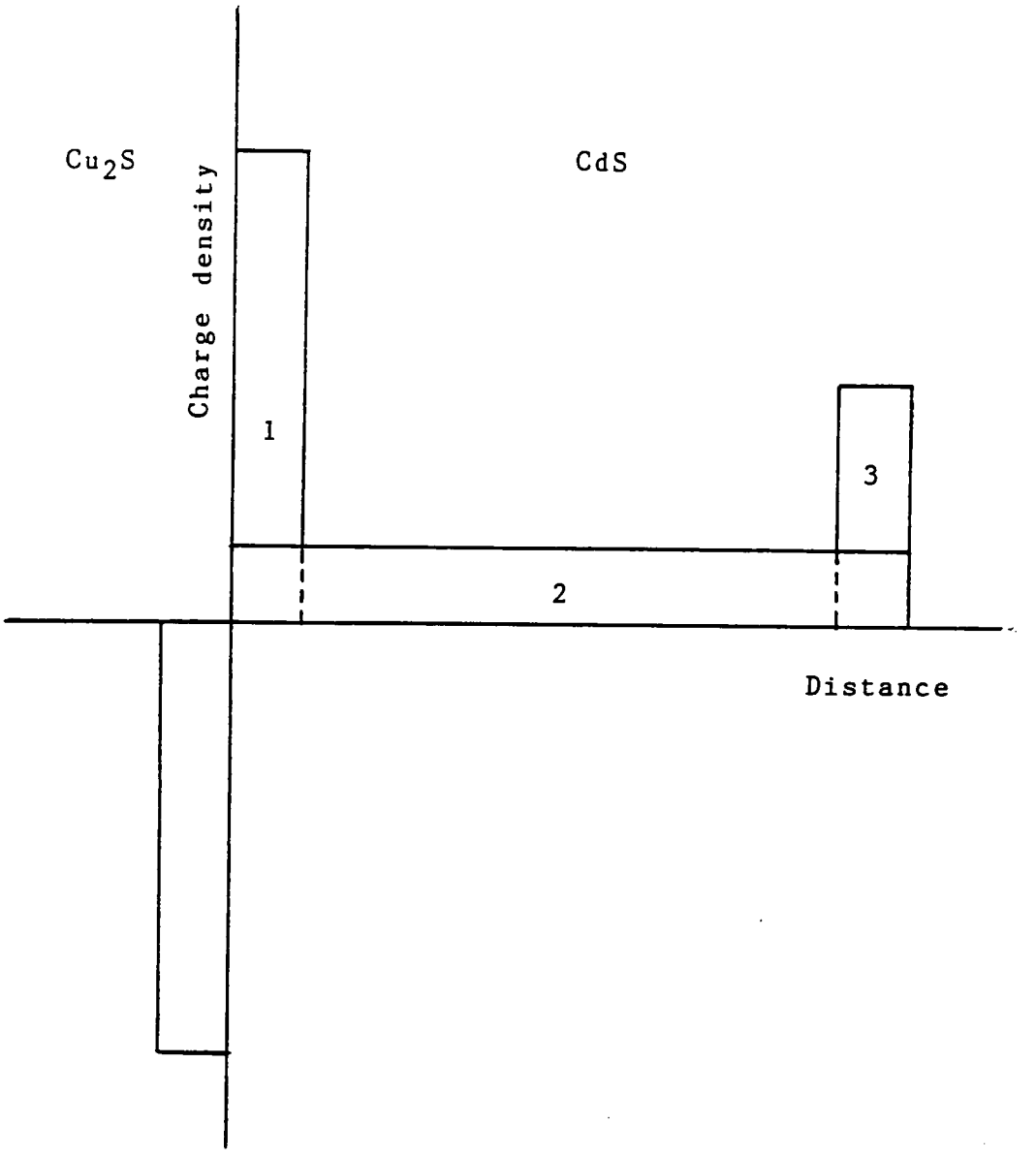

Figure 14: Space charge profile for Cu_2S/CdS solar cells [42].

compensated region is the bulk space charge region with shallow donor density of about 10^{17} cm^{-3}. Hall and Singh's results show that the $1/C^2$ versus voltage characteristic is a function of heat treatment, and that the depth of the Cu-compensated region in the CdS also depends on the heat treatment. This region is very important in the photoresponse of the junction.

2.6 DEEP ENERGY LEVELS

In order to produce high efficiency cells, heat treatment is necessary during fabrication of the Cu_2S/CdS and Cu_2S/ZnCdS junctions. During heat treatment, copper ions diffuse from the Cu_2S into the CdS or the ZnCdS layer, and Cd and Zn ions diffuse from the CdS or the ZnCdS into the Cu_2S. Anomalous effects, such as the cross-over between the light and dark I-V characteristics, enhancement and quenching of the spectral response, photocapacitance behavior, and time dependence on the open circuit voltage, can result from the deep energy levels that exist in the depletion region of the CdS or the ZnCdS layer. Several techniques can be used to determine the deep trap parameters

(trap energy level, capture cross section, and trap concentration). Some of these are listed below:

1) Frequency dependent capacitance [43,44]

2) Temperature dependent capacitance [45,46,47]

3) Voltage dependent capacitance [48,49,50]

4) Capacitance transient [51]

5) Photocapacitance [52,53]

6) Space-charge-limited current [54-59]

7) Thermally stimulated current [60,61,62]

8) Deep level transient spectroscopy [63,64,65].

Three methods considered in more detail below are based upon available equipment and applicability to these junctions. These techniques are photocapacitance, space-charge-limited current, and thermally stimulated current.

1) Photocapacitance

The effects of photocapacitance in p-n junctions have been considered as a powerful technique for studying deep traps in semiconductors. The quenching of photocapacitance has been applied to the study of deep energy levels in Cu_2S/CdS solar cells [47,48]. The general photocapacitance quenching spectrum for Cu_2S/CdS junctions can be seen in Figure 15.

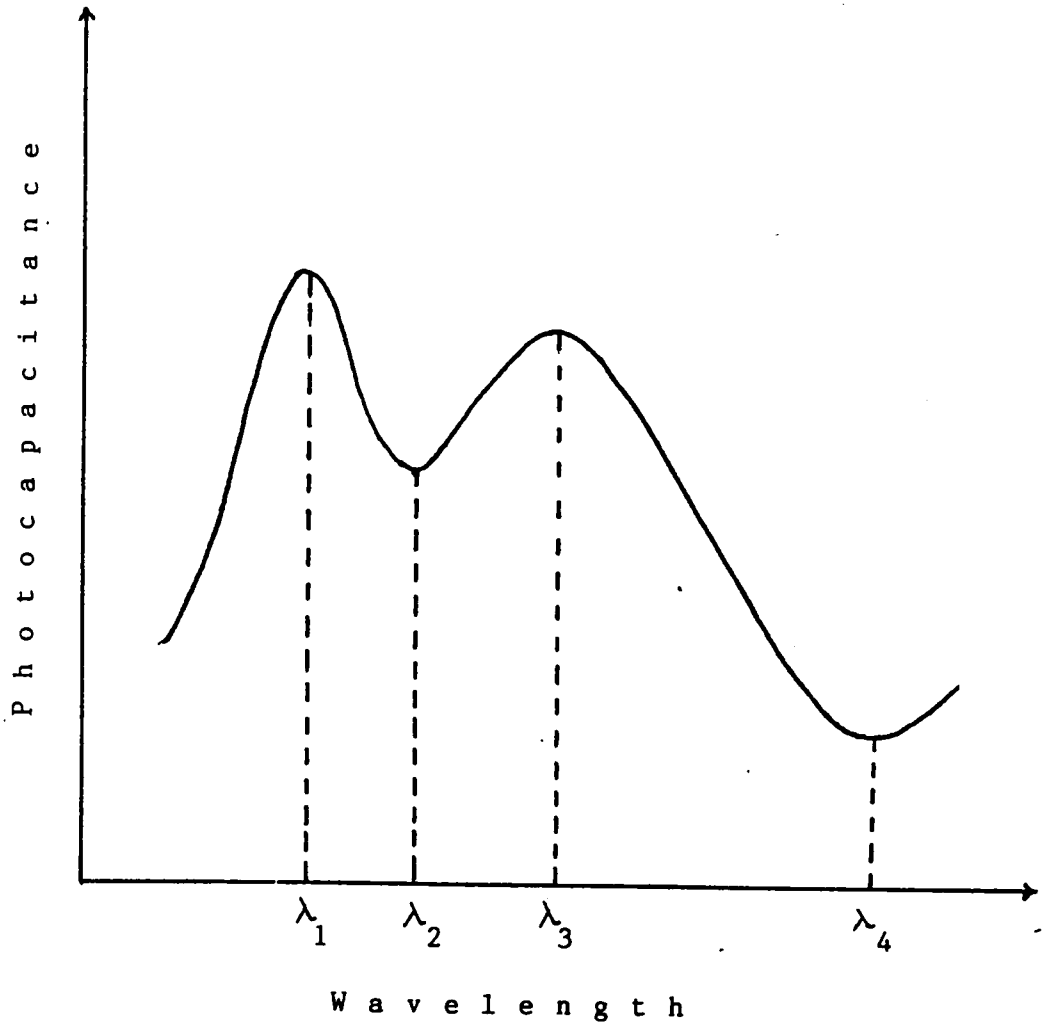

Figure 15: Photocapacitance quenching spectrum for Cu_2S/CdS junction [52].

Two peaks, at λ_1 and λ_3 can be seen in this figure. These two peaks correspond to two energy levels E_1 and E_3, as indicated in Figure 16. The peak in the photocapacitance at λ_1 can be attributed to the bandgap of the CdS. The peak at λ_3 results from the ionization of deep donor level in the CdS. The electrons in this level are excited to the CdS conduction band, with the result of a net increase in positive charge. Therefore, the photocapacitance increases.

Two minima are observed at λ_2 and λ_4. They correspond to deep acceptor energy levels in the CdS. These two acceptor levels occur at E_2 and E_4 above the valence band of the CdS. The minimum of photocapacitance can be explained by the trapping of the deep acceptor levels. The electrons are excited from the valence band and then trapped in these two levels. The trapping of electrons in these levels decreases the net positive charge. Therefore, the photocapacitance decreases.

2) Space-charge-limited current

Lampert developed a theory of space-charge-limited conduction in material with traps in 1956 [66]. The theory

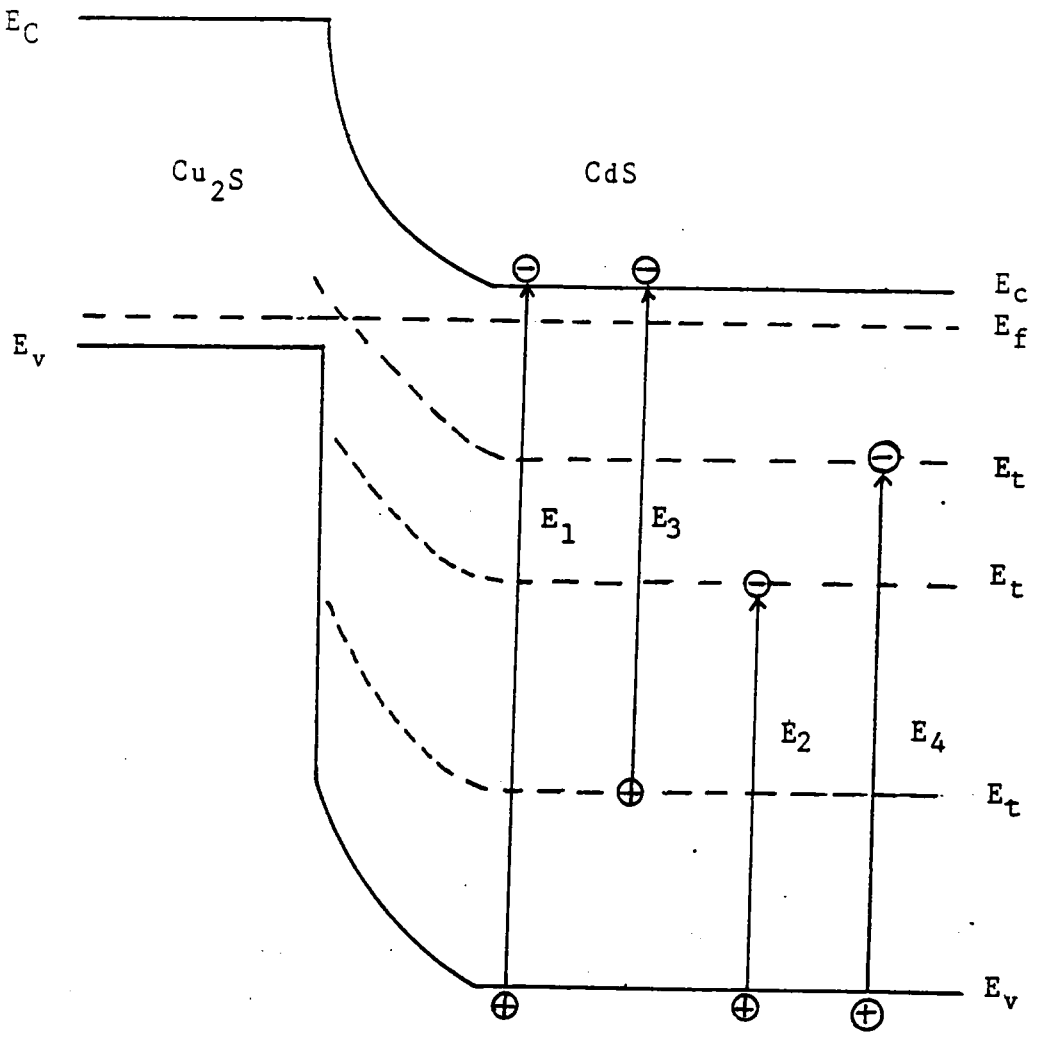

Figure 16: Energy band diagram with deep donor and deep acceptor traps.

illustrates several distinct regions in the I-V characteristic, as shown in Figure 17. At low voltages, Ohm's law is followed. At some applied voltages, most of the injected charge is trapped, and the current density is given by a square law relationship

$$J = \frac{\varepsilon \mu V^2}{d^3} \theta \qquad (2\text{-}27)$$

where ε is the permittivity, μ the electron mobility, V the applied voltage, d the electrode separation and θ a trapping factor,defined as

$$\theta = \frac{N_c}{N_t} \exp(-\frac{E_t}{kT}) \qquad (2\text{-}28)$$

where N_c is the density of states in the conduction band; N_t is the trap density; and E_t is the trap energy level.

At voltage V_{TFL}, all traps become filled; the relation between the trap- fill-limit voltage and the trap density is

$$V_{TFL} = \frac{ed^2}{2\varepsilon} N_t \qquad (2\text{-}29)$$

V_{TFL} obtained from the experimental results can be used to estimate N_t using equation (2-29). θ can be determined

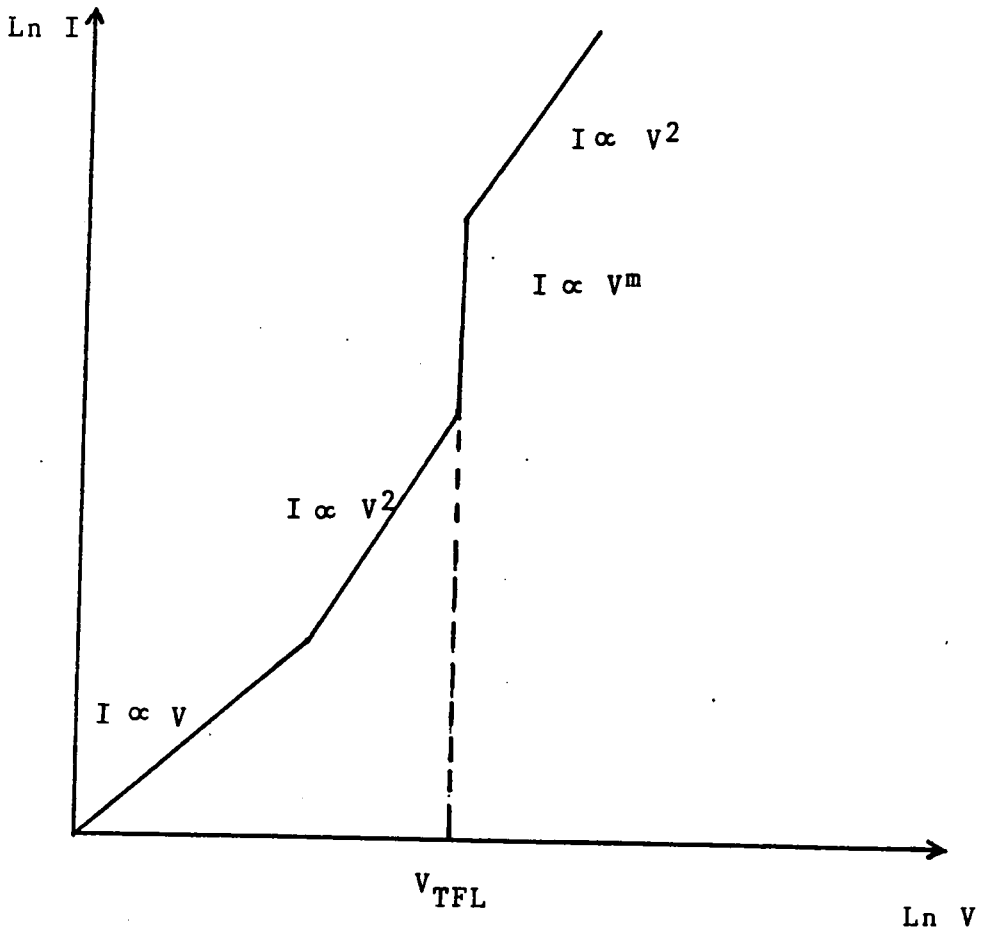

Figure 17: I-V characteristics for space-charge-limited current injection into material with a shallow trap.

from the square law characteristic, and E_t can be calculated from equation (2-28).

3) Thermally stimulated current

Thermally stimulated current involves the escape of electrons from the trapping center during the gradual warming up of the sample. This method is a powerful tool to evaluate the electron trapping parameters for both insulators and semiconductors. The thermally stimulated current can be expressed as [67].

$$\Delta\sigma = n_{to}\tau q\mu\nu\exp\left(-\frac{E_t}{kT} - \int_{T_o}^{T}\frac{\nu}{\beta}\exp\left(-\frac{E_t}{kT}\right)dT\right) \qquad (2\text{-}30)$$

where n_{to} is the density of filled traps, τ the lifetime of the free electron, μ the electron mobility, ν the attempt-to-escape frequency of a trapped electron, E_t a trap energy below the conduction band, T_o the temperature from which heating begins, and β the heating rate. A typical thermally stimulated current curve can be shown in Figure 18.

A number of methods can be utilized to evaluate the trap parameters from thermally stimulated current curve. One of

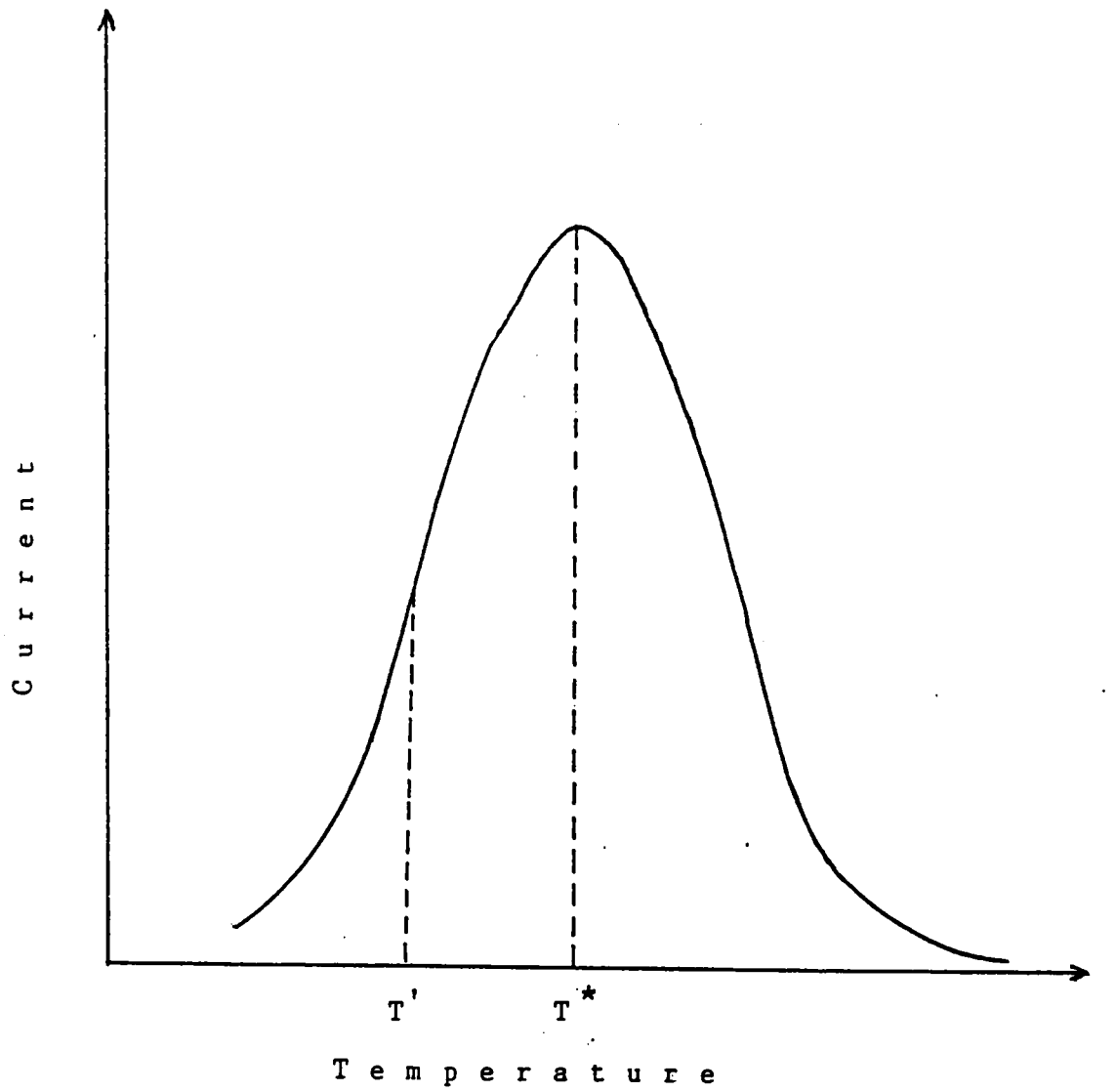

Figure 18: Typical thermally stimulated current curve.

them is Grossweiner's method [68]. This method is based on a simplification of equation (2-30). The trap energy E_t below the conduction band is given by

$$E_t = \frac{1.51kT^*T'}{T^*-T'} \qquad (2\text{-}31)$$

where k is the Boltzmann constant; T^* is the temperature of maximum current; T' is the temperature at which the current reaches half of the maximum value, as shown in Figure 18.

Chapter III

EXPERIMENTAL PROCEDURES

The experimental techniques used in this research can be divided into 4 sections: electrical, spectral, capacitance, and deep trap measurements. Electrical characterization measurements include I-V and $\ln(I_{sc})$ versus V_{oc} curves. Spectral measurements were made using one-beam and two-beam techniques [69,70]. Junction capacitances were measured in the dark. Deep trap characterization was accomplished using photocapacitance, space-charge-limited current, and thermally stimulated current measurements.

3.1 ELECTRICAL MEASUREMENTS

A) I-V measurements

The I-V characteristics of Cu_2S/CdS and Cu_2S/ZnCdS heterojunctions were measured in the same manner. The electrical schematic diagram and experimental set-up for these measurements are shown in Figure 19. A Cu_2S/CdS or Cu_2S/ZnCdS solar cell was connected in series with a one ohm resister and a Hewlett-Packard bipolar power supply (model 6825A). This series circuit was then connected in parallel with a Hewlett-Packard x-y recorder (model 7535B). A 300

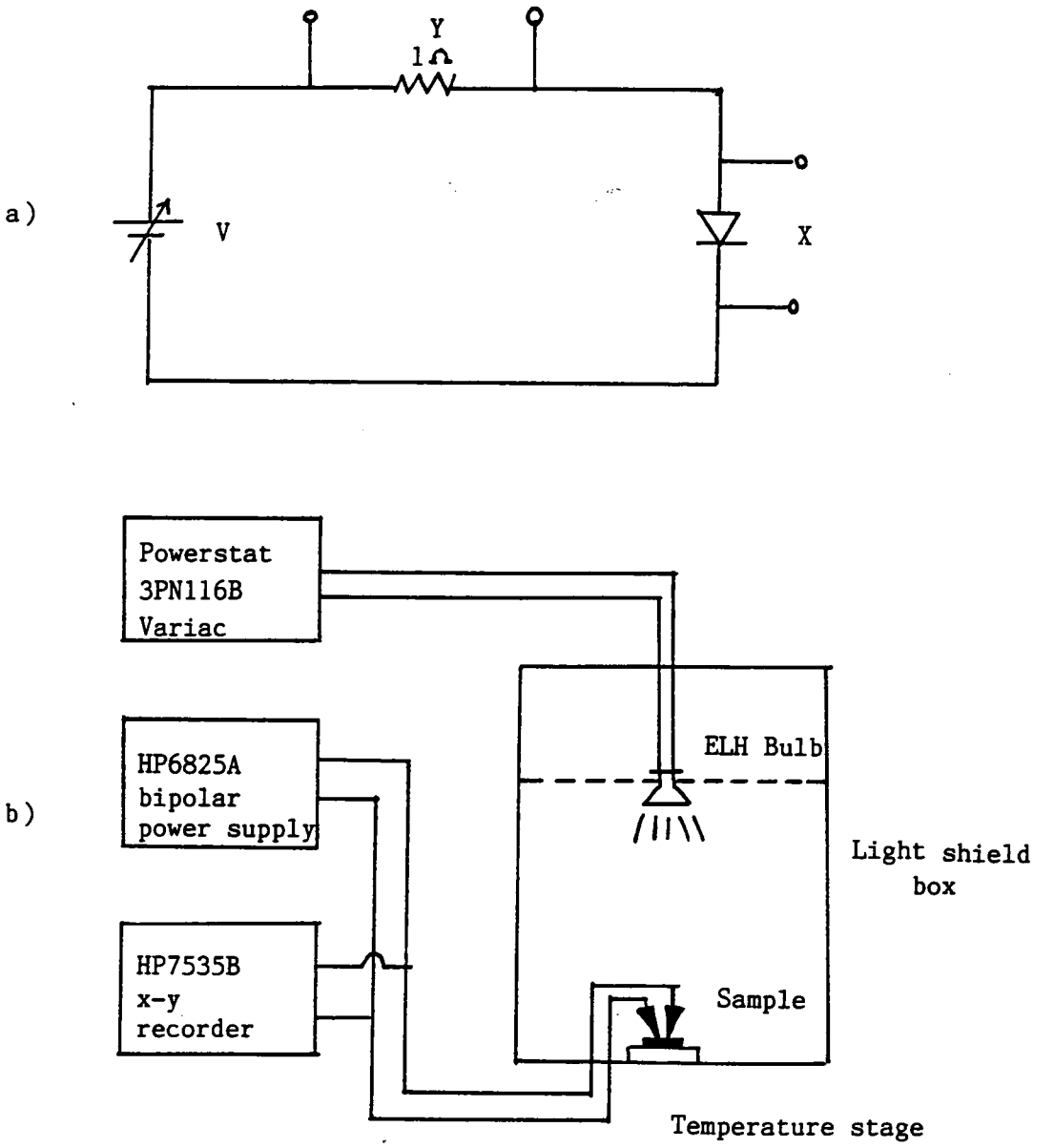

Figure 19: a) Electrical schematic diagram, and b) block diagram for the I-V measurements.

watt tungsten halogen projector lamp was used to simulate AM1 irradiance. The lamp's power intensity was adjusted to 100 mW/cm^2 by a variac. The cell was first measured in the dark. A dark I-V curve was traced on the x-y recorder by varying the voltage of the cell from reverse to forward bias. The cell was then exposed to an irradiance of 100 mW/cm^2. An I-V curve was obtained by varying the voltage of the cell from reverse to forward bias. Cell efficiency (η), fill factor (FF), short circuit current (I_{sc}), open circuit voltage (V_{oc}), series resistance (R_S), and shunt resistance (R_{SH}) of these cells can all be determined from the measured I-V curves (The parameters were defined in Section 2.3).

B) $\ln(I_{sc})$ versus V_{oc} measurements

$\mathrm{Ln}(I_{sc})$ versus V_{oc} measurements were used to determine junction parameters: reverse saturation current J_o, diode factor A, current density J_{oo}, and potential barrier height ϕ. The setup for these measurements is illustrated in Figure 20. The light source, which was used in the I-V measurements, was adjusted to the intensity of AM1. Neutral density filters were subsequently used to obtain lower levels of irradiance. The cells were mounted on a copper block which was connected to a Cambion temperature control unit. This temperature control unit includes a range extender (model 809-3048-01), a bipolar controller (model

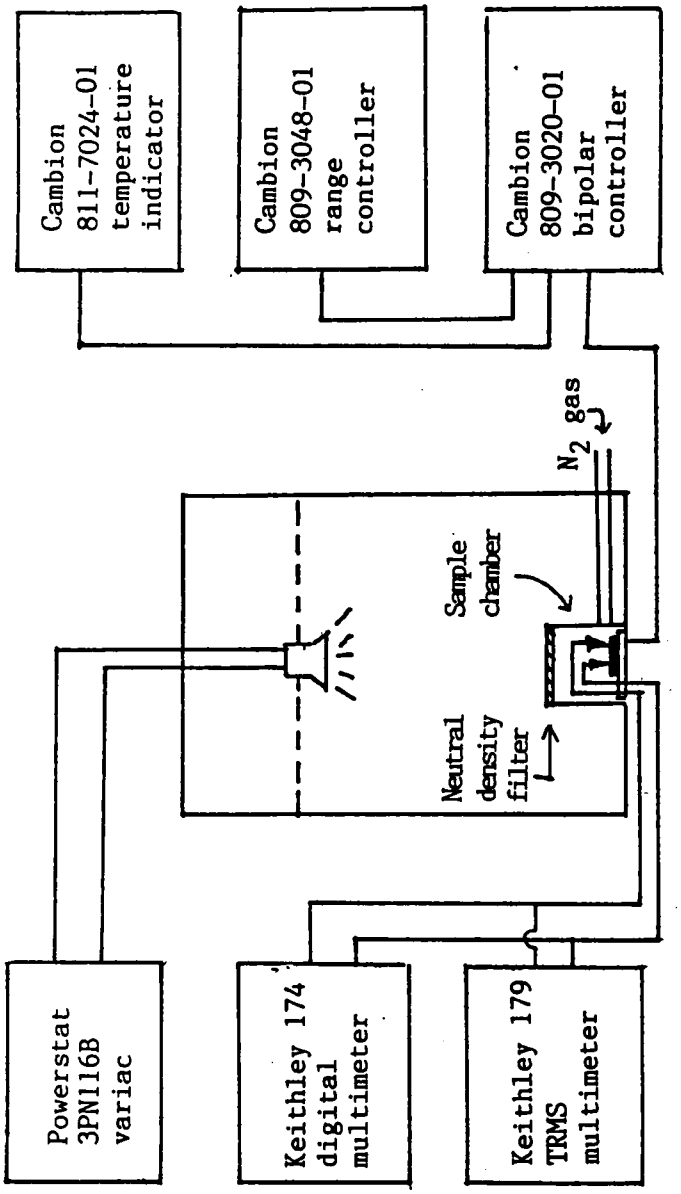

Figure 20: Set-up for the $\ln(I_{sc})$ versus V_{oc} measurements.

809-3020-01), and a digital temperature indicator (model 811-7024-01). The temperature can be adjusted in the range of -20 to 125°C. A Keithley digital multimeter (model 174) was used to measure V_{oc}, and a Keithley TRMS digital multimeter (model 179) was used to measure I_{sc}. V_{oc} and I_{sc} were measured at -15, 0, 15, 30, 45, and 60°C. No temperature higher than 60°C was applied during these measurements to avoid the degradation of the cells. These cells were placed inside a small chamber under the light source, as shown in Figure 21. N_2 gas was passed through this chamber to prevent vapor condensation on the cell during low temperature measurements. V_{oc} versus temperature for different levels of irradiance was also measured for these cells.

3.2 SPECTRAL MEASUREMENTS

Spectral measurements were used to determine the reasons for low or high photocurrent, especially minority carrier properties and surface recombination velocities. The set-up for these measurements is illustrated in Figure 22. A Jarrell-Ash monochromator (model 82-410) was used as a

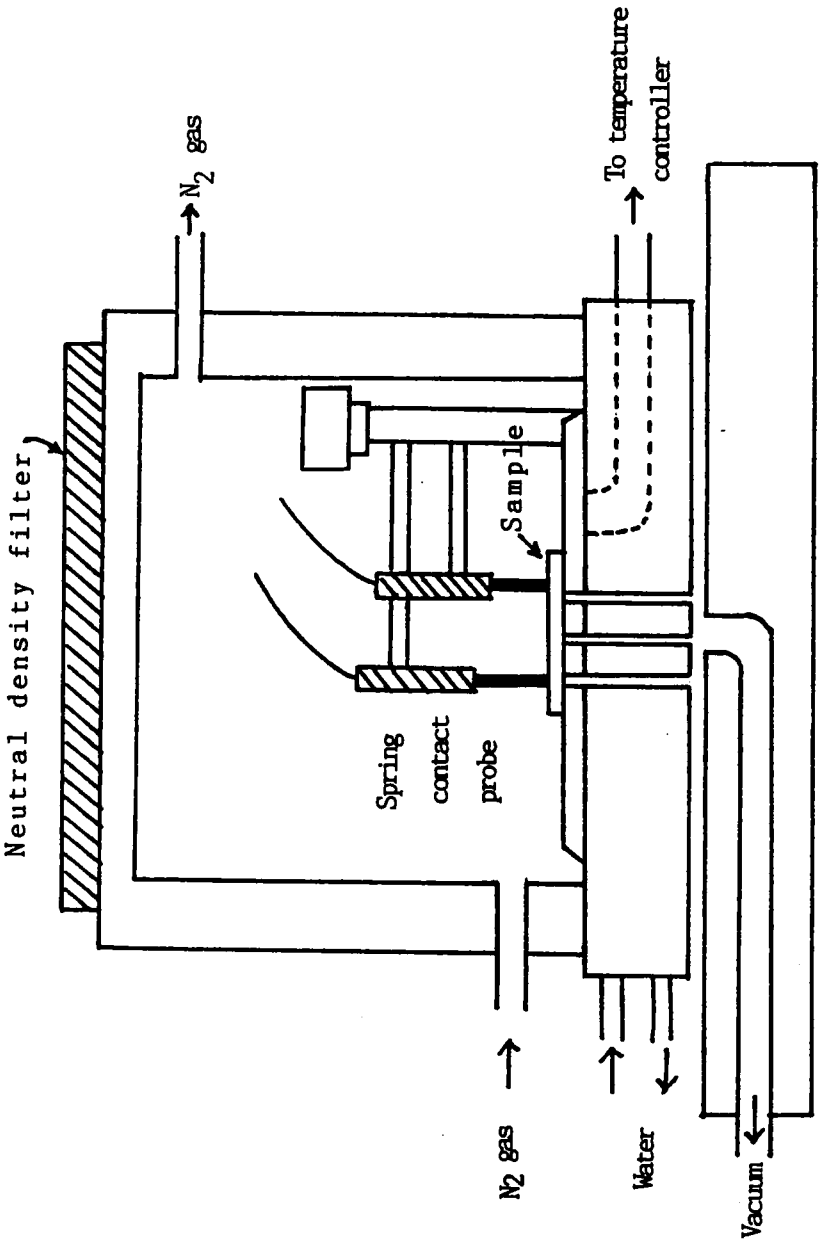

Figure 21: Sample chamber for the $\ln(I_{sc})$ versus V_{oc} measurements

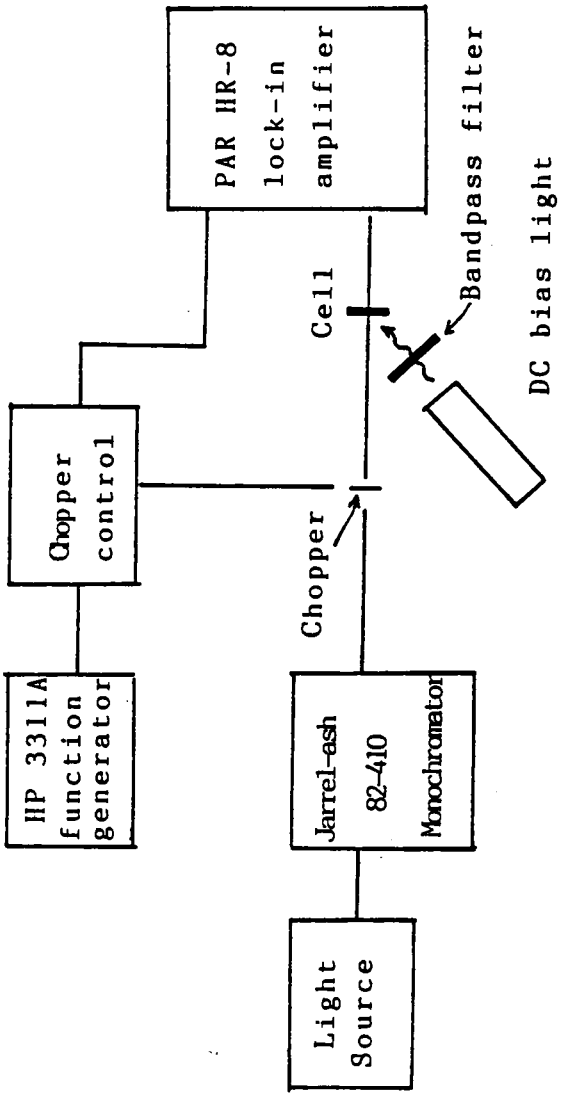

Figure 22: Set-up for the measurements of spectral response.

variable wavelength light source. A chopper, which was used to convert a DC light signal into an AC signal, was placed between this light source and a sample holder. A function generator (HP model 3311A) was used to drive the chopper at a frequency of 80 Hz. The Cu_2S/CdS or Cu_2S/ZnCdS cells were mounted in the sample holder with two leads connected to a PAR lock-in amplifier (model HR-8). This lock-in amplifier was then connected to a small resistor. The voltage drop across the resistor gave the output current of the samples. The input power of the samples was measured by replacing the sample holder with a photodetector, which was maintained at the same distance from the light source as the sample holder, and by recording the input power of the photodetector with a United Detector Technology optometer (UDT model 80X). Spectral measurements were made over a range of 450 to 1000 nm. Quantum efficiencies were obtained from the input power and the output current of the cells.

Enhancement and quenching of the quantum efficiency was studied by a two-beam technique. The light from a microscope lamp with a narrow bandpass filter was used as a primary beam, while the light from the monochromator was used as a secondary beam. Spectral responses were measured as a

function of the secondary beam wavelength for different light bias. Blue, red and white light were employed as light bias in these measurements.

3.3 CAPACITANCE MEASUREMENTS

Capacitance measurements were used in an effort to obtain important parameters of the cell, such as carrier concentration, diffusion voltage, and depletion width. These measurements were made using a Hewlett Packard impedance analyzer (model 4192A). The junction capacitance of Cu_2S/CdS and Cu_2S/ZnCdS cells were measured in the dark. (Variable wavelength photocapacitance measurements are described in the next section.) Capacitance as a function of an applied voltage, with frequency as a parameter, were measured for these cells. The voltage applied here was set between -1 and 0.3 V with 0.1 V increments. The measuring frequency was set at 100 Hz, 1 KHz, 10 KHz, and 100 KHz. Capacitance versus voltage curves were also measured as a function of temperature. Cell temperature was set at -15, 15 and 45^{o}C. These data were then plotted on linear paper as

C^{-2} versus V. Diffusion capacitance was also measured as a function of forward bias current to determine the mean lifetime of minority carriers in the interfacial regions.

3.4 DEEP TRAP MEASUREMENTS

A) Photocapacitance

The photocapacitance measurements were used to determine deep trap energy levels in the CdS and ZnCdS. The two-beam technique described in Section 3.2 was also applied in these measurements. The Hewlett-Packard impedance analyzer (model 4192A) was used to obtain the capacitance values. White, red, and green bias light were used during these measurements. The variation of photocapacitance (ΔC) was measured as a function of wavelength (λ).

B) Space-charge-limited current

Space-charge-limited current measurements were used to evaluate deep trap parameters, including trap energy levels and trap densities. A Hewlett-packard DC power supply (model 6113A), a Keithley digital multimeter (model 174), and a Keithley TRMS multimeter (model 179) were used in these measurements. These measurements were carried out in the dark.

C) Thermally stimulated current (TSC)

TSC measurements were applied to obtain trap energy levels. These measurements were conducted below room temperature. The schematic diagram for these measurements is shown in Figure 23. A low temperature cryostat, which gave controlled temperature from -175 to 25°C, was used in this setup. Two containers were used here. The first container with a copper coil in it was filled with liquid nitrogen. The nitrogen gas was passed through the copper coil. This gas was cooled to the boiling temperature of the liquid nitrogen when passing through the first container. The cool gas was then passed through the sample holder in the second container. The Cu_2S/CdS or Cu_2S/ZnCdS solar cells were mounted on this sample holder, and four wires led out from it. Two of these wires (thermocouple wires) were connected to an Omega temperature indicator (model 175) to monitor the cell temperature. The other two wires from the solar cell were connected to the electrical equipment, the HP power supply (model 6113A) and the Keithley TRMS multimeter (model 179). Before the cooling process began, the pressure in the second container was reduced to below 10^{-3} Torr by a mechanical pump to prevent vapor condensation on the cell.

A typical TSC procedure is as follows: The solar cell was first kept in the dark and subjected to a forward bias.

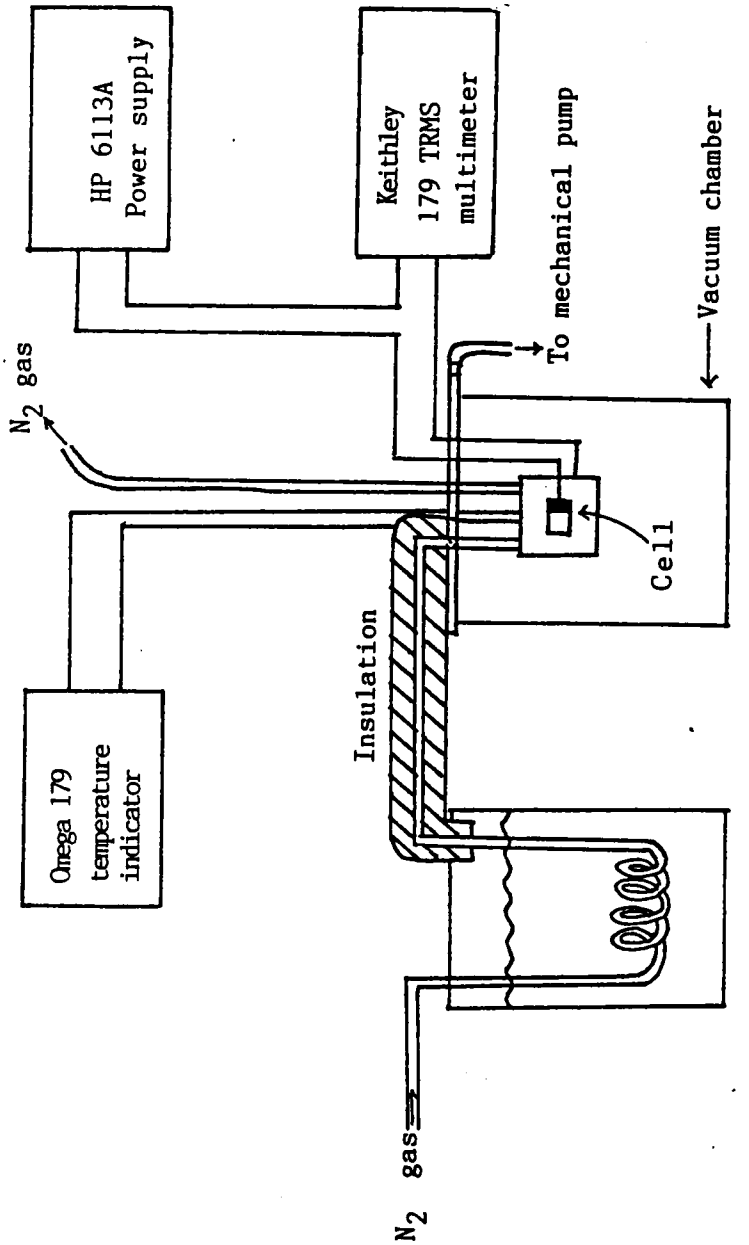

Figure 23: Schematic diagram for thermally stimulated current measurements.

The cell was then cooled to -175^{o}C and maintained there for 5-10 minutes. The voltage bias was then removed, and the thermally stimulated current was measured while the temperature of the cell was increased. Temperature was increased at 0.2 degree/sec by reducing the N_2 flow rate.

Chapter IV

RESULTS AND DISCUSSION

Cu_2S/CdS and $Cu_2S/Zn_xCd_{1-x}S$ solar cells manufactured by Chevron Research Company (Standard Oil of California) and the Institute of Energy Conversion (University of Delaware) were measured in this research. Results of these measurements are presented and discussed here. They are divided into four sections: electrical, spectral, capacitance, and deep trap measurements.

4.1 ELECTRICAL MEASUREMENTS

A) Current-Voltage (I-V) Measurements

I-V measurements can be used to determine cell parameters. These parameters include short circuit current (I_{sc}), open circuit voltage (V_{oc}), series resistance (R_S), shunt resistance (R_{SH}), fill factor (FF), and cell efficiency (η). Typical I-V characteristics of Cu_2S/CdS or $Cu_2S/Zn_xCd_{1-x}S$ cells are shown in Figure 24. The important cell parameters are listed in Table 1. (At least 4 cells were measured for each cell type.) It can be seen that V_{oc} values of $Cu_2S/Zn_xCd_{1-x}S$ cells are larger than those of Cu_2S/CdS cells. These results are expected. The increase of

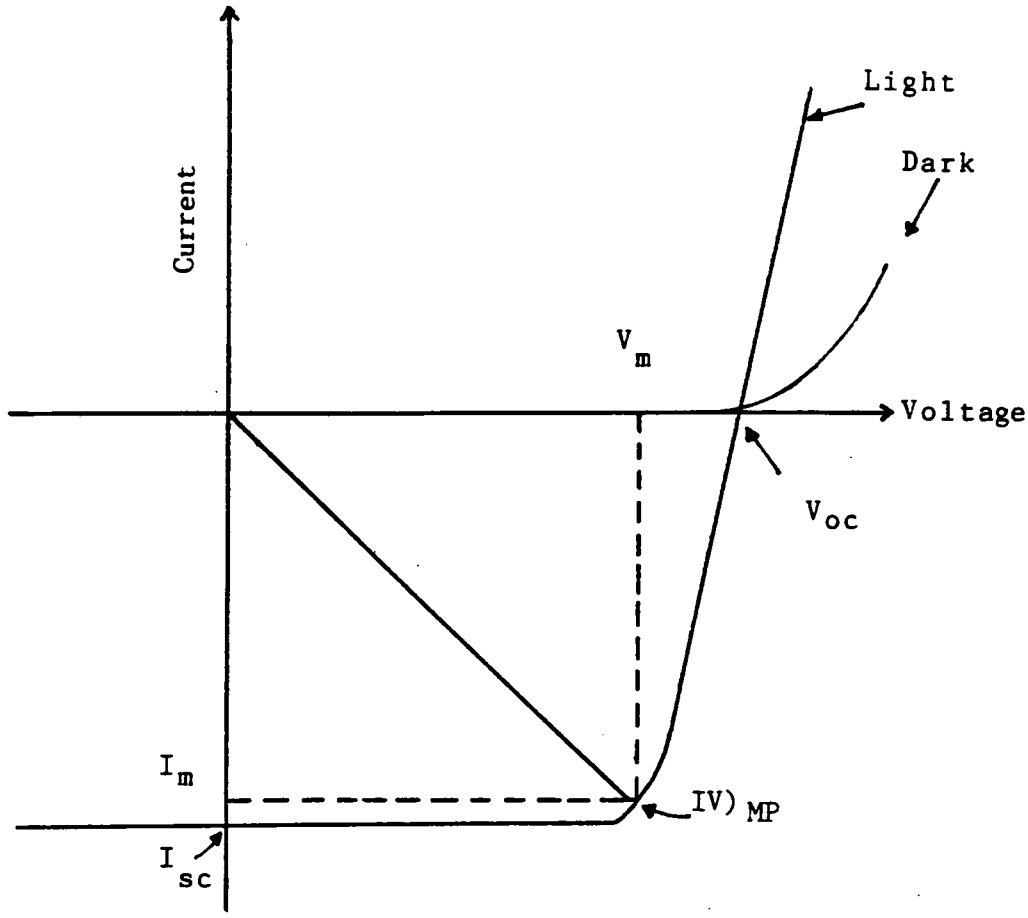

$$FF = \frac{IV)_{MP}}{I_{sc}V_{oc}} \qquad \eta = \frac{I_{sc}V_{oc}FF}{P_{in}}$$

Figure 24: Typical I-V characteristics of Cu_2S/CdS or $Cu_2S/Zn_xCd_{1-x}S$ cells. P_{in} is input power.

Table 1

Electrical parameters for Cu_2S/CdS and $Cu_2S/ZnCdS$ cells. Cell areas = 1 cm^2.

Sample	I_{sc} (mA)	V_{oc} (V)	R_S (Ω)	R_{sh} (Ω)	FF (%)	η (%)
Chevron Cu_2S/CdS 27A-4	8.9	0.51	2.53	660	70	3.3
Chevron $Cu_2S/Zn_{0.11}Cd_{0.89}S$ 04D-4	6.3	0.59	7.29	600	62	2.6
Chevron $Cu_2S/Zn_{0.25}Cd_{0.75}S$ 10C-4	5.4	0.62	5.76	250	63	2.4
IEC Cu_2S/CdS 470-11-2	16.5	0.51	2.07	610	72	6.9
IEC $Cu_2S/Zn_{0.12}Cd_{0.88}S$ 390-11-2	17.0	0.59	2.57	720	73	8.3
IEC $Cu_2S/Zn_{0.16}Cd_{0.84}S$ 389-11-4	16.5	0.60	2.27	700	74	7.8

V_{oc} is due to a better electron affinity match between Cu_2S and $Zn_xCd_{1-x}S$ [16]. Series resistances of $Cu_2S/Zn_xCd_{1-x}S$ cells are generally higher than those of Cu_2S/CdS cells. This results from the increased resistance of $Zn_xCd_{1-x}S$. For the Chevron cells, I_{sc}, FF, and η decrease as the content of Zn of $Zn_xCd_{1-x}S$ increases. These results are similar to those reported by Burton et al [71,72]. For the IEC cells, I_{sc} and FF of $Cu_2S/Zn_xCd_{1-x}S$ cells are close to the values of Cu_2S/CdS cells. The cell efficiencies (η) of $Cu_2S/Zn_xCd_{1-x}S$ cells are greater than those of Cu_2S/CdS cells due to the increase of V_{oc}. These results can be attributed to different fabrication conditions. (For example, CdS and $Zn_xCd_{1-x}S$ are etched in HCl for different periods of time.)

B) $Ln(I_{sc})$ versus V_{oc} Measurements

The electrical properties of the cell can be partly characterized by two diode parameters, the reverse current density J_{oo} and the potential barrier height ϕ. The values of J_{oo} and ϕ can be obtained by measuring the short circuit current I_{sc} and open circuit voltage V_{oc} under different illumination intensities. Assuming that both shunt resistance and series resistance can be neglected, the relation between J_{sc} and V_{oc} can be expressed as

$$J_{sc} = J_o \exp\left(\frac{qV_{oc}}{AkT}\right) \qquad (4\text{-}1)$$

From measurements of J_{sc} and V_{oc} at different irradiance levels, the diode factor A can be determined by the slope of a $\ln(J_{sc})$ versus V_{oc} plot, and J_o can be calculated from equation (4-1) for different temperatures. J_{sc} versus V_{oc} curves for a typical Cu_2S/CdS cell, at different temperatures, are shown in Figure 25. Tabulated values of A and J_o for the cell shown in Figure 25 are listed in Table 2. Other Cu_2S/CdS cells show similar results.

J_o can be expressed by the following equation

$$J_o = J_{oo}\exp(\frac{-\phi}{kT}) \qquad (4\text{-}2)$$

where J_{oo} is the current density and ϕ is the potential barrier height. The reverse current density J_{oo} can be obtained from the intercept of this plot, and ϕ can be obtained from a $\ln(J_o)$ versus 1/T plot. Figure 26 illustrates the $\ln(J_o)$ versus 1/T for the cell shown in Figure 25. Because results obtained from other Cu_2S/CdS cells were similar, they are not ploted here. The results of J_{oo} and ϕ under various levels of irradiance for 5 different Cu_2S/CdS cells are tabulated in Table 3.

An alternate technique to evaluate potential barrier height is to measure the open circuit voltage as a function of temperature. The potential barrier height can be obtained by the extrapolation of V_{oc} to zero degrees Kelvin.

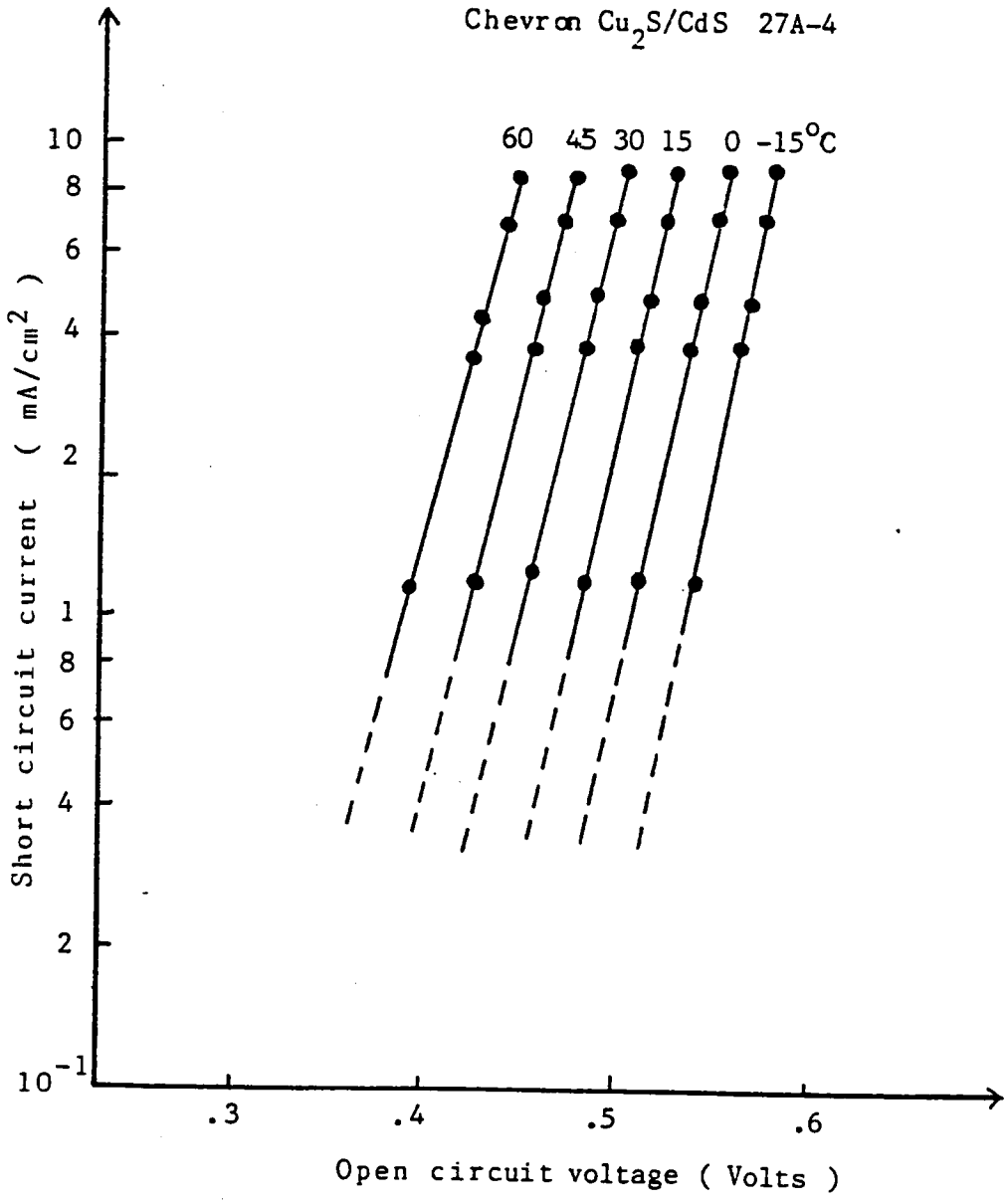

Figure 25: $Ln(J_{sc})$ versus V_{oc} for a typical Cu_2S/CdS cell at different temperatures.

TABLE 2

Values of A and J_o for Cu_2S/CdS, $Cu_2S/Zn_{0.11}Cd_{0.89}S$, and $Cu_2S/Zn_{0.25}Cd_{0.75}S$ cells, at six temperatures.

Sample		-15°C	0°C	15°C	30°C	45°C	60°C
Cu_2S/CdS	A	0.96	0.98	0.98	0.95	0.97	0.99
27A-4	J_o(ma)	1.55×10^{-11}	3.12×10^{-10}	3.06×10^{-9}	1.55×10^{-8}	1.55×10^{-7}	1.56×10^{-6}
$Cu_2S/Zn_{0.11}Cd_{0.89}S$	A	1.03	1.01	0.96	0.99	0.96	0.92
04D-3	J_o(ma)	2.62×10^{-12}	3.51×10^{-11}	3.99×10^{-10}	3.06×10^{-9}	2.14×10^{-8}	1.25×10^{-7}
$Cu_2S/Zn_{0.25}Cd_{0.75}S$	A	1.22	1.20	1.18	1.18	1.17	1.15
10C-1	J_o(ma)	2.34×10^{-10}	1.60×10^{-9}	9.76×10^{-9}	4.66×10^{-8}	2.15×10^{-7}	9.08×10^{-7}

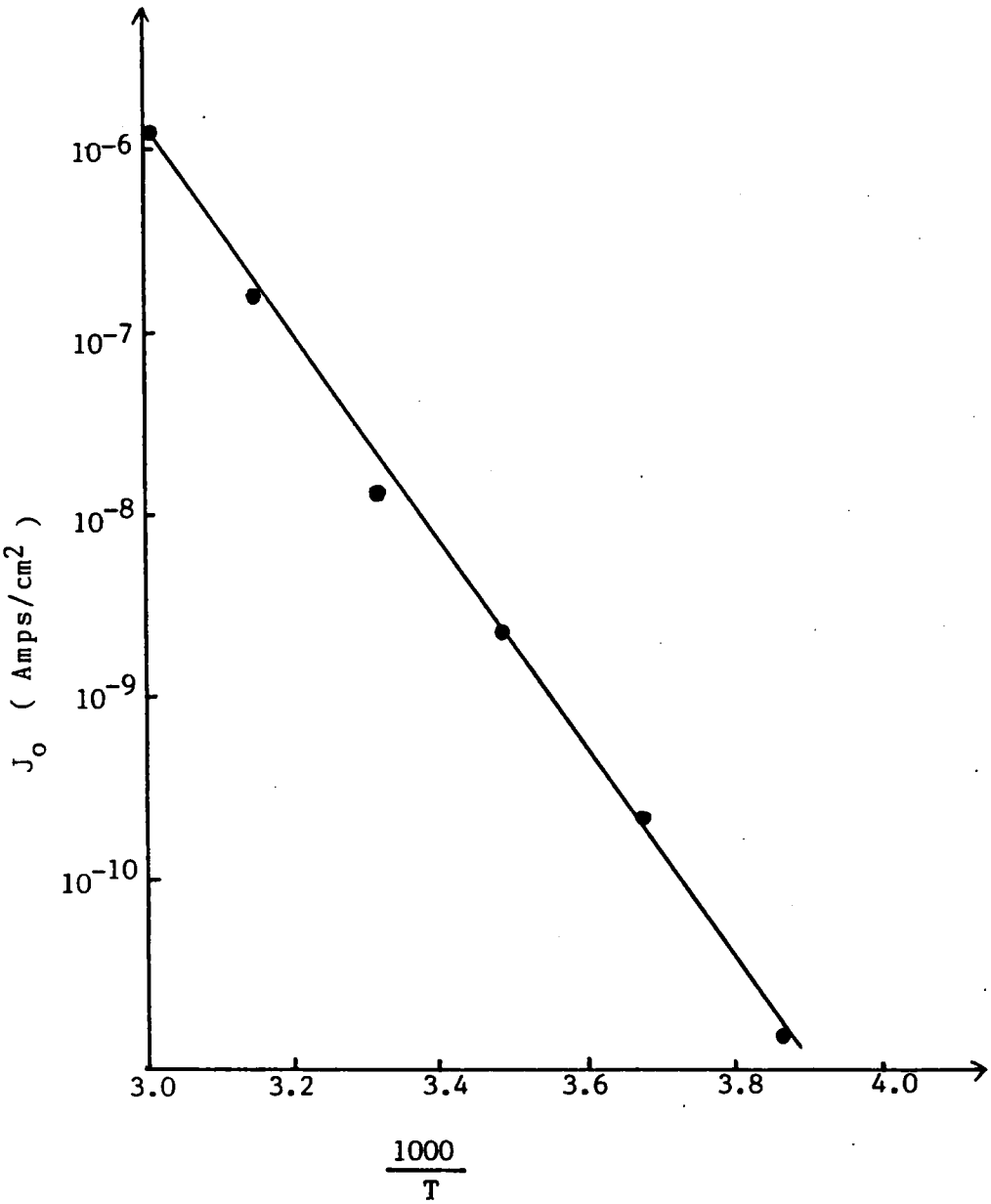

Figure 26: Ln(J_o) versus 1/T for a Cu_2S/CdS cell.

TABLE 3

Values of J_{oo} and ϕ under various levels of irradiance for 5 different Cu_2S/CdS solar cells. ϕ is the potential barrier height obtained from a plot of $\ln(J_o)$ versus $1/T$, and ϕ_1 is the potential barrier obtained from a V_{oc} versus T plot.

Sample		100% AM1	79% AM1	50% AM1	40% AM1
Cell 27A-1	ϕ_1(eV)	1.015	1.013	1.015	1.013
	ϕ(eV)	1.011	1.011	1.012	1.010
	J_{oo}(A/cm^2)	3.62×10^{6}	3.46×10^{6}	3.58×10^{6}	3.22×10^{6}
Cell 27A-2	ϕ_1(eV)	1.042	1.039	1.039	1.039
	ϕ(eV)	1.038	1.035	1.034	1.034
	J_{oo}(A/cm^2)	8.54×10^{6}	7.68×10^{6}	7.14×10^{6}	7.22×10^{6}
Cell 27A-4	ϕ_1(eV)	1.045	1.047	1.045	1.047
	ϕ(eV)	1.039	1.041	1.040	1.042
	J_{oo}(A/cm^2)	8.43×10^{6}	8.46×10^{6}	8.13×10^{6}	8.65×10^{6}
Cell 24B-2	ϕ_1(eV)	0.842	0.840	0.839	0.839
	ϕ(eV)	0.844	0.843	0.840	0.841
	J_{oo}(A/cm^2)	2.87×10^{4}	2.78×10^{4}	2.47×10^{4}	2.45×10^{4}
Cell 24B-4	ϕ_1(eV)	0.788	0.791	0.783	0.789
	ϕ(eV)	0.785	0.786	0.777	0.785
	J_{oo}(A/cm^2)	1.79×10^{4}	1.87×10^{4}	1.28×10^{4}	1.81×10^{4}

Figure 27 illustrates the plot of V_{oc} versus T for the cell shown in Figure 25. The barrier heights (denoted as ϕ_1) obtained from this method are also listed in Table 3. It can easily be seen that the values of the barrier height from these two methods are close to each other.

The experimental values of A and J_o, determined by these techniques, for $Cu_2S/Zn_{0.11}Cd_{0.89}S$ and $Cu_2S/Zn_{0.25}Cd_{0.75}S$ cells at different temperatures are listed in Table 2. The values of J_{oo} and ϕ under different levels of irradiance for these cells are shown separately in Tables 4 and 5.

The $\ln(J_{oo})$ versus ϕ data from these measurements fall roughly on a straight line for Cu_2S/CdS, $Cu_2S/Zn_{0.11}Cd_{0.89}S$ and $Cu_2S/Zn_{0.25}Cd_{0.75}S$ cells. Figure 28 shows $\ln(J_{oo})$ versus ϕ as a function of Zn content under AM1 illumination.

Current mechanisms for these junctions can be analyzed by considering several possible types of band diagrams that can exist. Several possible types of energy band diagrams for Cu_2S/CdS solar cells are shown in Figure 29. The electron affinity of CdS is larger than that of Cu_2S (Figure 29[a]). Therefore, the discontinuity in the conduction band edges of the Cu_2S and CdS is $\Delta x \approx 0.2$ eV. Assuming that carrier concentration density in Cu_2S is much larger than that of

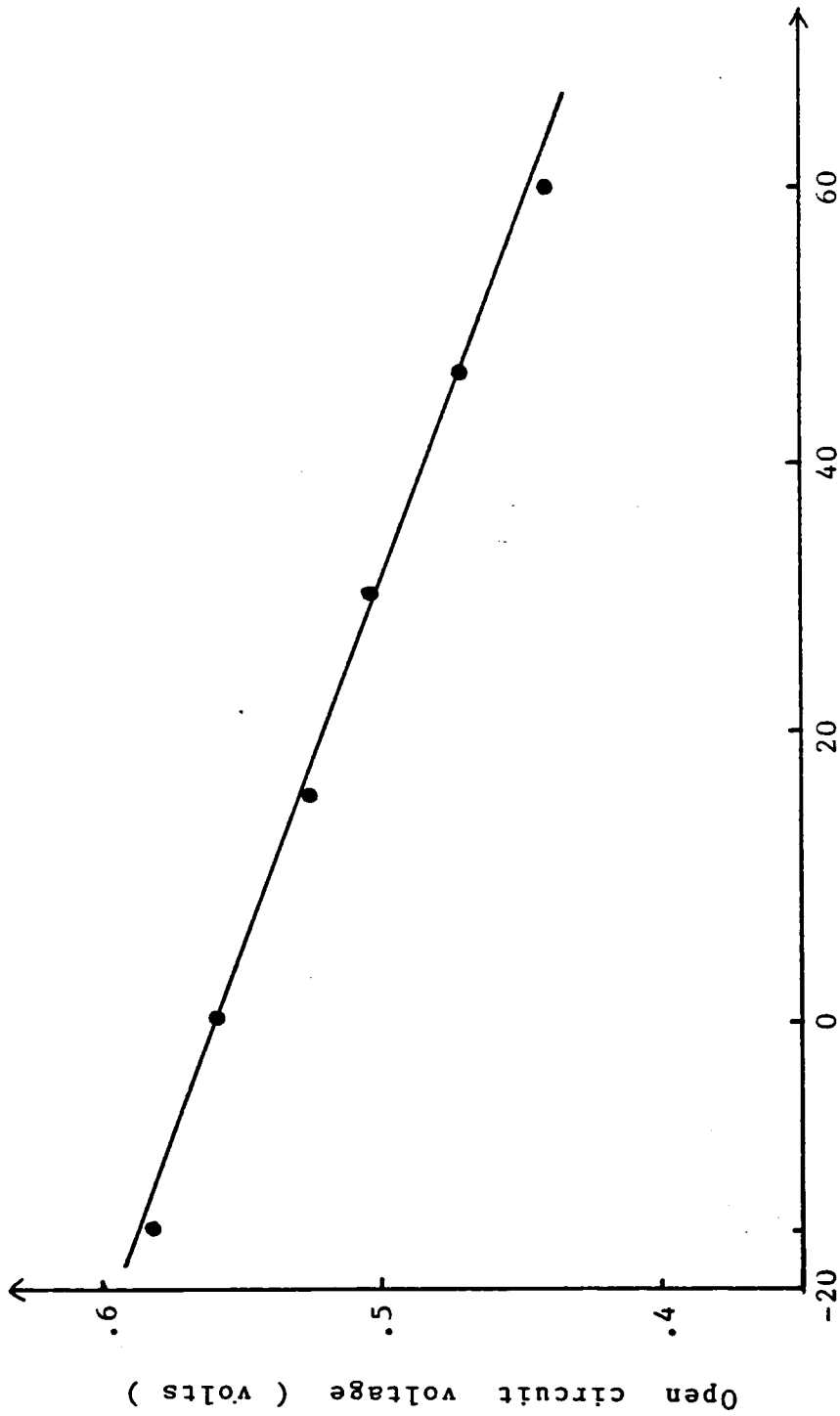

Figure 27: Plot of V_{oc} versus T for the cell shown in Figure 25.

TABLE 4

Values of J_{oo} and ϕ under various levels of irradiance for 4 different $Cu_2S/Zn_{0.11}Cd_{0.89}S$ solar cells. ϕ is the potential barrier height obtained from a plot of $\ln(J_o)$ versus $1/T$, and ϕ_1 is the potential barrier obtained from a V_{oc} versus T plot.

Sample		100% AM1	79% AM1	50% AM1	40% AM1
Cell 04D-1	ϕ_1(eV)	1.050	1.052	1.046	1.043
	ϕ(eV)	1.046	1.047	1.040	1.036
	J_{oo}(A/cm^2)	7.96×10^{5}	8.16×10^{5}	6.34×10^{5}	5.15×10^{5}
Cell 04D-2	ϕ_1(eV)	0.789	0.785	0.787	0.784
	ϕ(eV)	0.780	0.775	0.776	0.771
	J_{oo}(A/cm^2)	4.20×10^{3}	3.43×10^{3}	3.60×10^{3}	3.00×10^{3}
Cell 04D-3	ϕ_1(eV)	1.074	1.074	1.066	1.070
	ϕ(eV)	1.064	1.063	1.054	1.057
	J_{oo}(A/cm^2)	1.55×10^{6}	1.51×10^{6}	1.06×10^{6}	1.17×10^{6}
Cell 04D-4	ϕ_1(eV)	0.761	0.755	0.759	0.756
	ϕ(eV)	0.750	0.744	0.748	0.745
	J_{oo}(A/cm^2)	3.71×10^{3}	2.85×10^{3}	3.26×10^{3}	2.95×10^{3}

TABLE 5

Values of J_{oo} and ϕ under various levels of irradiance for 4 different $Cu_2S/Zn_{0.25}Cd_{0.75}S$ solar cells. ϕ is the potential barrier height obtained from a plot of $\ln(J_o)$ versus $1/T$, and ϕ_1 is the potential barrier obtained from a V_{oc} versus T plot.

Sample		100% AM1	79% AM1	50% AM1	40% AM1
Cell 10C-1	ϕ_1(eV)	0.832	0.829	0.829	0.834
	ϕ(eV)	0.814	0.809	0.808	0.810
	J_{oo}(A/cm^2)	1.71×10^{3}	1.36×10^{3}	1.41×10^{3}	1.47×10^{3}
Cell 10C-2	ϕ_1(eV)	0.653	0.651	0.658	0.659
	ϕ(eV)	0.633	0.631	0.634	0.633
	J_{oo}(A/cm^2)	1.02×10^{2}	0.87×10^{2}	1.01×10^{2}	0.98×10^{2}
Cell 10C-3	ϕ_1(eV)	0.746	0.747	0.742	0.737
	ϕ(eV)	0.727	0.710	0.721	0.716
	J_{oo}(A/cm^2)	3.99×10^{2}	1.86×10^{2}	3.16×10^{2}	2.50×10^{2}
Cell 10C-4	ϕ_1(eV)	0.761	0.762	0.756	0.762
	ϕ(eV)	0.750	0.744	0.743	0.748
	J_{oo}(A/cm^2)	9.66×10^{2}	6.12×10^{2}	6.96×10^{2}	8.17×10^{2}

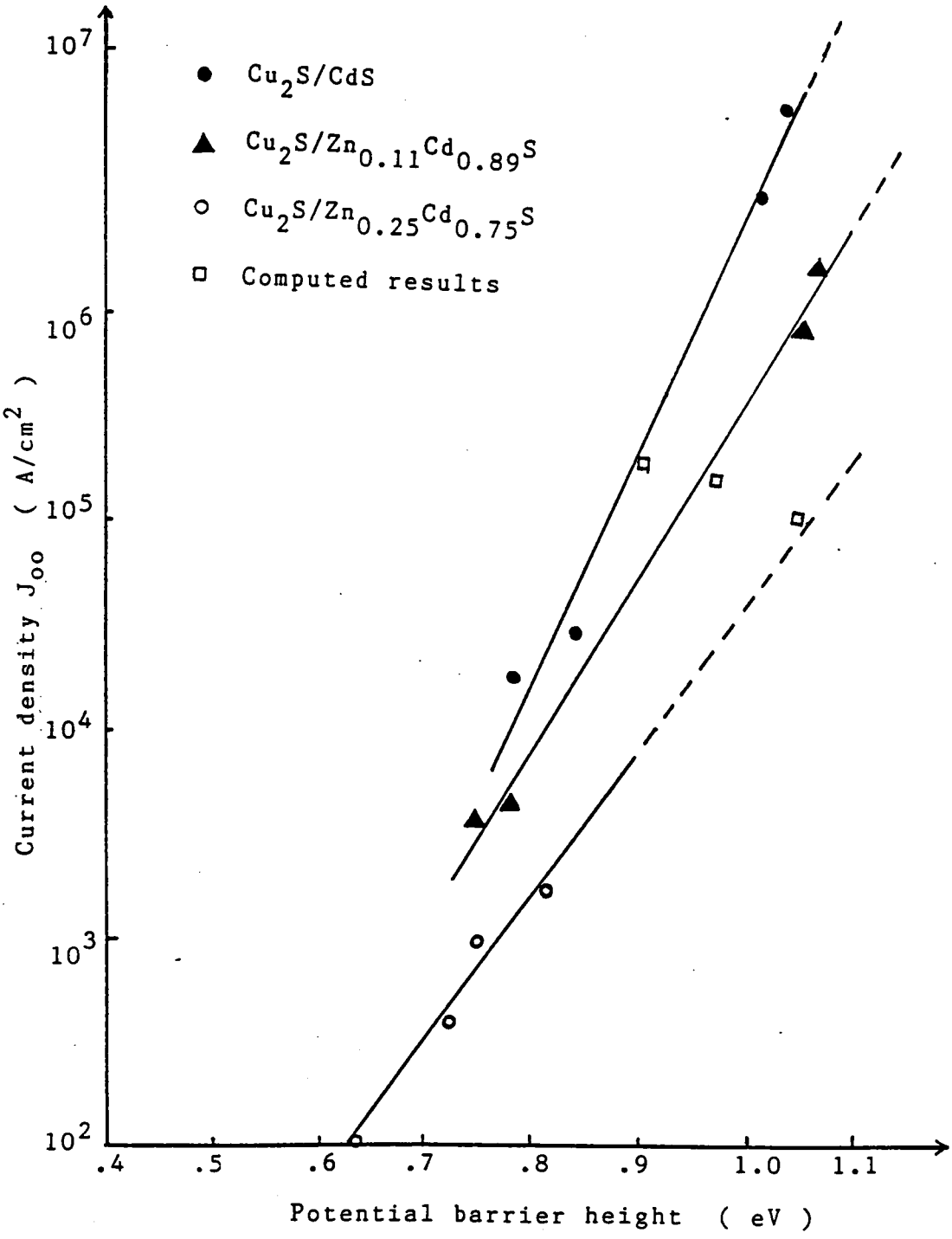

Figure 28: $Ln(J_{oo})$ vs. ϕ as a function of Zn content under AM1 illumination.

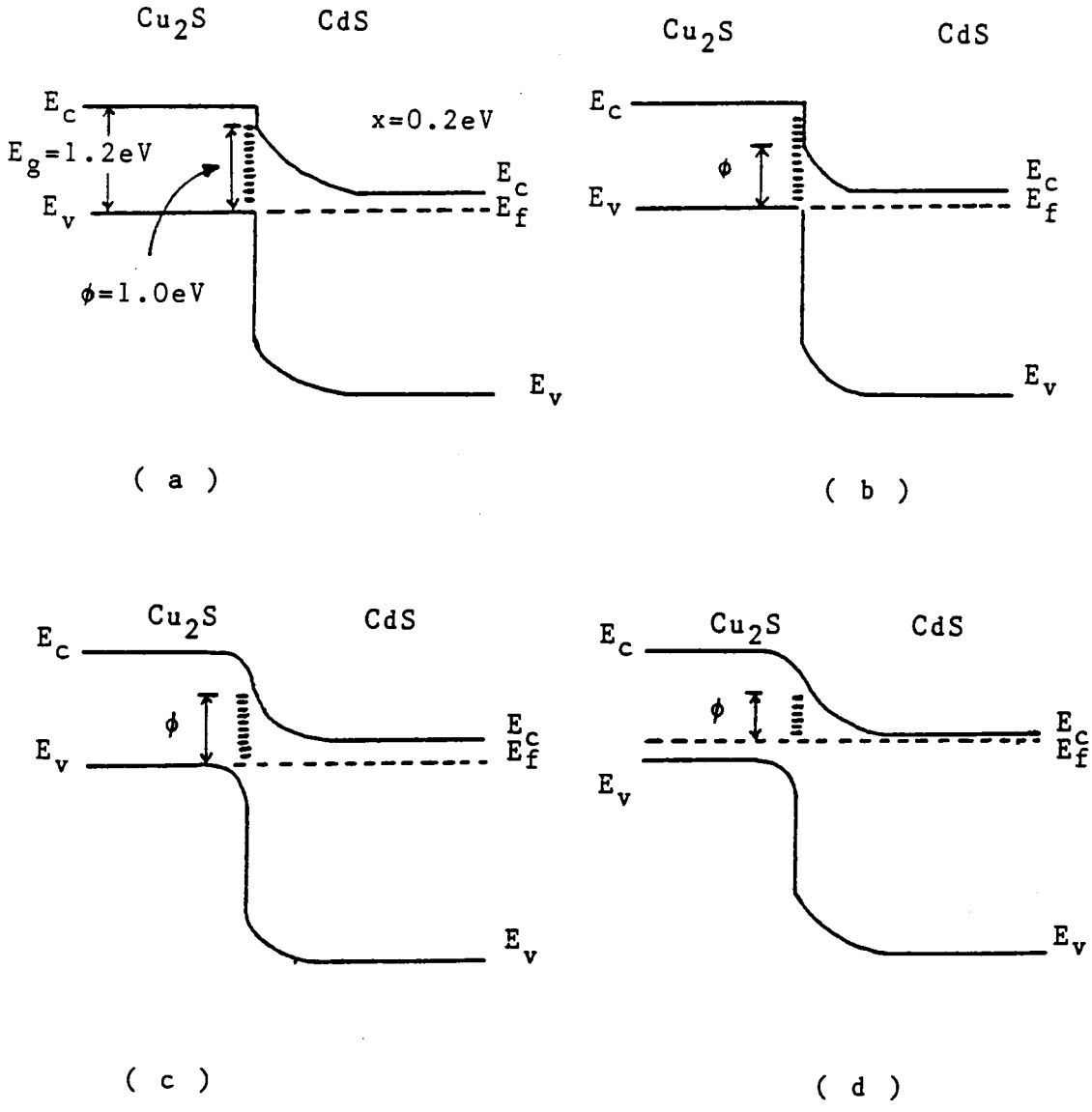

Figure 29: Energy band diagrams for Cu_2S/CdS cells under various conditions. ϕ represents the barrier height. These cases are described in the text.

CdS, then the Cu_2S band bending can be neglected, and the Fermi level in the Cu_2S is close to the valence band. The highest value of the potential barrier ϕ for Cu_2S/CdS cells should be Eg (Cu_2S) - $\Delta x \approx 1.0$ eV as shown in Figure 29(a). The reduced value of ϕ can be attributed to several things:

1) Tunneling of electrons through the narrow upper region of the barrier as shown in Figure 29(b).

2) Band bending of Cu_2S due to the lower carrier concentration, as shown in Figure 29(c).

3) Fermi level lies in the bandgap rather than in the valence band as shown in Figure 29(d).

The current density J_{oo} can be expressed as follows:

$$J_{oo} = qN_cS_I \qquad (4\text{-}3)$$

where N_c is the density of electrons at the interface in CdS and S_I is the interface recombination velocity. S_I is given by the relation $S_I = v_{th}\sigma N_I$ where v_{th} is the thermal velocity of electrons, σ the capture cross section of interface states, and N_I the density of interface states. The lattice constant and electron affinities for Cu_2S, CdS, and ZnS are listed in Table 6. If we assume that they both

follow Vegard's law, the lattice constants and the electron affinities for $Zn_{0.11}Cd_{0.89}S$ and $Zn_{0.25}Cd_{0.75}S$ can be calculated. Therefore N_I, S_I, and J_{oo} can also be estimated. It is obvious that a better lattice match can reduce the interface state density which therefore reduces the current density J_{oo}. The decrease in the electron affinity mismatch between Cu_2S and $Zn_xCd_{1-x}S$ will reduce the height of the conduction band step, thus increasing the potential barrier height ϕ. The highest measured value of ϕ for the $Cu_2S/Zn_{0.11}Cd_{0.89}S$ cell is higher than that for a Cu_2S/CdS cell. This result is as expected. The highest value of ϕ for $Cu_2S/Zn_{0.25}Cd_{0.75}S$ cells, however, is lower than that for a Cu_2S/CdS cell. This reduction of ϕ can be attributed to those reasons mentioned above. Taking $v_{th} = 10^7$ cm/sec, $\sigma = 10^{-15}$ cm^2, the theoretical values of J_{oo} and ϕ for Cu_2S/CdS, $Cu_2S/Zn_{0.11}Cd_{0.89}S$ and $Cu_2S/Zn_{0.25}Cd_{0.75}S$ cells were computed and are listed in Table 6. These data fall close to the experimental lines in Figure 28.

If we compare the plot of $\ln(J_{oo})$ versus ϕ for Cu_2S/CdS cells with those of $Cu_2S/Zn_xCd_{1-x}S$ cells, the line on the $\ln(J_{oo})$ vs. ϕ shifts to the right as the content of Zn in $Zn_xCd_{1-x}S$ increases. The reason for this is simply the reduction in electron affinity mismatch. The question as to why the values of J_{oo} and ϕ fall on the straight line is

TABLE 6

Lattice constant and electron affinities for Cu_2S, CdS, and ZnS, and resulting values of N_I, S_I, J_{oo} and ϕ.

Sample	Lattice constant (A^o)	Electron affinity (eV)	N_i (cm^{-3})	S_i (cm/sec)	J_{oo} (A/cm^2)	ϕ (eV)
Cu_2S	3.96	4.30				
CdS	4.135	4.50	5.284×10^{13}	5.284×10^{6}	1.86×10^{6}	1.0
ZnS	3.814	3.90				
$Zn_{0.11}Cd_{0.89}S$	4.10	4.43	4.281×10^{13}	4.281×10^{6}	1.51×10^{6}	1.07
$Zn_{0.25}Cd_{0.75}S$	4.055	4.35	2.953×10^{13}	2.953×10^{6}	1.04×10^{6}	1.15

more difficult to answer. Meakin et al. suggest that N_I varies as $N_I(0)\exp(\phi/K)$ as ϕ changes [73], where K is a constant. Therefore , the relation between ln J_{oo} and ϕ becomes linear. The dependence of J_{oo} on the diffusion voltage has been derived by Boer [74]. However the physical explanation for this relation is not well understood.

C) V_{oc} Decay

The open circuit voltage (V_{oc}) is one of the most important parameters in solar cells. Higher V_{oc} lead to higher cell efficiency. Unfortunately, V_{oc} (hence the efficiency) decays with time for the Cu_2S/ZnCdS cells. Figure 30 shows a plot of the open circuit voltage (V_{oc}) versus time for Cu_2S/CdS and $Cu_2S/Zn_xCd_{1-x}S$ cells. It is seen that V_{oc} is fairly stable for the Cu_2S/CdS cell. However, V_{oc} decreases up to 20% after 2 hours of exposure under AM1 illumination for the $Cu_2S/Zn_xCd_{1-x}S$ cell. Several studies on the V_{oc} decay were conducted in the past [75,76]. Three mechanisms have been proposed to explain the V_{oc} decay: 1) The enhanced electric field at the ends of Cu_2S intrusions with sharp tips causes localized heating at these tips as shown in Figure 31. The increase in temperature at these tips results in an increase in diode current and hence a decrease in V_{oc}. 2) The heating at the tips of intrusions has an effect on the concentration of copper vacancies in

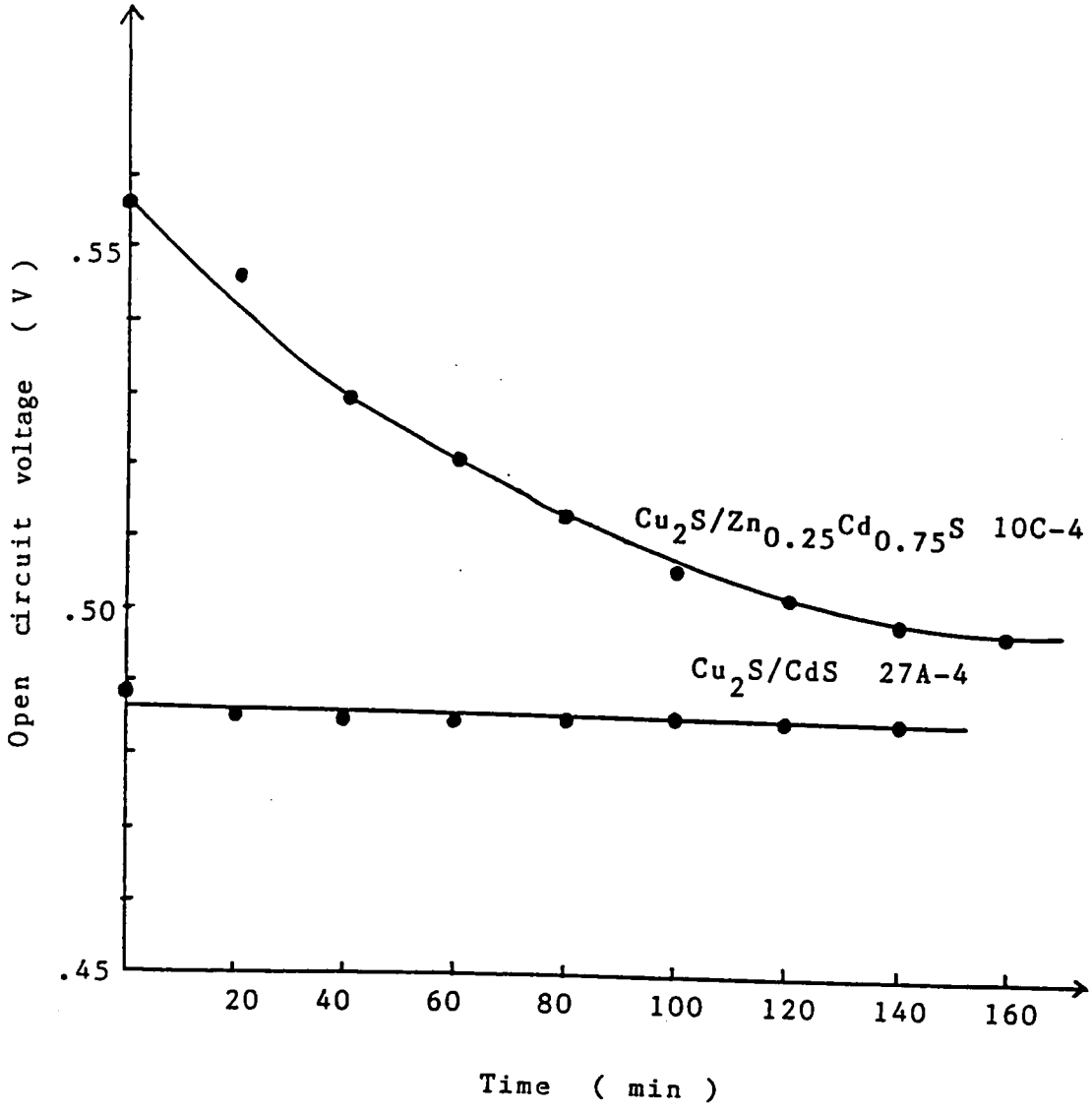

Figure 30: Plot of the open circuit voltage versus time for Cu_2S/CdS and $Cu_2S/Zn_{0.25}Cd_{0.75}S$ cell. The decay is significant and deleterious for the $Zn_xCd_{1-x}S$ cells.

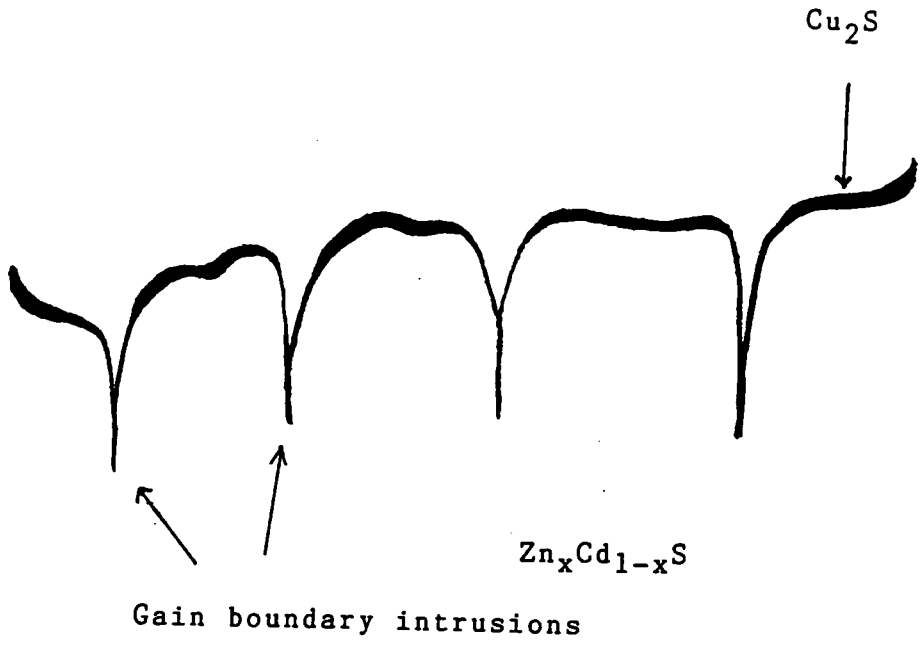

Figure 31: Cross section of a $Cu_2S/Zn_xCd_{1-x}S$ junction with sharp tips at the ends of intrusions.

Cu_2S. The increase in temperature results in the generation of copper vacancies so that copper is driven out of Cu_2S. This copper migration can also cause an increase in diode current and lead to a decay in V_{oc}. 3) V_{oc} decay may be related to extensive growth of copper at the tips of intrusion. The copper whiskers can result in a shunting of Cu_2S to the back contact of the cell which can cause a decay in V_{oc}.

V_{oc} decay can also be attributed to a deep hole trapping effect (electron relaxation from the deep trap level in i-layer). Figure 32 shows the energy band diagram for a $Cu_2S/Zn_xCd_{1-x}S$ cell. Electrons may relax to the valance band of ZnCdS, which increases the positive charge in the depletion region and reduces its thickness. The reduction of depletion width results in an increase of the interface recombination current. Therefore, V_{oc} decreases.

Time dependence of capacitance was also measured for both types of cells to see if there is any correlation with V_{oc} decay. These results are given in Figure 33. It is seen that C is fairly constant for the Cu_2S/CdS cell, and C increases with time for the $Cu_2S/Zn_xCd_{1-x}S$ cell. Electron relaxation in i-layer can also account for the C versus time behavior. Thus, the electron relaxation in the space charge region seems the most likely cause for the V_{oc} decay, since

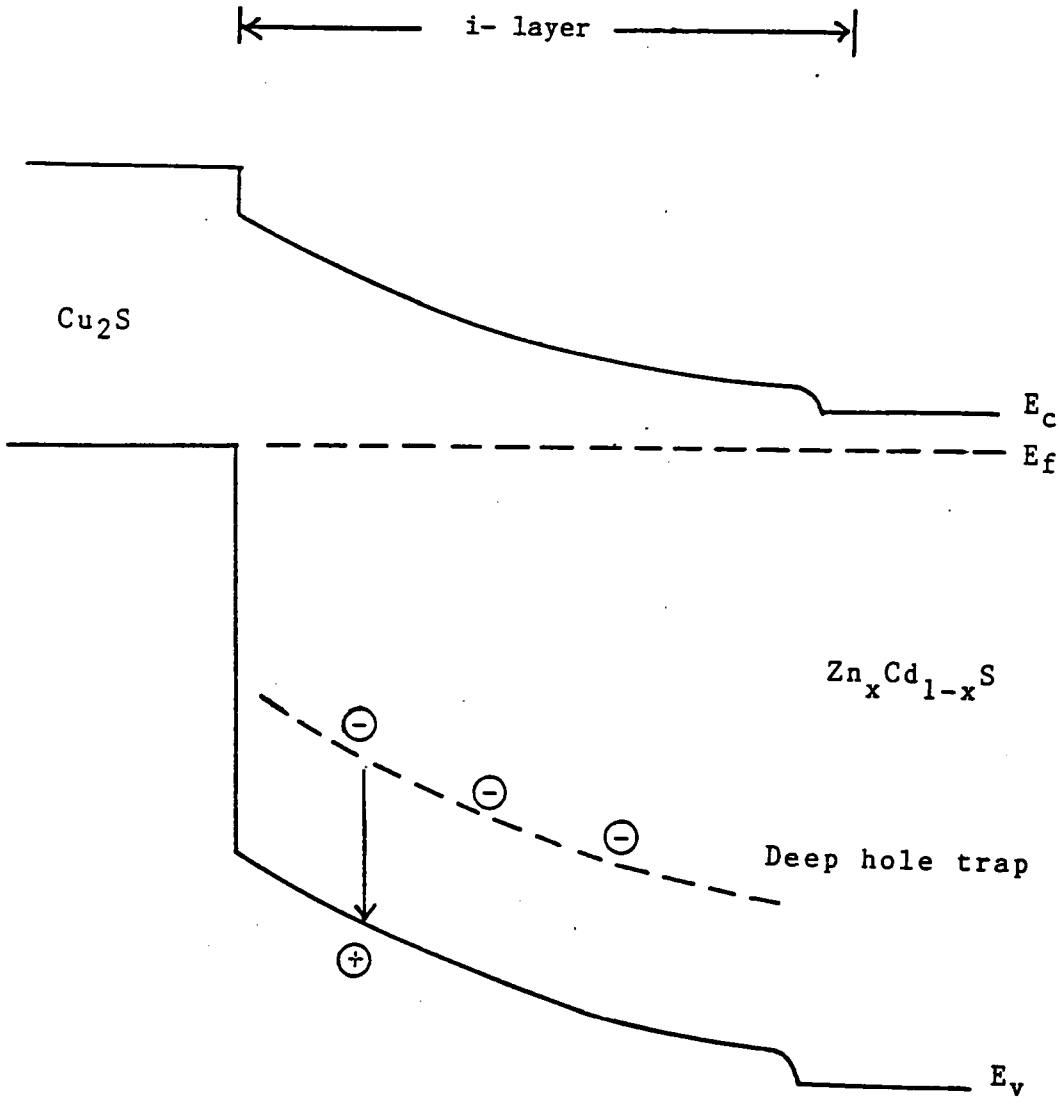

Figure 32: Energy band diagram for a $Cu_2S/Zn_xCd_{1-x}S$ cell, showing recombination at deep hole trap.

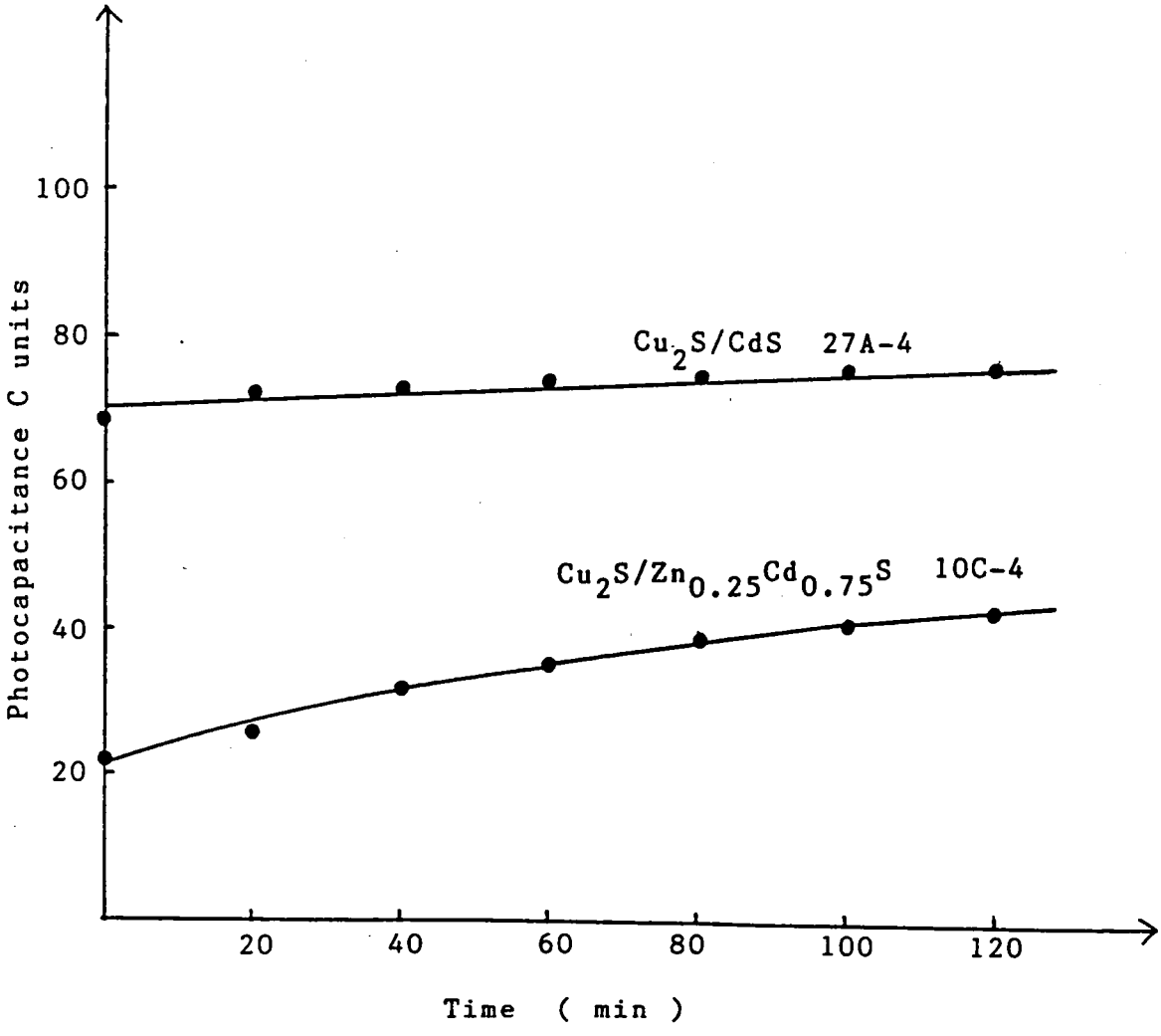

Figure 33: Time dependence of capacitance for Cu_2S/CdS and $Cu_2S/Zn_{0.25}Cd_{0.75}S$ cells.

it is also consistent with the capacitance increase, caused by the shrinking space charge width.

4.2 SPECTRAL MEASUREMENTS

One-beam and two-beam techniques were used for spectral measurements. Figure 34 shows the spectral response (quantum efficiency) of a typical Cu_2S/CdS solar cell. Two curves are seen in this figure. The line on the top shows the quantum efficiency* as a function of wavelength without light bias (one-beam technique). The line at the bottom indicates the quantum efficiency as a function of wavelength with white light bias of 100 mW/cm^2 (two-beam technique). Both curves fall off near the wavelength of 1000 nm. Peaks are observed at 505 nm and 650 nm on both curves. Similar results were obtained for $Cu_2S/Zn_xCd_{1-x}S$ cells. Figure 35 gives spectral response curves for a $Cu_2S/Zn_{0.25}Cd_{0.75}S$ cell with and without white light bias. Two peaks are seen on these curves: One peak occurs at wavelegth of 460 nm; the other peak is much broader and is not as obvious. The spectral response with white light bias is higher than that without light bias for both types of cells. Reasons for this are discussed below.

The peak at 505 nm in Figure 34 corresponds to the bandgap of the CdS (= 2.45 eV). The broad peak at about 650

* Quantum efficiency is defined as the number of electrons contributing to the short circuit current per incident photon.

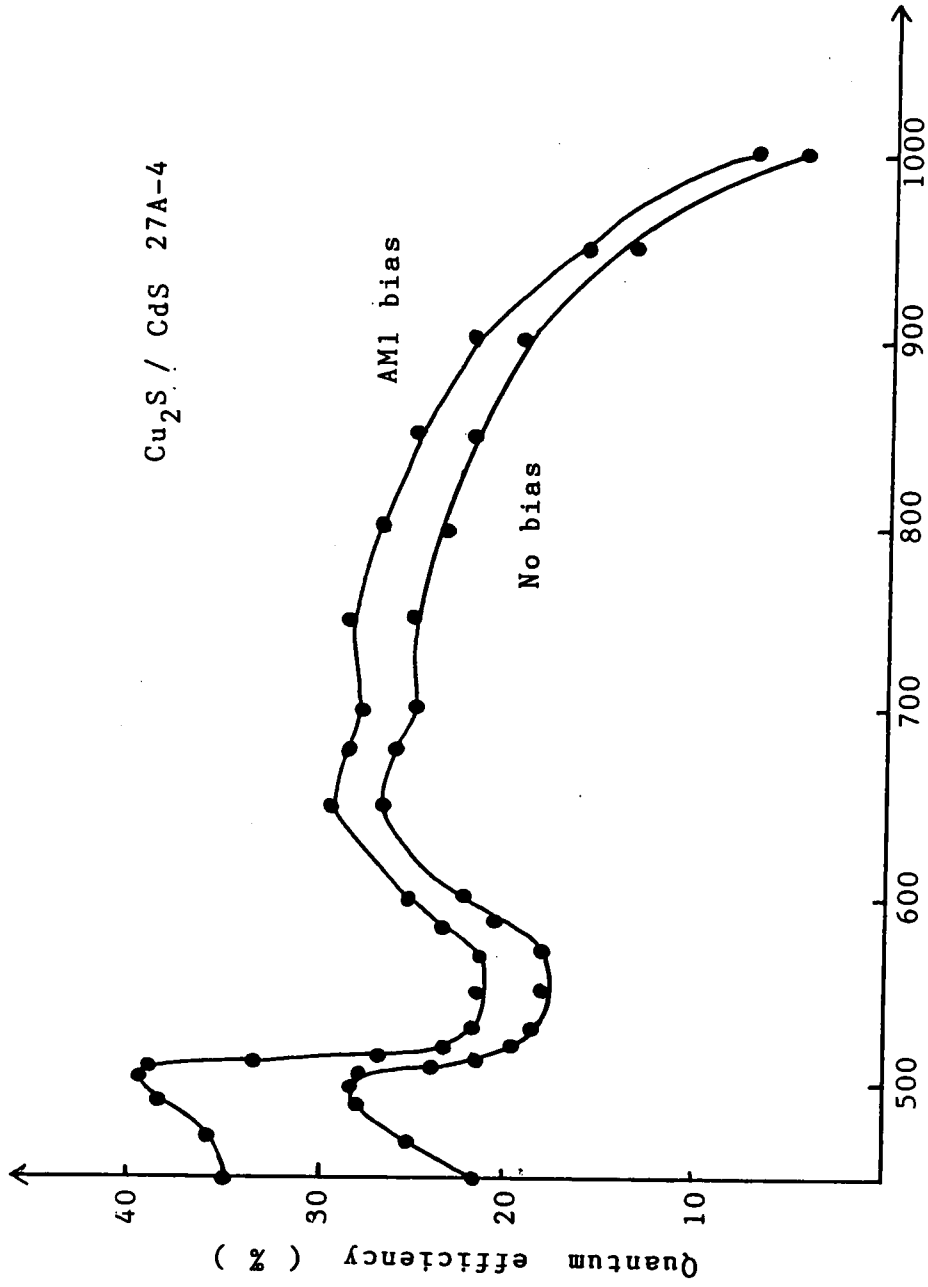

Figure 34: Spectral response of a typical Cu_2S/CdS solar cell with and without white light bias.

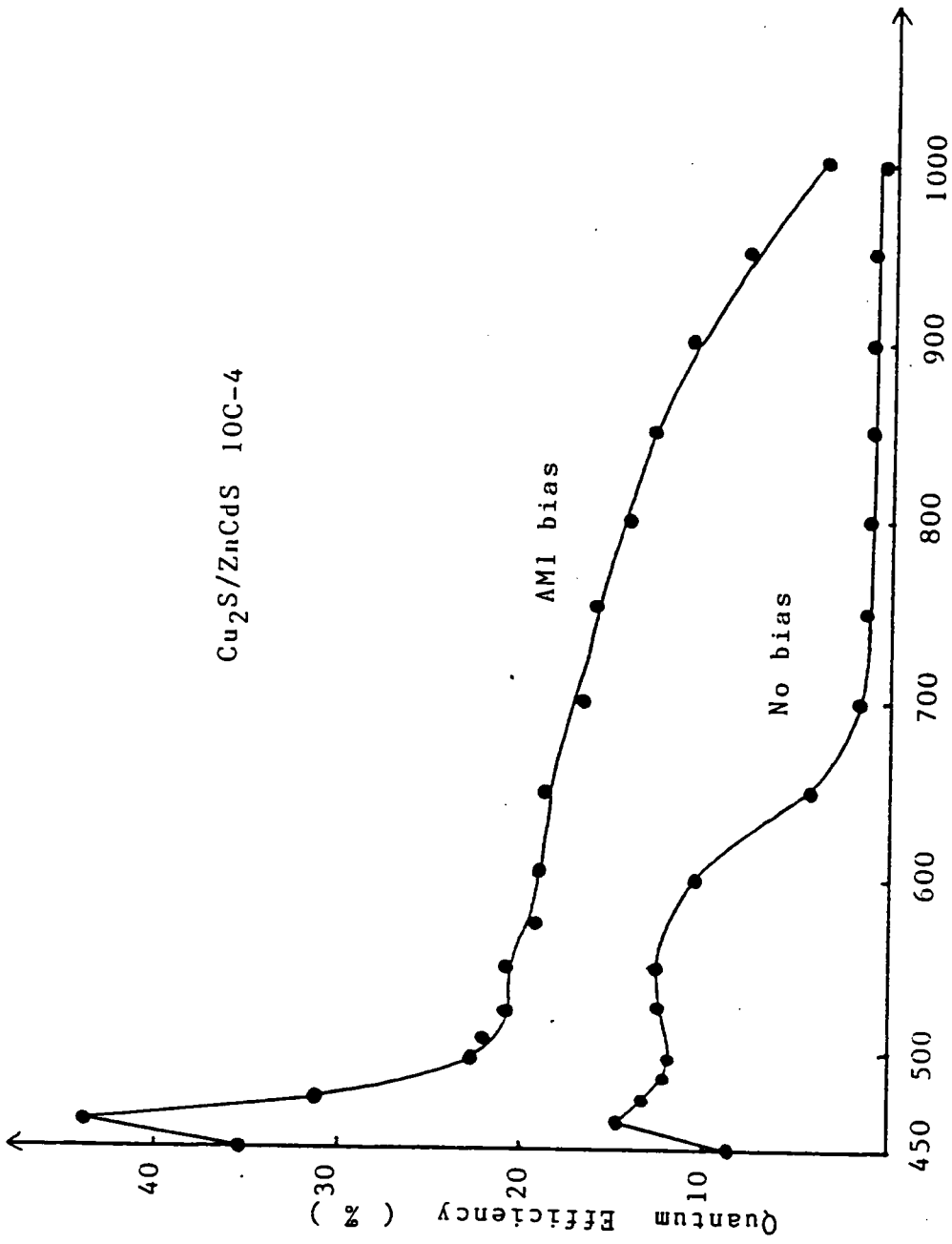

Figure 35: Spectral response of a $Cu_2S/Zn_{0.25}Cd_{0.75}S$ solar cell with and without white light bias.

nm is attributed to the ionization of the deep donor energy level in the CdS. This deep donor trap is centered at roughly 1.91 eV below the conduction band of the CdS. The reason for the broad peak is that the deep donor traps are not discrete. The peak at 460 nm in Figure 35 corresponds to the bandgap of the $Zn_{0.25}Cd_{0.75}S$ (= 2.70 eV). The location of the second peak is not as obvious, therefore, it is difficult to determine the deep donor trap energy by this technique. However, this deep donor level can be seen by photocapacitance measurements which will be discussed in a later section. The small response at wavelengths higher than 1000 nm is due to the reduced Cu_2S absorption coefficient.

A white light bias enhances the spectral response for both types of cells. This enhancement results from the ionization of the deep traps. Figure 12 illustrates the energy band diagram showing the enhancement effect. Electrons are excited from the deep traps and raised to the conduction band of CdS or $Zn_xCd_{1-x}S$. These electrons are then swept into the bulk of CdS or $Zn_xCd_{1-x}S$, or recombine with the holes in the valence band. The ionized holes increase the positive charge in the depletion region and reduce its width. The reduction of depletion width results in an increase of the electric field in this region. Therefore, the spectral response enhances (See equation 2-8.).

The effect of a blue and red light bias on the spectral response for both cell types was also investigated. Figures 36 and 37 give the results of spectral response with a blue and red light bias for Cu_2S/CdS and $Cu_2S/Zn_{0.25}Cd_{0.75}S$ cells respectively. Peaks occur at 505 nm and 650 nm for Cu_2S/CdS cell and one peak at 460 nm for the $Cu_2S/Zn_{0.25}Cd_{0.75}S$ cell. These results are similar to those seen in Figures 34 and 35. It can also be seen that a blue light bias enhances the spectral response for both types of cells, while red light bias quenches the response. Similar results were also obtained by other researchers [77,78,79]. The reason for the enhancement of the spectral response due to a blue bias is the same as that due to white light bias (that is, it is due to the ionization of deep traps). The quenching of the spectral response can be attributed to trapping at the deep energy level. (Figure 12 illustrates the energy band diagram for the junction showing the quenching effect.) Electrons are excited from the valance band and then trapped in this deep energy level. The resulting holes in the valence band can be swept into the Cu_2S by the electric field or recombined with the electrons falling from the conduction band. The trapping of electrons in this deep energy level decreases the positive charge and hence increases the depletion width. The increase of the depletion width can

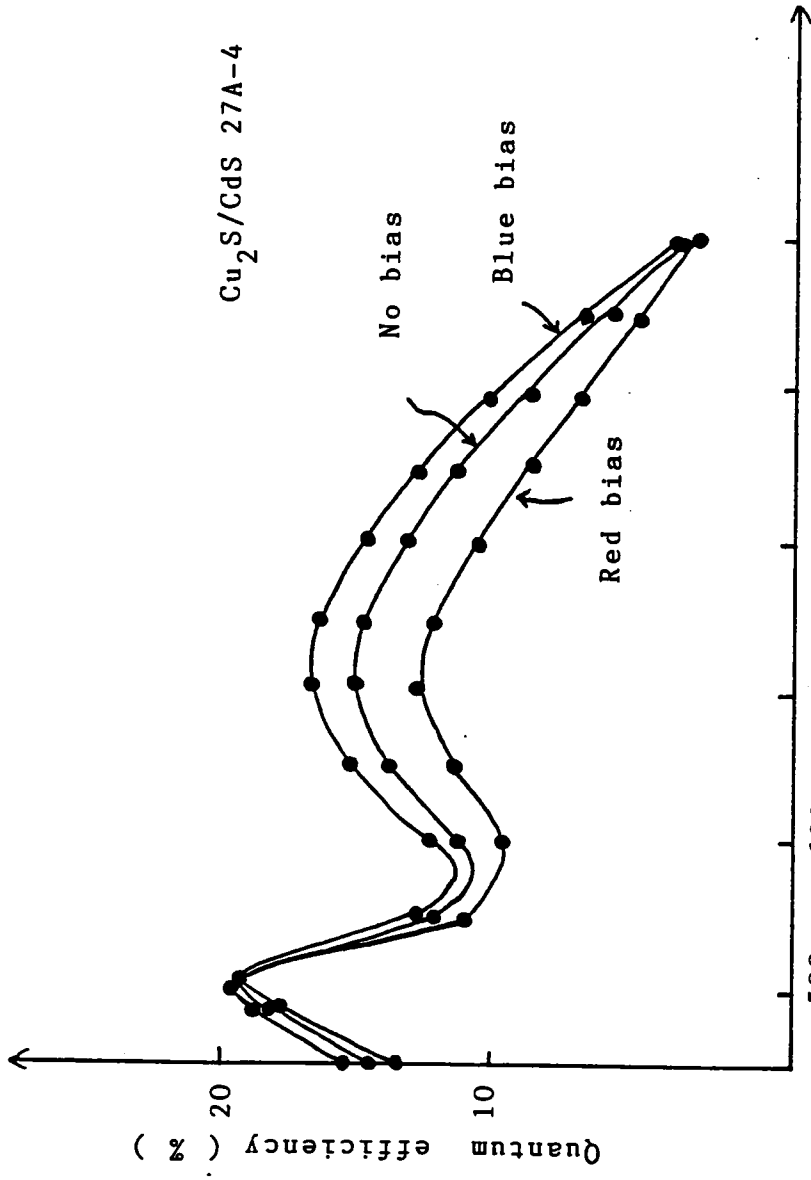

Figure 36: Quantum efficiency versus wavelength with a blue and red bias for a Cu_2S/CdS cell.

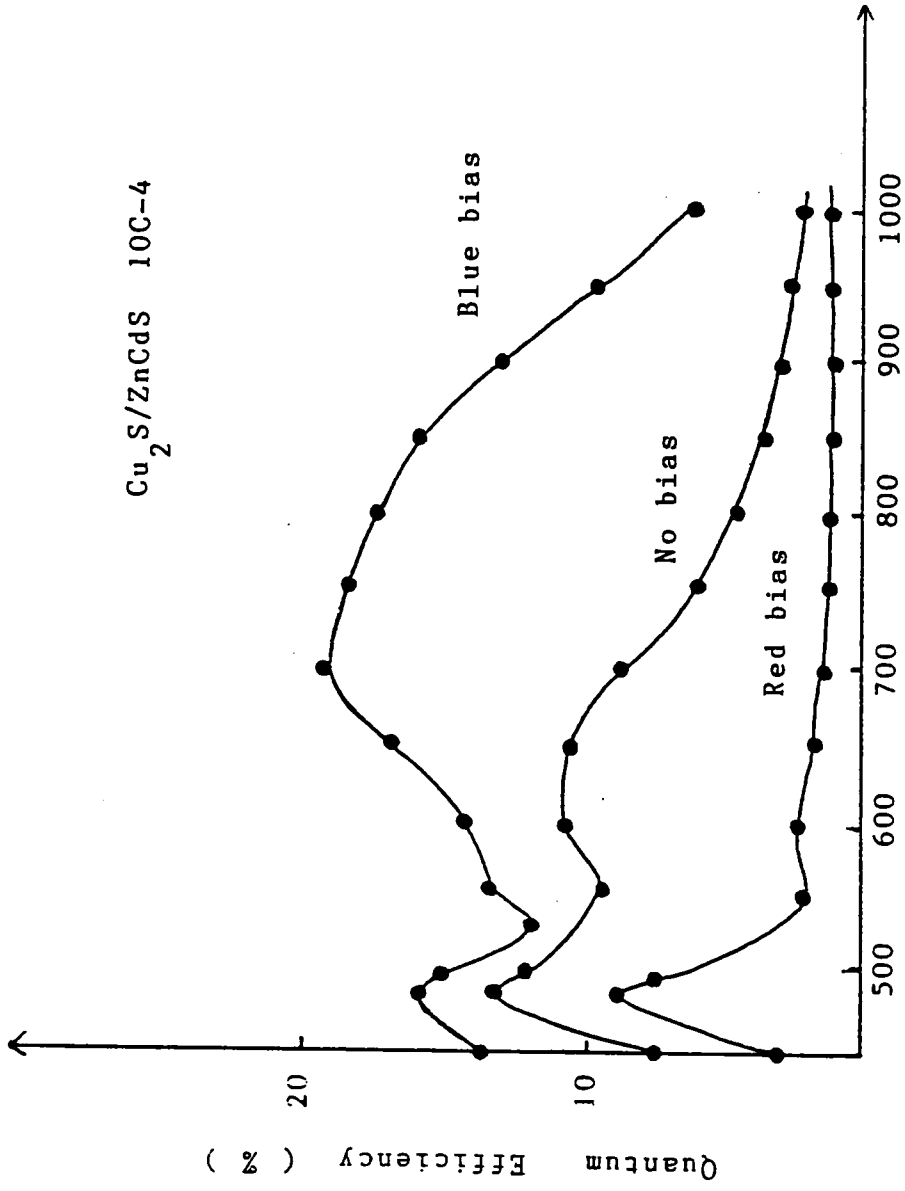

Figure 37: Quantum efficiency versus wavelength with a blue and red bias for a $Cu_2S/Zn_{0.25}Cd_{0.75}S$ cell.

result in a reduction of the electric field; therefore spectral response decreases..

The effect of bias light on the energy band diagram for Cu_2S/CdS or $Cu_2S/Zn_xCd_{1-x}S$ cells is shown in Figure 38. Red bias light quenches and blue bias light enhances the photocurrent of the $Cu_2S/Zn_xCd_{1-x}S$ cell more than that of the Cu_2S/CdS cell. This could be partly because the density of the deep energy levels in the $Zn_xCd_{1-X}S$ is higher than that in the CdS. Another possibility for the larger effect on the $Cu_2S/Zn_xCd_{1-x}S$ could be due to a larger capture cross section of deep traps in the $Zn_xCd_{1-x}S$. This phenomena could be in part responsible for the lower short circuit currents that are general seen for ZnCdS based cells.

4.3 CAPACITANCE MEASUREMENTS

Measurements of $1/C^2$ versus voltage bias for a p-n junction can be used to determined the diffusion voltage and carrier concentration. These curves are frequency-independent for a junction without deep traps. However, this is not the case for heat-treated Cu_2S/CdS and $Cu_2S/ZnCdS$ cells. The results for heat-treated cells show frequency-dependent behavior, which indicates the existence of deep traps in these junctions. A plot of $1/C^2$ versus bias voltage measured at different frequencies for a

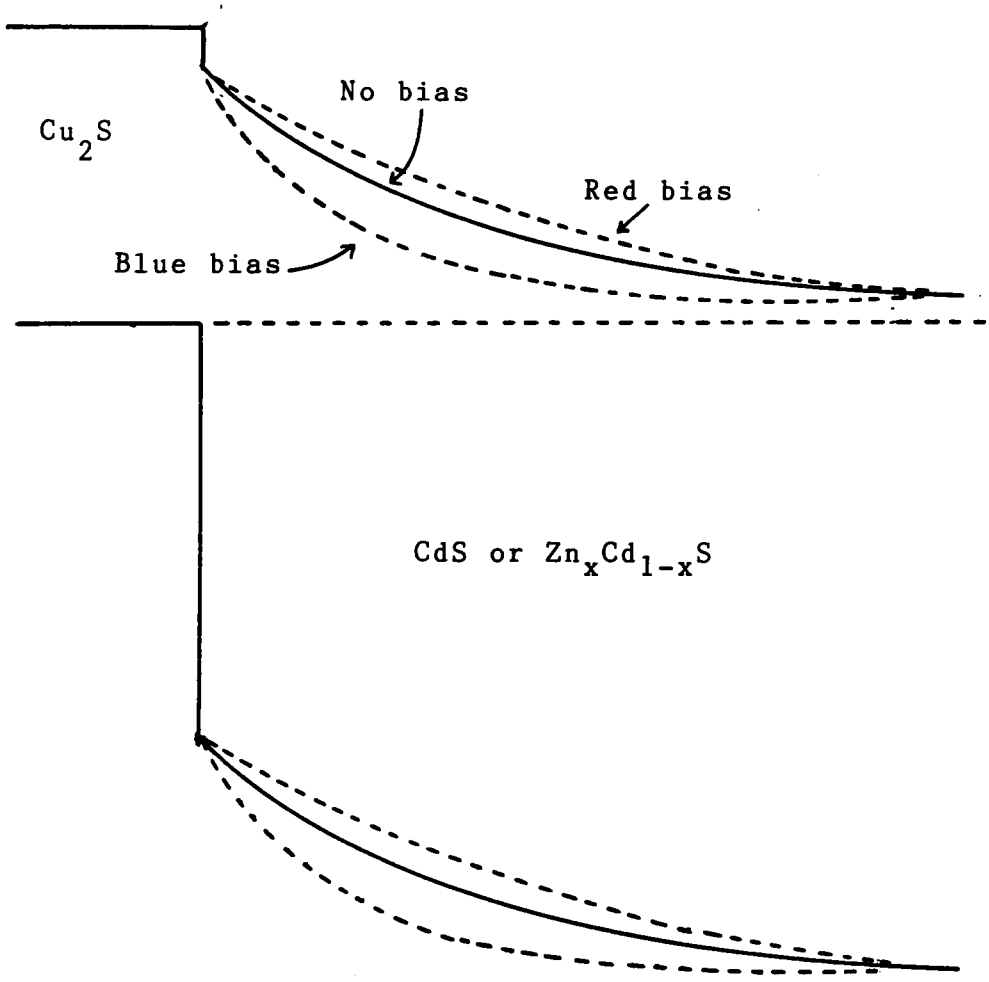

Figure 38: Effect of bias light on the energy band diagram for Cu_2S/CdS or $Cu_2S/Zn_xCd_{1-x}S$ cells.

Cu_2S/CdS junction is shown in Figure 39. Notice that these curves are fairly flat, verifying that a high resistance copper compensated layer (i-layer) exists near the interface, which clamps the depletion width in the dark. The slope of the straight line increases with increasing frequency for a Cu_2S/CdS junction. At high frequencies, C becomes smaller because slow traps cannot respond to the signal frequency. The slope of the straight line gives a value of the density, which is close to the shallow donor denity, N_D. (See equation 2-25). At low frequencies, all the traps respond to the signal frequency. C becomes larger and the carrier density is $N_D + N_t$. The stronger dispersion of these curves for the Cu_2S/CdS junction is probably due to the larger range of trap lifetimes.

$1/C^2$ versus voltage curves for a $Cu_2S/Zn_{0.25}Cd_{0.75}S$ junction are shown in Figure 40. These curves are even flatter than those of a Cu_2S/CdS junction. This is because the depletion width of the $Cu_2S/Zn_{0.25}Cd_{0.75}S$ junction is larger than that of CdS junction. The effect of voltage bias on the depletion width of the $Cu_2S/Zn_{0.25}Cd_{0.75}S$ junction gives a smaller capacitive response than that of the Cu_2S/CdS junction. The wider depletion width might be due to longer heat treatment of the junction. The weaker dispersion of $1/C^2$ versus voltage is probably due to a smaller range of trap lifetimes.

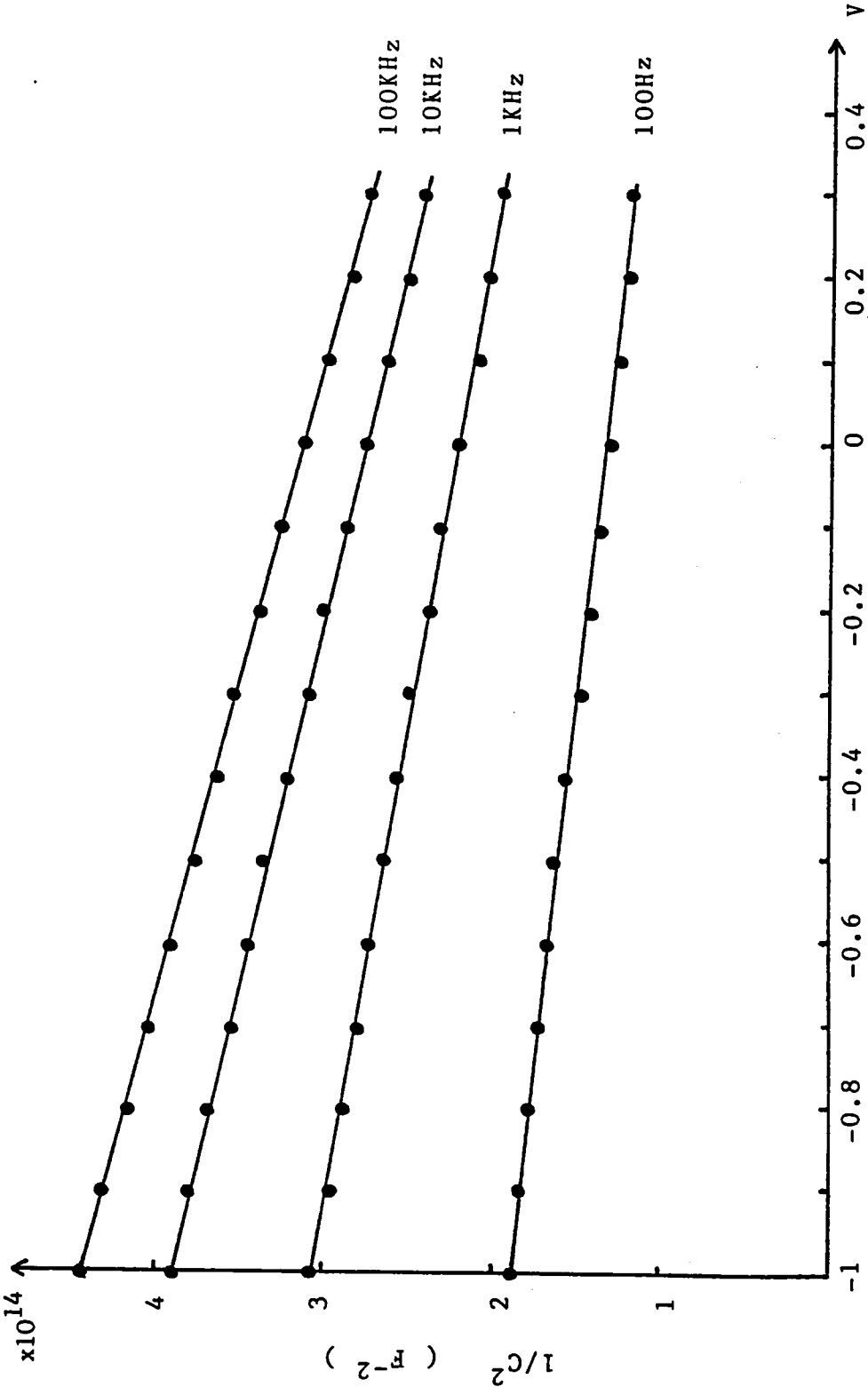

Figure 39: $1/C^2$ versus bias voltage curves measured at different frequencies for a Cu_2S/CdS junction.

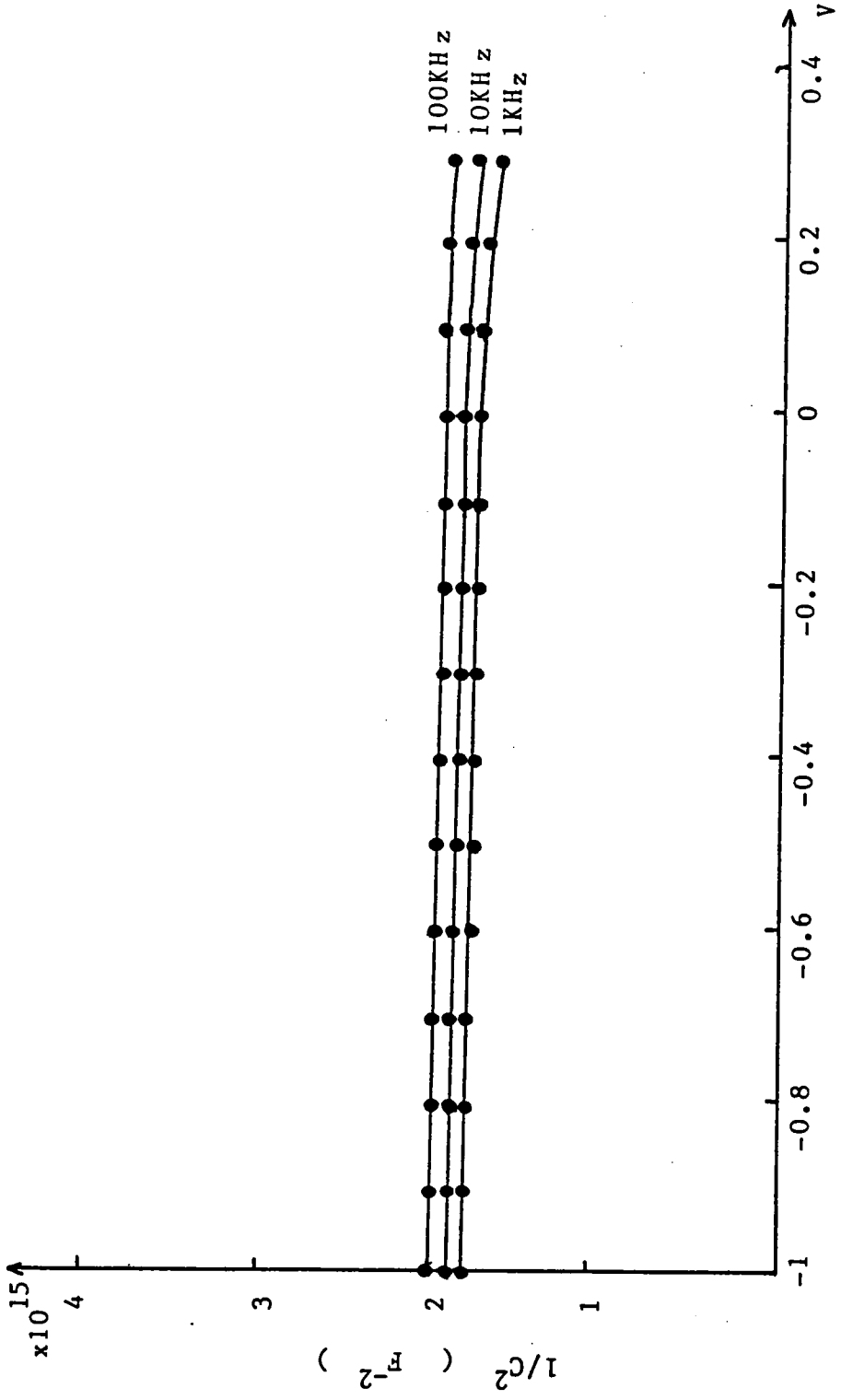

Figure 40: $1/C^2$ versus voltage curves measured at different frequencies for a $Cu_2S/Zn_{0.25}Cd_{0.75}S$ junction.

Plots of $1/C^2$ versus voltage bias, with temperature as a variable, for Cu_2S/CdS and $Cu_2S/Zn_{0.25}Cd_{0.75}S$ junctions are shown in Figures 41 and 42 respectively. These curves are also flat which again verifies the existence of an i-layer near the junction. The response time of a deep trap depends on the temperature. At low temperatures the response time increases. C decreases because slow traps can not follow the signal frequency. However, at high temperatures the response time decreases. More traps can respond to the signal, thus C increases. The same explanation that accouted for the larger dispersion of the $1/C^2$ versus voltage at different frequencies also explains why the Cu_2S/CdS junction is more temperature sensitive than the $Cu_2S/Zn_xCd_{1-x}S$ junction.

The results obtained from these measurement indicate that a high resistance i-layer exists at the interface of the junctions. The i-layer results from post-heat treatment of the cells. (This process is necessary for cell fabrication.) Without heat-treatment these cells show a poor junction between Cu_2S and the CdS or ZnCdS layer, with large leakage current resulting across the junction. Heat-treatment results in Cu diffusion from Cu_2S into the CdS (or ZnCdS) layer. The Cu atoms in the CdS (or ZnCdS) form acceptor states which compensate the donor states in CdS (or ZnCdS),

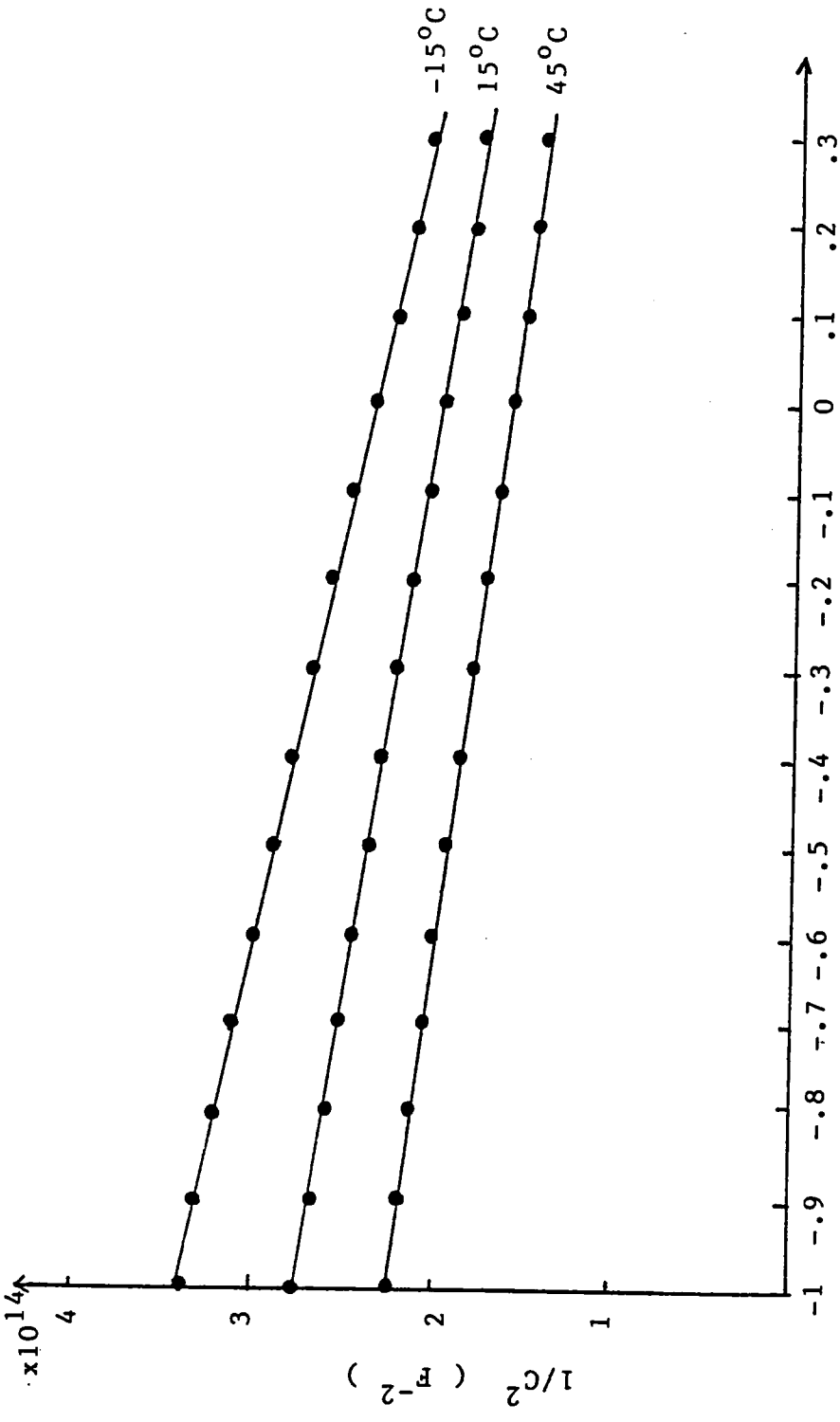

Figure 41: $1/C^2$ versus voltage curves measured at different temperatures for a Cu_2S/CdS junction.

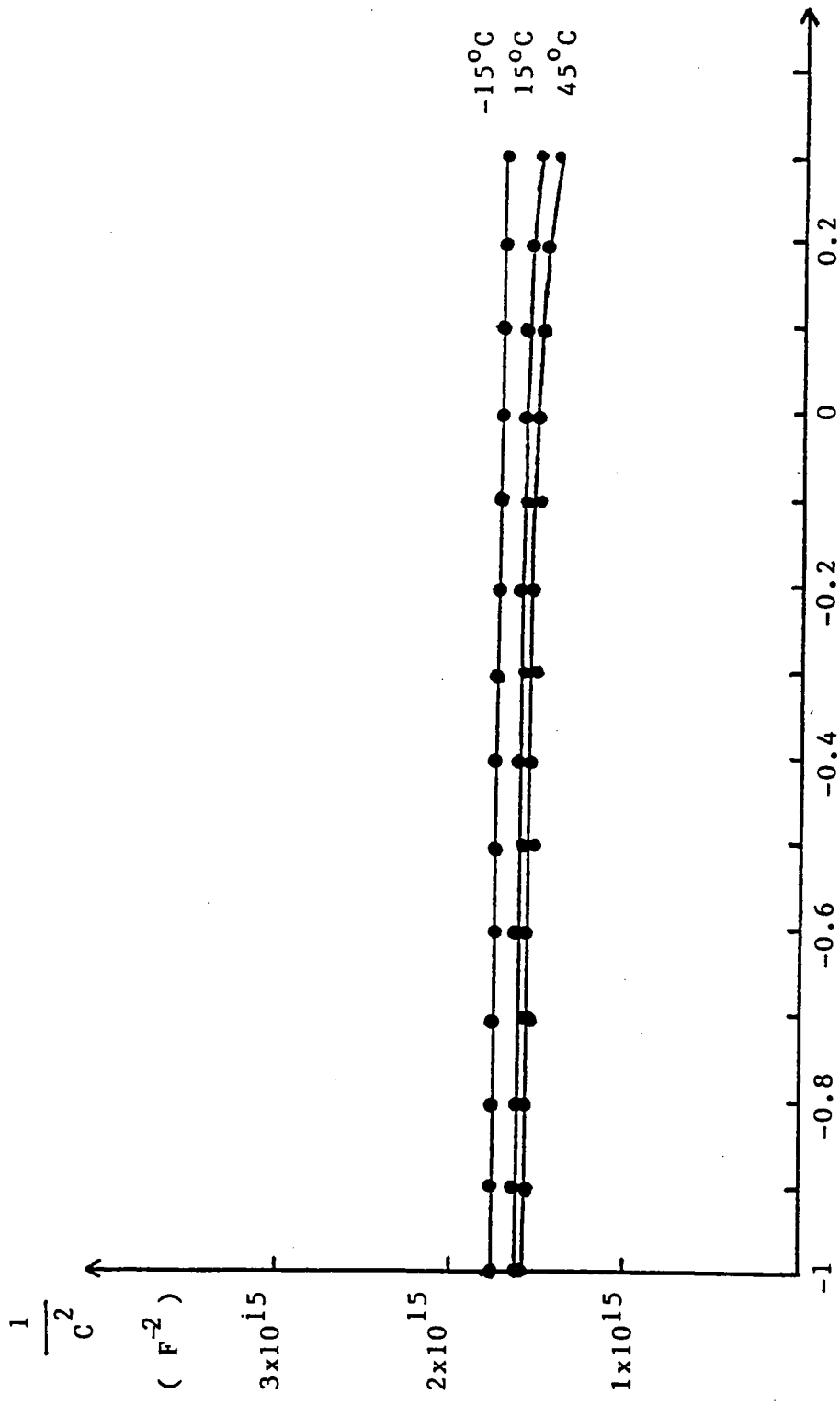

Figure 42: $1/C^2$ versus voltage curves measured at different temperatures for a $Cu_2S/Zn_{0.25}Cd_{0.75}S$ junction.

resulting in an intrinsic layer (i-layer). The space-charge-limited current technique can be applied to determine the deep trap energy and the trap density in this i-layer. This is discussed later.

Measurement of the diffusion capacitance as a function of forward current can yield the minority carrier (electron) lifetime. One possible mechanism [80] is that the electron lifetime at the interface is inversely proportional to the density of interface states. This is,

$$\tau \propto 1/N_I \qquad (4\text{-}4)$$

Figure 43 shows diffusion capacitance (C_D) as a function of forward current (I_F) for Cu_2S/CdS and $Cu_2S/Zn_xCd_{1-x}S$ junctions. Linear relations between diffusion capacitance and forward current are observed. The slope can be used to determine the electron lifetime from the following equation:

$$C_D = \frac{\tau}{AV_T} I_F \qquad (4\text{-}5)$$

where τ is the electron lifetime at the interface, A is the diode factor, and V_T is equal to kT/q (T is the temperature). The measured lifetime is 4×10^{-5} sec. for the CdS and 2×10^{-6} sec. for the $Zn_{0.25}Cd_{0.75}S$. Thus, the smaller electron lifetime at the interface for the

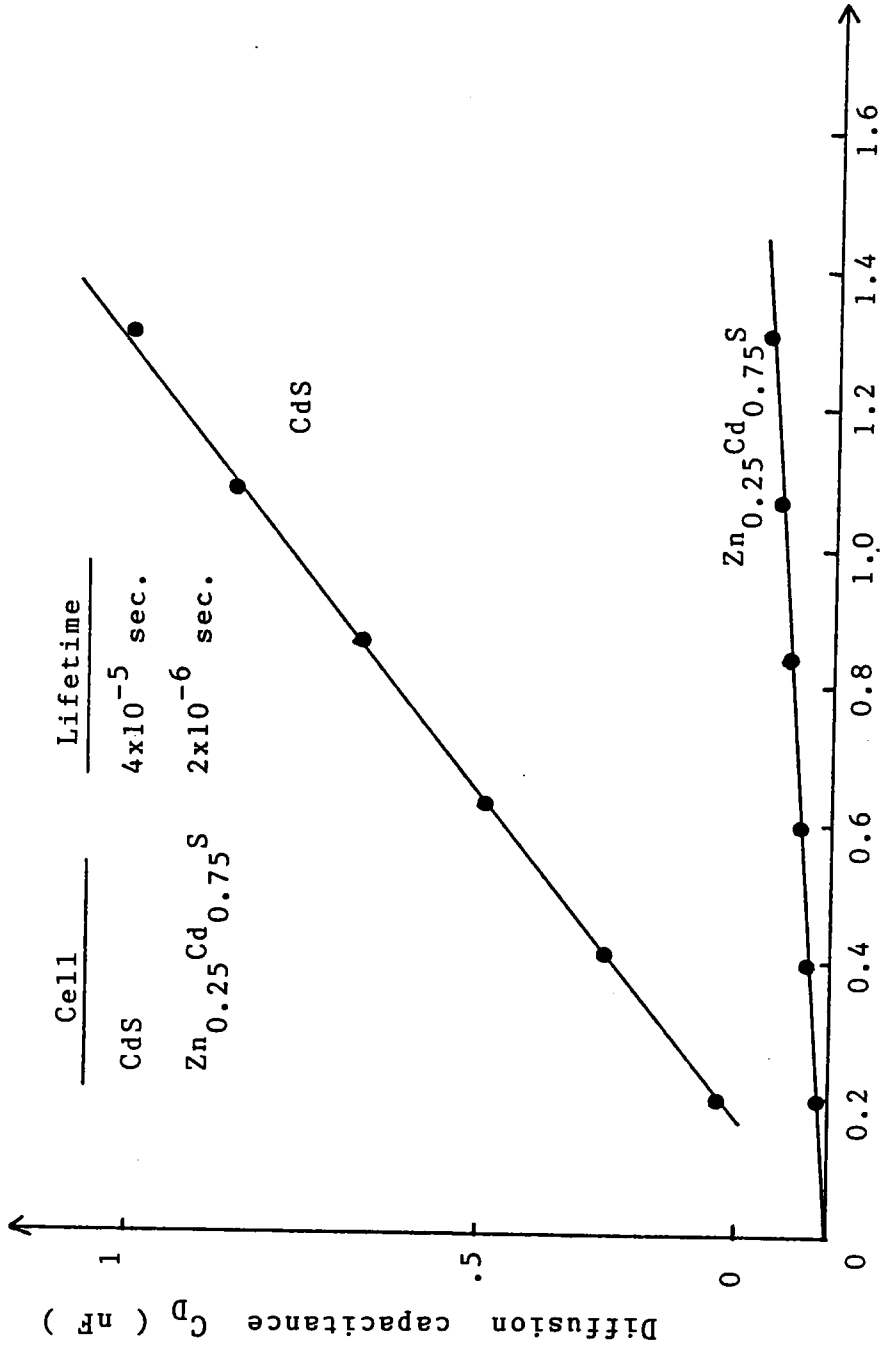

Figure 43: Diffusion capacitance as a function of forward current for Cu_2S/CdS and $Cu_2S/Zn_xCd_{1-x}S$ junctions.

$Cu_2S/Zn_{0.25}Cd_{0.75}S$ junction would indicate that its density of interface states (N_I) is larger. Accordingly, its interface recombination velocity (S_I) is larger (equation 2-16) and its short circuit current smaller (equation 2-8).

4.4 DEEP TRAP MEASUREMENTS

When Cu_2S/CdS and Cu_2S/ZnCdS cells are initially formed, they show poor junction behavior with large leakage currents. Post fabrication heat treatment helps to improve cell performance. During this heat treatment process, copper ions diffuse from Cu_2S into the CdS or ZnCdS layer and create a trap energy level there. Deep traps account for several unusual effects: the cross-over of dark and light I-V characteristics; the quenching and enchancement of the spectral response; frequency dependent capacitance; and the open circuit voltage decay. Thus, deep trap measurements are important. Trap energy level, trap density, and trap capture cross section can be determined from such measurements. Results and discussions of these measurements are divided into three parts: photocapacitance, space-charge-limited current, and thermally stimulated current.

A) Photocapacitance

The variation of photocapacitance with incident wavelength is shown in Figures 44-46 for Cu_2S/CdS, $Cu_2S/Zn_{0.11}Cd_{0.89}S$, and $Cu_2S/Zn_{0.25}Cd_{0.75}S$ cells. These curves are somewhat similar. Two peaks and two minima are observed in each figure. It can be seen that these peaks shift toward shorter wavelengths as the Zn content of the $Zn_xCd_{1-x}S$ increases (peaks, minima, and corresponding energies are listed in Table 7). The first peak occurs at 505 nm for Cu_2S/CdS cells. This wavelength corresponds to the bandgap of 2.45 eV for CdS. The peaks are observed at 485 nm and 460 nm for $Cu_2S/Zn_{0.11}Cd_{0.89}S$ and $Cu_2S/Zn_{0.25}Cd_{0.75}S$ cells respectively. These wavelengths correspond to the bandgaps of 2.56 eV and 2.70 eV. These peaks in photocapacitance are caused by direct band-to-band absorption, and corroborate the quantum efficiency measurements reported earlier, which show peaks due to this same cause. The second peak shifts from the wavelength of 650 nm to 560 nm and 540 nm as the content of Zn increases for $Cu_2S/Zn_xCd_{1-x}S$ cells. These wavelengths correspond to deep donor energies of 1.91 eV, 2.21 eV, and 2.30 eV below the conduction band of $Zn_xCd_{1-x}S$. It is seen that the deep

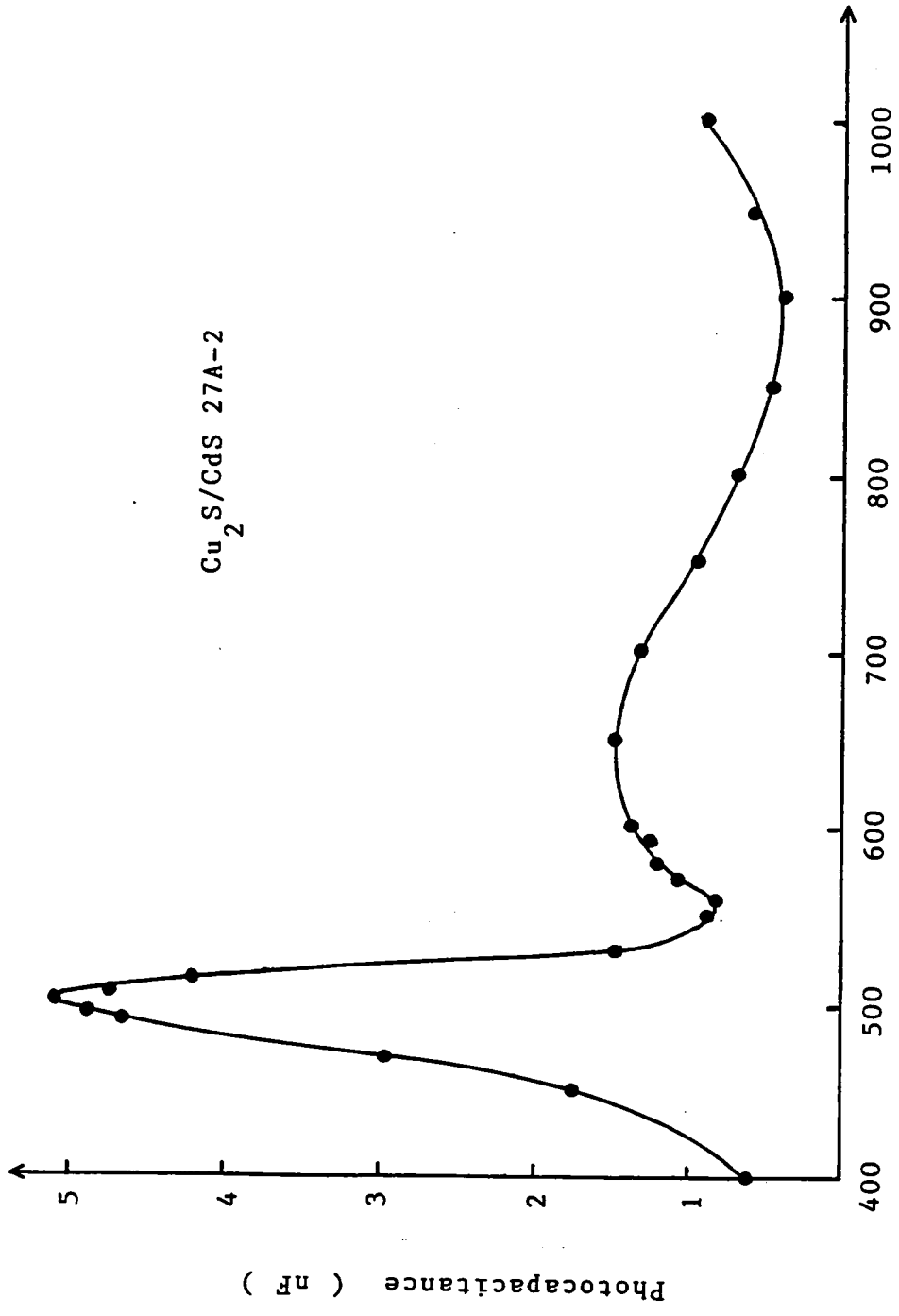

Figure 44: Variation of photocapacitance versus wavelength for Cu_2S/CdS cell.

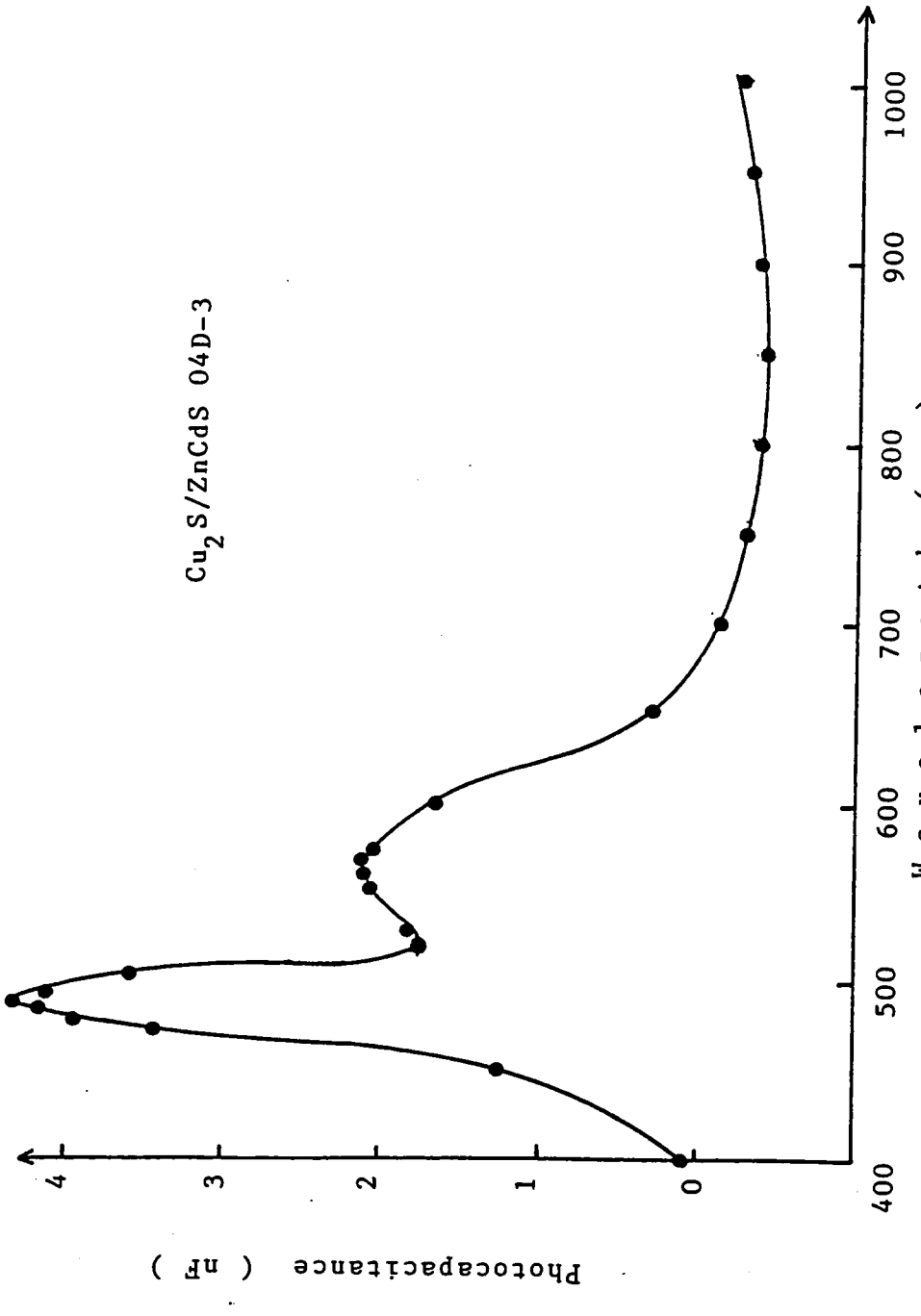

Figure 45: Variation of photocapacitance versus wavelength for $Cu_2S/Zn_{0.11}Cd_{0.89}S$ cell.

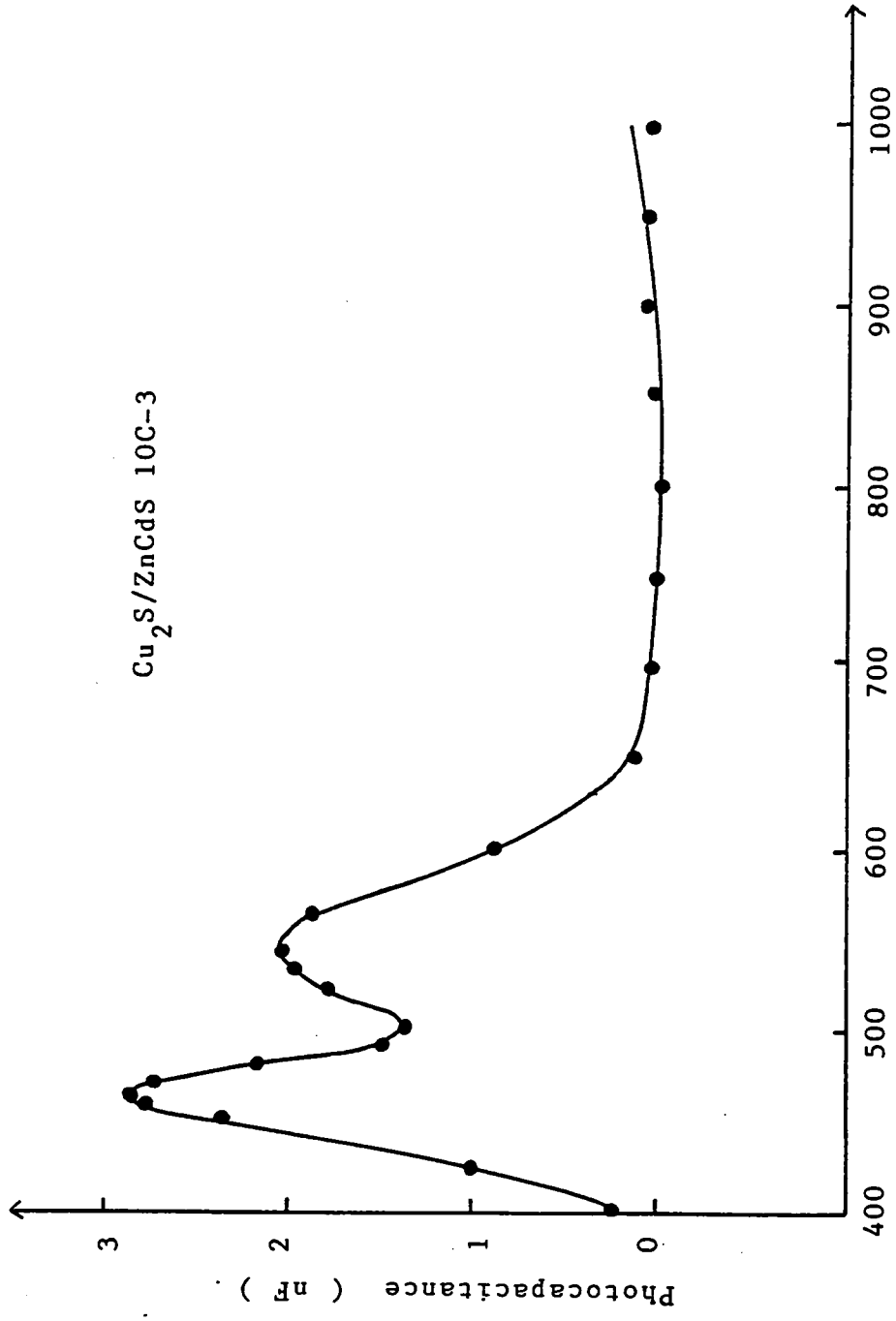

Figure 46: Variation of photocapacitance versus wavelength for $Cu_2S/Zn_{0.25}Cd_{0.75}S$ cell.

TABLE 7

Peaks, minima, and corresponding energies for Cu_2S/CdS, $Cu_2S/Zn_{0.11}Cd_{0.25}S$, and $Cu_2S/Zn_{0.25}Cd_{0.75}S$ cells.

Sample	Peaks (nm)	Energies (Band gap) (eV)	Peaks (nm)	Energies (Deep donor) (eV)
Cu_2S/CdS	505	2.45	650	1.91
$Cu_2S/Zn_{0.11}Cd_{0.89}S$	485	2.56	560	2.21
$Cu_2S/Zn_{0.25}Cd_{0.75}S$	460	2.70	540	2.30
	Minima (nm)	Energies (Deep acceptor) (eV)	Minima (nm)	Energies (Deep acceptor) (eV)
Cu_2S/CdS	560	2.21	900	1.38
$Cu_2S/Zn_{0.11}Cd_{0.89}S$	520	2.38	850	1.46
$Cu_2S/Zn_{0.25}Cd_{0.75}S$	500	2.48	800	1.55

donor energy becomes larger as the content of Zn increases, as expected, due to the larger bandgap.

The first minima are observed at wavelengths of 560 nm, 520 nm, and 500 nm in Figures 44-46. These minima indicate a quenching phenomena (discussed earlier) attributed to deep acceptor levels located at 2.21 eV, 2.38 eV, and 2.48 eV above the $Zn_xCd_{1-x}S$ valence band edge. The second minima in these figures are much broader, and are observed at wavelengths of roughly 900 nm, 850 nm, and 800 nm. These wavelengths correspond to deep acceptor levels of 1.38 eV, 1.46 eV and 1.55 eV above the valence band edge of $Zn_xCd_{1-x}S$. These results indicate that the deep acceptor energy becomes larger as the content of Zn of $Zn_xCd_{1-x}S$ increases for the same reason that the deep donor energies increase, as discussed above. Energy band diagrams for these cells, with the trap levels indicated, are shown in Figure 47.

B) Space-charge-limited current

Capacitance measurement results verify the existence of an i-layer near the junction. Space-charge-limited current measurements were performed in order to gain information about this layer. Log-log plots of I-V characteristics for Cu_2S/CdS and $Cu_2S/Zn_xCd_{1-x}S$ cells are shown in Figure 48. Four distinct regions are seen in the I-V curve for a

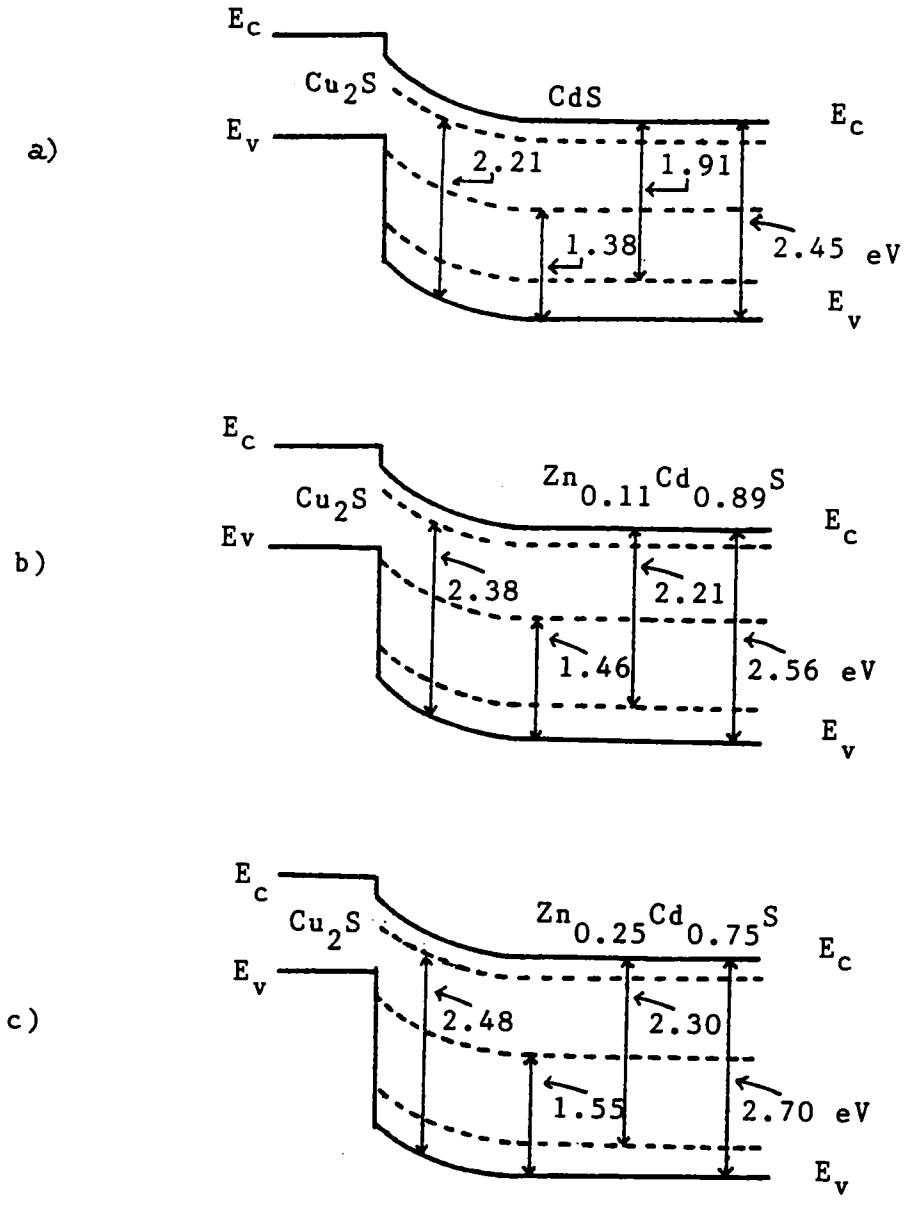

Figure 47: Energy band diagrams for a) Cu_2S/CdS, b) $Cu_2S/Zn_{0.11}Cd_{0.89}S$ and c) $Cu_2S/Zn_{0.25}Cd_{0.75}S$ cells, showing bandgaps and deep levels deduced from photocapacitance measurements. (Energy values are in eV)

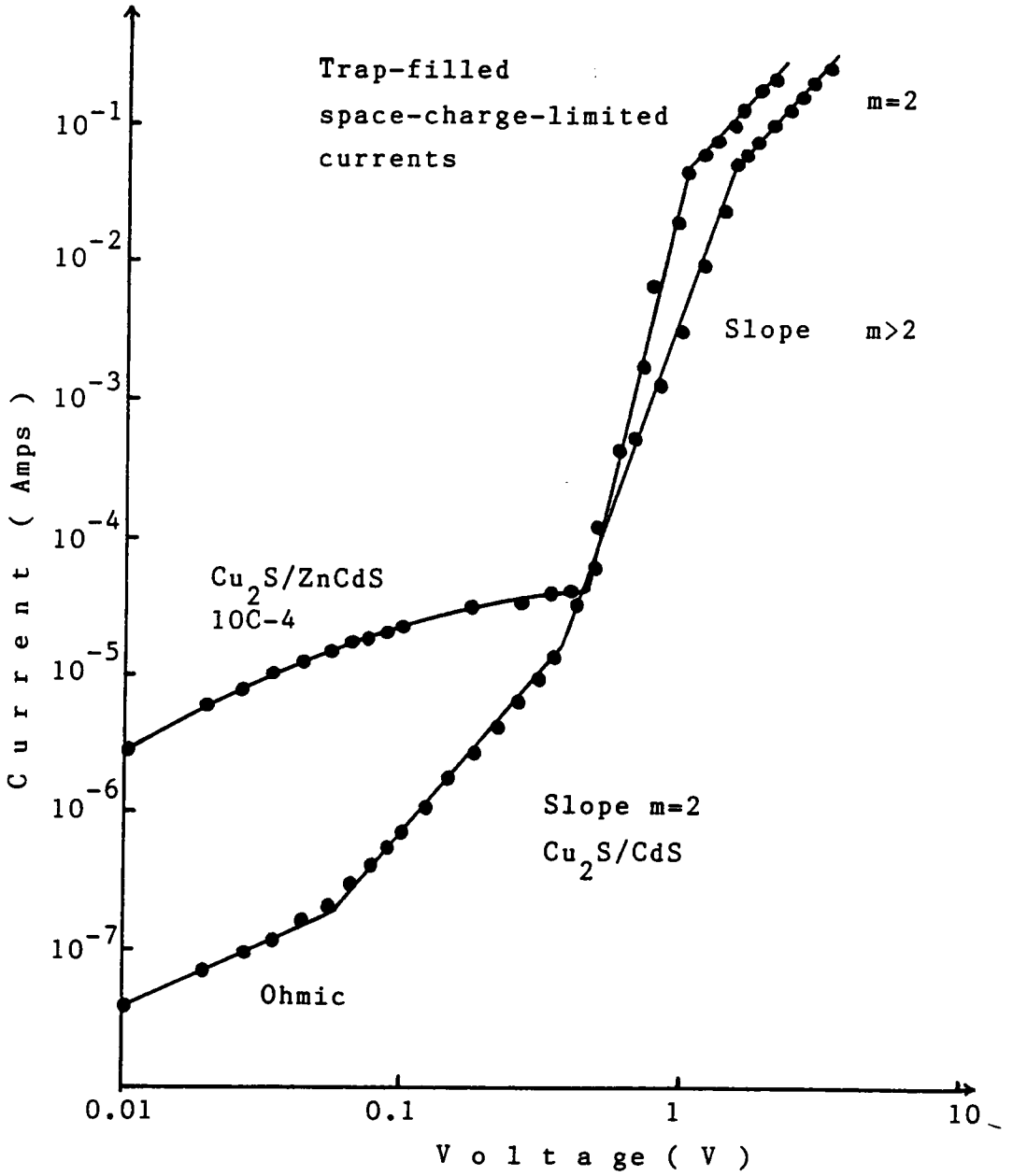

Figure 48: Log-log plot of I-V characteristics for Cu_2S/CdS and $Cu_2S/Zn_xCd_{1-x}S$ cells, showing space charge limited currents, and for the ZnCdS cell, a low voltage current saturation.

Cu_2S/CdS cell. At low voltages, the slope of the curve, m, is 1. This is an ohmic region. Following the ohmic region is a space-charge-limited current region with m = 2. Following this is a trap-filling region with m ≈ 13, followed by what appears to be a trap-filled space-charge-limited current region with m = 2. According to the theory developed by Lampert [66], such an I-V characteristic represents a material with a shallow trap. The trap-fill-limit voltage, V_{TFL}, is found to be 0.5 V, and the trap density is determined from equation (2-29). The value of N_t is approximately equal to 10^{16} cm^{-3}. The trap energy, E_t, can be estimated by using equations (2-27) and (2-28). E_t is thus determined to be 0.26 eV below the conduction band edge of CdS. This value is close to one of the traps (0.24 eV below the conduction band edge of CdS) obtained from photocapacitance measurements.

The I-V characteristic for $Cu_2S/Zn_xCd_{1-x}S$ cells differs somewhat from that of a Cu_2S/CdS cell. An ohmic region does appear at low voltages. Following this is an unexpected current-saturated region. The next two regions (a trap-filling region and a trap-filled space-charge-limited current region) are similar to those of Cu_2S/CdS cells. N_t is again estimated to be about 10^{16} cm^{-3}.

One model that may account for the presence of the current-saturated region is based on the filling of traps at the Cu_2S/ZnCdS interface. Figure 49(a) illustrates this. For small voltage, ionized negative charges exist in the p-type Cu_2S near the interface, and ionized positive charges occur in the depletion region of the compensated ZnCdS. The potential barrier height, ϕ, is caused by these charges. As V increases, the interface traps begin to fill. The negative charge in Cu_2S thus increases, as does the positive charge in the ZnCdS. ϕ also increases, (see Figure 49(a)) which opposes the applied voltage. Therefore, the current saturates. This can be demonstrated by the following equations:

$$J = J_{oo}\exp(-\phi/kT)\exp(qV/kT) \qquad (4\text{-}6)$$

$$= J_{oo}\exp((qV-\phi)/kT) \qquad (4\text{-}7)$$

When V = 0, ϕ can be designated as ϕ_o. As the voltage increases, $\Delta\phi$ caused by the filling of the interface traps appears. This increment of ϕ compensates the applied voltage. Therefore, $\phi = \phi_o - eV + \Delta\phi$ tends to be constant, and the current tends toward saturation. The current will increase again when the interface traps are all occupied. However, this is not so for the Cu_2S/CdS junction. The

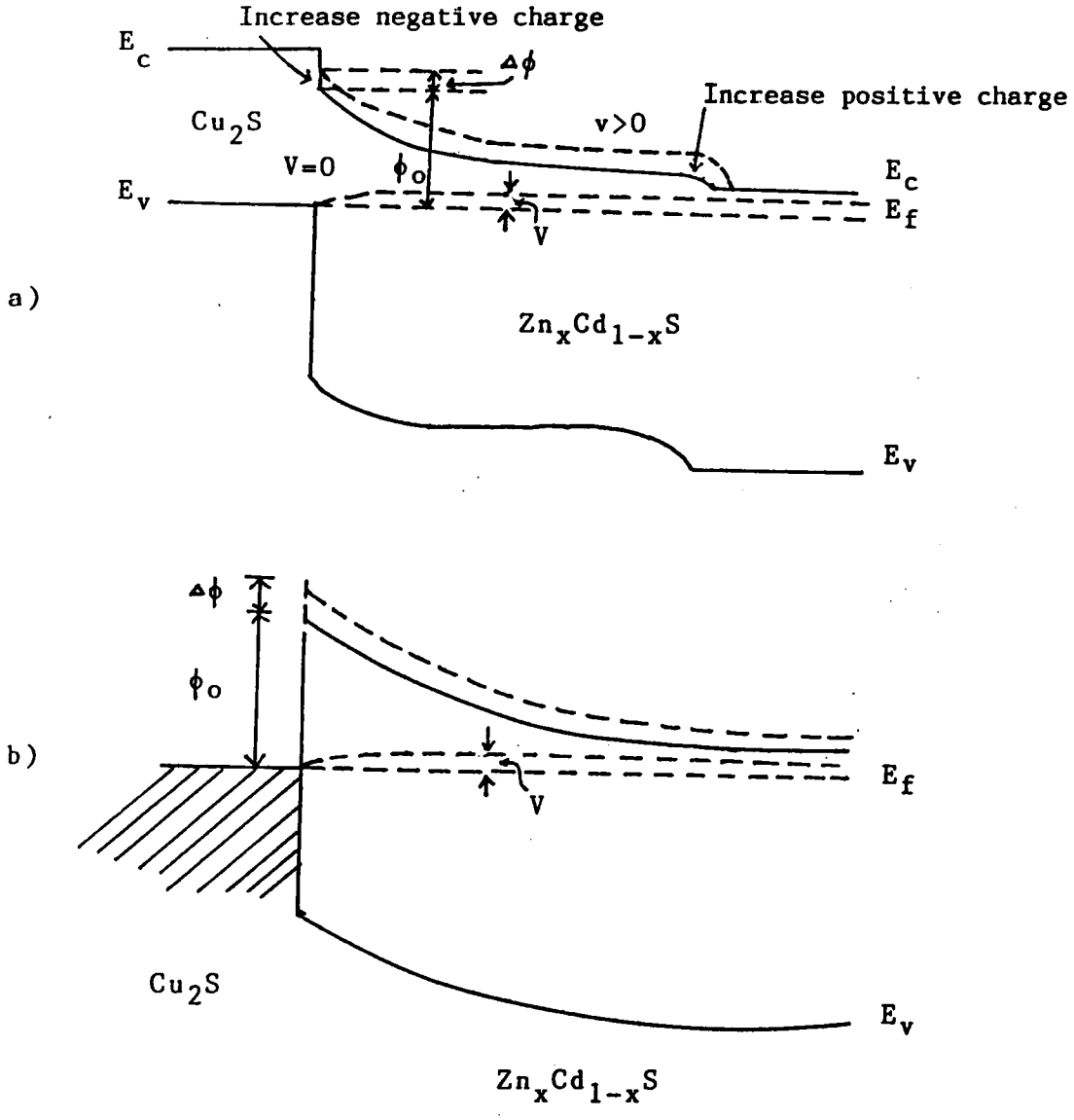

Figure 49: Energy band diagrams for $Cu_2S/Zn_xCd_{1-x}S$ junction, a) viewed as a p-n junction and b) viewed as a Schottky barrier, under forward bias.

interface traps are not as significant in current transport. Bulk traps become more important in this case. When V increases, electrons are trapped in the CdS space charge region, which reduces the net positive charge there. This results in the decrease of ϕ, and the increase of current.

Another model for explaining the existence of the current-saturated region is also associated with the filling of interface traps. The $Cu_2S/Zn_xCd_{1-x}S$ junction can be considered as a Schottky diode due to very high carrier concentration in the Cu_2S. The energy band diagram for a $Cu_2S/Zn_xCd_{1-x}S$ junction, viewed as a Schottky barrier, is shown in Figure 49(b). As stated earlier, ϕ tends to be constant under applied voltage, and the current tends toward saturation. The interface traps could result from the retention of Zn at the interface of the junction when Zn diffuses from ZnCdS to the Cu_2S [16]. Such is not the case for CdS. These traps could also result from gas atoms adsorbed during the cell fabrication process [81].

C) Thermally stimulated current (TSC)

Thermally stimulated current measurement is a powerful technique to study the deep traps in a material. The importance of these deep traps has been mentioned earlier. Figure 50 shows a thermally stimulated current curve for a Cu_2S/CdS junction (The experimental technique is described

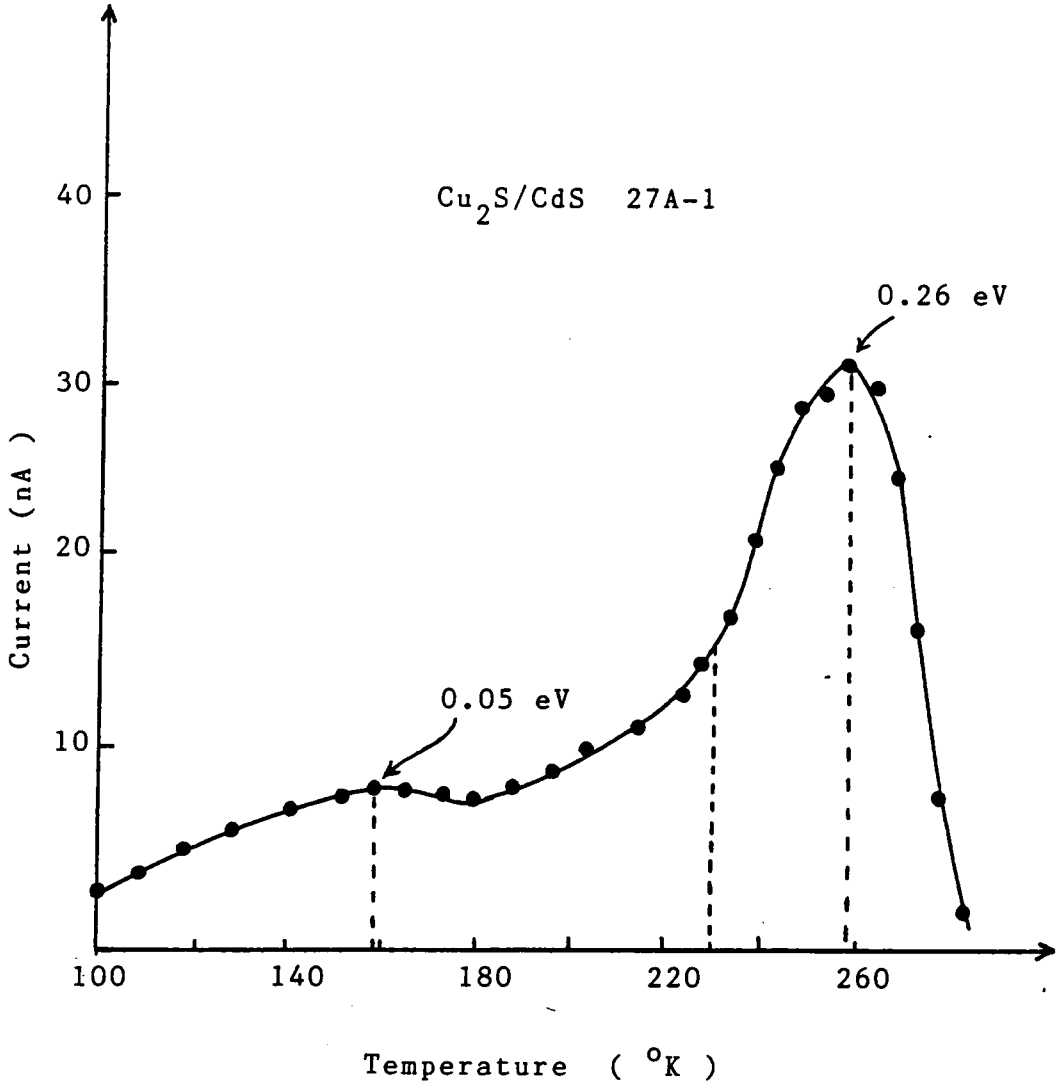

Figure 50: Thermally stimulated current curve for a Cu_2S/CdS junction. Energy level values are also indicated.

in Section 3.4.). The curve was measured at a heating rate of 0.2 degree/sec. Grossweiner's method was used to evaluate the deep trap energy level from the TSC curve [68]. Two peaks, one at 158°K and another at 258°K, are observed in this figure. The corresponding temperatures at which the current reaches one-half of the maximum current are 113°K and 228°K. The trap energy level below the conduction band, E_t, is determined by equation (2-35). These two energy levels are found to be 0.05 eV and 0.26 eV. The first energy level (0.05 eV) is a shallow donor energy level which is attributed to Cd excess in CdS. The second energy level (0.26 eV) is a shallow trap energy level. This is the result of Cu diffusion from Cu_2S to CdS during the cell fabrication process.

The same measurement was also applied to $Cu_2S/Zn_xCd_{1-x}S$ junctions. Unfortunately, no satisfactory results were obtained. The peak of the thermally stimulated current curve was not detected. The reasons for this are at present, unknown. It may form an area for future investigations.

Table 8 shows the trap energy levels obtained from above techniques. Trap energy level at 0.26 eV below the CdS conduction band edge obtained from space-charge-limited current and thermally stimulated current techniques is

consistent with the value (0.24 eV) obtained from photocapacitance technique, which gives us more confidence in the results obtained from photocapacitance technique for the $Cu_2S/ZnCdS$ cells.

Other techniques, such as frequency dependent capacitance, deep level transient spectroscopy (DLTS), capacitance transient, etc., can also potentially be used to study the deep traps of the $Cu_2S/Zn_xCd_{1-x}S$ junctions. These are also potential areas for future investigations.

TABLE 8

Trap energy levels obtained from photocapacitance, space-charge-limited current (SCLC), and thermally stimulated current (TSC) techniques. These values are with respect to conduction band of CdS or $Zn_xCd_{1-x}S$.

Technique	CdS	$Zn_{0.11}Cd_{0.89}S$	$Zn_{0.25}Cd_{0.75}S$
photocapacitance	0.24 eV	0.18 eV	0.22 eV
	1.07 eV	1.10 eV	1.15 eV
	1.91 eV	2.21 eV	2.30 eV
SCLC	0.26 eV	----	----
TSC	0.26 eV	----	----

Chapter V

CONCLUSIONS AND RECOMMENDATIONS

5.1 SUMMARY AND CONCLUSIONS

The objectives of this research were to compare the Cu_2S/CdS and $Cu_2S/ZnCdS$ solar cells using Cu_2S/CdS as a reference, and to understand more about the operation and properties of $Cu_2S/ZnCdS$ junctions in order to improve cell performance. These tasks were approached by means of electrical, spectral, capacitance, and deep trap measurements. The important results are summarized as follows:

1) I-V measurement yields the important electrical parameters; cell efficiency, fill factor, short circuit current, open circuit voltage, shunt resistance, and series resistance. From a $\ln(I_{sc})$ versus V_{oc} measurement, the diode factor, A, was determined to be about 1 for Cu_2S/CdS and $Cu_2S/Zn_{0.11}Cd_{0.89}S$ cells, and about 1.2 for $Cu_2S/Zn_{0.25}Cd_{0.75}S$ cells. A linear relation between $\ln(J_{oo})$ (current density) and ϕ (potential barrier height) was found for both types of cells. The increasing slope of $\ln(J_{oo})$ versus ϕ curves is attributed to the reduction in electron affinity mismatch.

2) V_{oc} and capacitance values are fairly constant with time for Cu_2S/CdS cell. However, V_{oc} decreases and capacitance increases with time for Cu_2S/ZnCdS cells. The V_{oc} decay and capacitance increase for the Cu_2S/ZnCdS case are attributed to longer decay of trapped charge (electron relaxation from the deep traps) near the junction.

3) White and blue bias light enhance the quantum efficiency of Cu_2S/CdS and Cu_2S/ZnCdS cells, whereas red bias light quenches the quantum efficiency of the cells. Ionization and filling of deep traps account for these enhancement and quenching effects. Stronger red quenching of the quantum efficiency for the Cu_2S/ZnCdS case is seen. This could be due to higher density of traps or larger capture cross section.

4) Capacitances are nearly independent of bias voltage, which indicates that an i-layer exists near the interface of the junctions. The electron lifetime of CdS (4×10^{-5} sec) is larger than that of ZnCdS (2×10^{-6} sec). This could be one of the reasons that the I_{sc} of Cu_2S/ZnCdS is smaller than that of Cu_2S/CdS made under similar conditions.

5) Photocapacitance as a function of wavelength was measured for both cell types. Two peaks and two minima occur for each cell. One deep donor trap and two deep acceptor traps were found for both types of cells. These trap energies become larger as the content of Zn increases.

6) Space-charge-limited current measurements give a trap density of about 10^{16} cm^{-3} for both types of cells. The deep energy level at 0.26 eV below the conduction band edge of CdS was found for Cu_2S/CdS cells, which is consistent with the photocapacitance result.

7) Thermally stimulated current measurements indicate two energy levels below the conduction band of CdS, at 0.05 eV and 0.26 eV. The first energy level can be attributed to the shallow donors in the CdS. The second energy level is attributed to the deeper traps, also consistent with the photocapacitance and SCLC measurements.

The smaller I_{sc} for the Cu_2S/ZnCdS cells is possibly a result of :

a) smaller electron lifetime at the interface. This indicates that its density of interface states (N_I) is larger (Section 4-3). Therefore, the interface recombination velocity is larger, and the I_{sc} smaller.

b) larger interface recombination velocity. This could be due to larger N_I or larger capture cross section (σ).

c) Enhanced Zn concentration near the junction. This could form a potential spike [16], increase trap density, and alter the properties of the Cu_2S, all of which tend to reduce the short circuit current.

The V_{oc} decay for the Cu_2S/ZnCdS cell was attributed above to several potential causes. This research indicates that a prominent mechanism could be due to the slower decay of trapped charge near the interface. The decay time constant for ZnCdS cells could be larger than that for CdS cells because the traps are deeper.

The above results demonstrate that the Cu_2S/ZnCdS cells differ from the Cu_2S/CdS cells in many ways. These differences include stronger red quenching, smaller electron lifetime at the interface, and deeper traps for the Cu_2S/ZnCdS cells. These differences can help to account for the reduced I_{sc} and the V_{oc} decay for the ZnCdS cells.

5.2 RECOMMENDATIONS FOR FUTURE WORK

1) The physical explanation for the linear relation between $\ln(J_{oo})$ and ϕ is not well understood. Further studies in this area are necessary to better understand the properties of the cells.

2) Other deep trap measurement techniques, such as frequency dependent capacitance, deep level transient spectroscopy (DLTS) and thermally stimulated capacitance, can be applied to study the deep traps of the junctions. These could give additional information related to trap concentrations and capture cross sections.

3) Measurements similar to those reported here on a set of CdS and ZnCdS based cells receiving different heat treatments could further clarify the role of the i-layer formed during heat treatment.

REFERENCES

1. D. C. Reynolds, G. Leies, L. L. Antes and R. E. Marburger, Phys. Rev., 96 (1954) 533.

2. D. A. Hammond and F. A. Shirland, Proc. Electron Components Conf., 1959, p.98.

3. F. A. Shirland, ARL Tech. Rep. 60-293, Harshaw Chem. Co., 1960.

4. A. E. Carlson, "Research on Semiconductor Films" WADC Tech Rep. 56-62, Clevite Corp., 1956.

5. A. E. Carlson, L. R. Shiozawa, and J. D. Finegan, U. S. Patent 2,820,841 (1958).

6. R. Williams and R. H. Bube, J. Appl. Phys., 31 (1960) 968.

7. H. G. Grimmeiss and R. Memming, J. Appl. Phys., 33 (1962) 217.

8. D. A. Cusano, Solid State Electronics, 6 (1963) 217.

9. P. N. Keating, J. Appl. Phys., 36 (1965) 564.

10. E. R. Hill and B. G. Keramidas, IEEE Trans. Electron Devices, 14 (1967) 22.

11. B. Selle, W. Ludwig and R. March, Phys. Stat. Sol., 24 (1967) K149.

12. R. B. Hall R. W. Birkmire, J. E. Phillips and J. D. Meakin, Appl. Phys. Lett., 38 (1981) 925.

13. P. K. Bhat, S. R. Das, D. K. Pandya and K. L. Chopra, Solar Energy Material, 1 (1979) 215.

14. G. H. Hewig and W. H. Bloss, Thin Solid Films, (1977) 1.

15. A. M. Barnett, J. A. Bragagnolo, R. B. Hall, J. E. Phillips and J. D. Meakin, Proc. 13th IEEE Photovoltaic Specialists' Conference, IEEE, New York, 1978, p.419.

16. L. C. Burton, Solar Cells, 1 (1979/1980) 159.

17. R. B. Hall and J. D. Meakin, Thin Solid Films, 63 (1979) 203.

18. S Martinuzzi, J. Qualid, D. Sarti and J. Gervais, Thin Solid Films, 51 (1978) 211.

19. E. W. Williams, K. Jones, A. J. Griffiths, D. J. Roughley, J. M. Bell, J. H. Steven, M. J. Huson, M. Rhodes and T. Costish, Proc. 2nd EC Photovoltaic Solar Energy Conference, Berlin, (April 1979) p.874.

20. R. R. Chamberlin and J. S. Skarman, J. Electrochem. Soc., 113 (1966) 86.

21. R. R. Chamberlin and J. S. Skarman, Solid State Electron., 9 (1966) 819.

22. R. S. Feigelson, A. N. Diaye, S.-Y. Yin and R. H. Bube, J. Appl. Phys., 48 (1977) 3162.

23. W. Shockley, U. S. Patent 2,569,347 (1951).

24. A Rothwarf, Proc. Int. Workshop on Cadmium Sulfide Solar Cells and Other Abrupt Heterojunction, University of Delaware, May 1975, in Publ. NSF-RANN-AER75-15858, 1975, pp.9-51, National Science Foundation.

25. A Rothwarf, Solar Cells, 2 (1980) 141.

26 N. Nakayama, Japan. J. Appl. Phys., 10 (1971) 1415.

27. W. Palz, J Besson, T Nguyen Duy and J. Vedel, Conf. Rec., 9th IEEE Photovoltaic Specialists' Conf., 1972, p.91.

28. T. S. teVelde and J. Dieleman, Philips Res. Repts., 28 (1973) 573.

29. W. Palz, J Besson, T Nguyen Duy and J. Vedel, Conf. Rec., 9th IEEE Photovoltaic Specialists' Conference, p.69, Nov. 1973.

30. B. Baron, A. W. Catalano and E. A. Fagen, Proc. 13th Photovoltaic Specialists' Conf., Washington D. C., June 5-8, 1978, IEEE, New York, 1978, p.406.

31. L. R. Shiozawa, F. Augustine, G. A. Sullivan, J. M. Smith III and W. R. Cook Jr., Final Rep., June 1966-

May 1969, Clevite Corp. (Contract AF-33(615)-5224).

32. A. Rothwarf, Proc. Int. Conf. on Solar Electricity, Toulouse, March 1976, Centre National d'Etudes Spatiales, Toulouse, 1976, p.273.

33. L. L. Kazmerski, Polycrystalline and Amorphous Thin Films and Device, Academic Press, New York, 1980 Chap. 8.

34. A Rothwarf, Tech. Rep. NSF-RANN-AER-72-03478 A03-TR75-03, May 1975, National Science Foundation.

35. L. C. Burton and T. L. Hench, Appl. Phys. Lett., 29 (1976) 612.

36. T. M. Peterson, Ph. D. Thesis, Lawrence Berkeley Laboratory, University of California at Berkeley, 1975.

37. Final Rep., NSF/RANN/AER 72-03478 A04 FR76, Institute of Energy Conversion, University of Delaware. 1977.

38. J. Bougnot, Int. Workshop on CdS Solar Cells, University of Delaware, 1975, Newark, Delaware, 1975, p.337.

39. H. W. Brandhorst, Jr., Proc. 7th Photovoltaic Specialists' Conf., Pasadena, California, November 1968, IEEE, New York, 1968, p.33.

40. J. Lindmayer and A. G. Revesz, Solid State Electronics, 14 (1971) 647.

41. P. F. Lindquist and R. H. Bube, J. Appl. Phys., 43 (1972) 2839.

42. R. B. Hall and V. P. Singh, J. Appl. Phys., 50 (1979) 6406.

43. B. M. Basol and O. M. Stafsudd, Thin Solid Films, 78 (1981) 217.

44. E. Schibli and A. G. Miles, Solid State Electronics, 11 (1968) 323.

45. D. L. Losee, J. Appl. Phys., 46 (1975) 2204.

46. A Kobayashi, J. Appl. Phys., 49 (1978) 934.

47. A Kobayashi, Appl. Phys., 18 (1979) 345.

48. L. Hmurcik, L. Ketelson and R. A. Serway, J. Appl. Phys., 53 (1981) 3839.

49. G. I. Roberts and C. R. Crowell, Solid State Electronics, 16 (1972) 29.

50. G. I. Roberts and C. R. Crowell, J. Appl. Phys., 41 (1969) 1767.

51. J. Qualid, D. Sarti, J. Gervais and S. Martinuzzi, J. Appl. Phys. 12 (1979) 2313.

52. W. G. Haines and R. H. Bube, 14th IEEE Photovoltaic Specialists' Conf., 1980, p. 718.

53. I. E. Ture, F. Poulin, A. W. Brinkman and J. Woods, Phys. Stat. Sol. (a) 77 (1983) 535.

54. R. H. Bube, J. Appl. Phys., 33 (1962) 1733.

55. G. A. Marlor and J. Woods, Proc. Phys. Soc., 81 (1963) 1013.

56. G. A. Marlor and J. Woods, Brit. J. Appl. Phys., 16 (1965) 1449.

57. U. Buget and G. T. Wright, Brit. J. Appl. Phys., 16 (1965) 1457.

58. S. J. McGarthy and S. S. Yee, Solid State Electronics, 17 (1974) 485.

59. L. D. Partain, G. A. Armantrout and J. Leong and P. Warter, J. Electronic Materials, 9 (1980) 467.

60. K. H. Nicholas and J. Woods, Brit. J. Appl. Phys., 15 (1964) 783.

61. S. G. Patil, J. Appl. Phys., 5 (1972) 1692.

62. J. G. Simmons and G. W. Taylor, Phys. Rev. B, 5 (1972) 1619.

63. D. V. Lang, J. Appl. Phys., 45 (1974) 3023.

64. C. Grill, G. Bastide, G. Sagnes and M. Rouzeyre, J. Appl. Phys., 50 (1979) 1375.

65. P. Besomi and B. Wessel, J. Appl. Phys., 51 (1980) 4305.

66. M. A. Lampert, Phys. Rev., 103 (1956) 1648.

67. J. T. Randall and M. H. F. Wilkins, Proc. Roy. Soc. A, 184 (1945) 390.

68. L. I. Grossweiner, J. Appl. Phys., 24 (1953) 1306.

69. A. E. Potter, Jr., R.L. Schalla, H. W. Brandhorst, Jr., and L. Rosenblum, IEEE 7th Photovoltaic specialists conference, (1968) p.62.

70. W.Devaney, S. Lorenz, and J. D. Meakin, Proc. Terrestrial Photovoltaic Measurement-II, ERDA/NASA-1022/76/10 p.385.

71. L. C. Burton et al., Proc. 12th IEEE photovoltaic specialists conference, Baton Rouge, LA (1976)

72. S. Oktik, G. J. Russell, and J. Woods, Solar Cell, 5 1982) 231.

73. J. D. Meakin et al., Semi-Annu. Progr. Rept. NSF/RANN/ AER72-03478 A04PR75/4 (1975) 69.

74. K. W. Boer, Phys. Stat. Sol. (a) 49 (1978) 13.

75. Progress Report XR-9-8063-1, Institute of Energy Conversion, University of Delaware, June 1979, p.17.

76. K.H. Norian and R. B. Hall, Thin Solid Films, 88 (1982) 55.

77. W. D. Gill and R. H. Bube, J. Appl. Phys., 41 (1970) 3731.

78. A. L. Fahrenbruch and R. H. Bube, J. Appl. Phys., 45 (1974) 1264.

79. A. Rothwarf, J. Phillips, and N. C. Wyeth, Proc. 13th IEEE Photovoltaic Specialists Conference, Washington, D. C. (1978) p.399.

80. L. C. Burton, Private Communication, Photovolt. Lab., Virginia Tech (1985).

81. S Martinuzzi, Solar Cell, 5 (1982) 243.

The vita has been removed from the scanned document